PROCESSING AND CHARACTERIZATION OF ζ-Ta_4C_{3-x}: A HIGH TOUGHNESS TANTALUM CARBIDE

by

Michael M. Sygnatowicz

A dissertation submitted to the faculty of
The University of Utah
in partial fulfillment of the requirements for the degree of

Doctor of Philosophy

Department of Materials Science and Engineering

The University of Utah

December 2014

The University of Utah Graduate School

STATEMENT OF DISSERTATION APPROVAL

The dissertation of **Michael M. Sygnatowicz**

has been approved by the following supervisory committee members:

Dinesh K. Shetty	, Chair	**10-31-2014** Date Approved
Feng Liu	, Member	**10-28-2014** Date Approved
Richard Cohen	, Member	**10-28-2014** Date Approved
Ravi Chandran	, Member	**10-28-2014** Date Approved
Taylor Sparks	, Member	**10-28-2014** Date Approved

and by **Feng Liu**, Chair/Dean of

the Department/College/School of **Materials Science and Engineering**

and by David B. Kieda, Dean of The Graduate School.

ABSTRACT

Tantalum carbides are commonly processed by hot-pressing, canned hot-isostatic-pressing, or spark-plasma sintering because of their high melting temperatures and low diffusivities. This study reports processing of dense ζ-Ta_4C_{3-x} by reaction sintering of a Ta and TaC powder mixture (C/Ta atomic ratio = 0.66). ζ-Ta_4C_{3-x} is of interest due to its rhombohedral (trigonal) crystal structure that may be characterized as a polytype with both face-centered-cubic (fcc) and hexagonal-close-packed (hcp) Ta stacking sequences interrupted by stacking faults and missing carbon layers. This structure leads to easy cleaving on the basal planes and high fracture toughness.

A key step in processing is the hydrogenation of the Ta powder to produce β-TaH_x, a hard and brittle phase that enables efficient comminution during milling and production of small, equiaxed Ta particles that can be packed to high green density with the TaC powder. Studies of phase evolution by quantitative X-ray diffraction during sintering revealed several intermediate reactions: (a) decomposition of β-TaH_x to Ta, (b) diffusion of C from γ-TaC to Ta leading to the formation of α-Ta_2C_y, with the kinetics described by the Johnson-Mehl-Avrami-Kolmogorov (JMAK) equation with an exponent, $n = 0.5$, and an activation energy of 221 kJ/mole, (c) equilibration of α-Ta_2C_y and γ-$TaC_{0.78}$ phases, and (d) formation of ζ-$Ta_4C_{2.56}$ from the equilibrated α-Ta_2C and γ-$TaC_{0.78}$ phases with the kinetics characterized by a higher JMAK exponent ($n \approx 3$) and higher activation energy (1089 kJ/mole). The microstructure showed evidence of

nucleation and growth of the ζ-$Ta_4C_{2.56}$ phase in both the α-Ta_2C and γ-$TaC_{0.78}$ parent phases with distinct difference in the morphology due to the different number of variants of the habit plane.

A hot-pressed and hot-isostatic-pressed (HIPed) material (C/Ta atomic ratio = 0.66), having formed 95 w% ζ-phase, attained a fracture toughness of 15.6 ± 0.5 MPa√m and a fracture strength of 508 ± 97 MPa, while a pressureless sintered and HIPed counterpart, having formed 89 w% ζ-phase and 11 w% γ-$TaC_{0.78}$, attained a fracture toughness of 13.7 ± 0.3 MPa√m and a fracture strength of 679 ± 56 MPa. All ζ-phase containing materials showed rising R-curves. The high fracture toughness and rising R-curve were attributed to ligament bridging across the crack face. The ligaments, called lamella, were formed as a result of weak cleavage planes in the basal plane of the ζ-Ta_4C_{3-x} crystal.

TABLE OF CONTENTS

LIST OF NOMENCLATURE

K_{Ic}:	fracture toughness.
K_R:	crack growth resistance.
K_a:	crack-driving force.
H_V:	Vickers hardness
σ_f:	fracture strength.
y:	C/Ta atomic ratio in γ-TaC_y
y':	0.5 x C/Ta atomic ratio in α-$Ta_2C_{y'}$
a:	crack length.
a_o:	initial crack size.
Å:	angstrom.
eV:	electron volts.
k:	temperature dependent rate constant for α-$Ta_2C_{y'}$ formation.
α_∞:	maximum weight fraction of α-$Ta_2C_{y'}$ formed.
Q_1:	activation energy for the formation of α-$Ta_2C_{y'}$.
κ:	temperature dependent rate constant for ζ-Ta_4C_{3-x} formation.
ζ_∞:	maximum weight fraction of ζ-Ta_4C_{3-x} formed
Q_2:	activation energy for the formation of ζ-Ta_4C_{3-x}.

ACKNOWLEDGMENTS

I would like to express my appreciation to Prof. Dinesh K. Shetty for the time and effort he has given me over the last five years. Also, to Prof. Raymond C. Cutler whose undergraduate class convinced me to stay in the field. Also, to Roger Marc Flinders, who I've always been able to rely on for advice and clarification. I would also like to give a very special thanks to Marilyn Bishop who made the last two years of my graduate carrier a pleasant experience.

Lastly, I would like to thank my wife, Amy, and my parents, Ania and George, for their constant support and encouragement. Dziękuję

CHAPTER 1

REVIEW OF THE LITERATURE

1.1 Introduction

Tantalum carbides are part of a small group of ceramics known as ultra-high temperature ceramics (UHTC). They exhibit high melting temperatures [1, 2], high hardness and fracture toughness [3-5], low thermal expansion [6], both low and high thermal conductivity [2, 7], high resistance to oxidation [6, 8, 9] at temperatures above 2000°C, semimetal electrical resistivity [7], and low chemical reactivity [7]. UHTCs are extensively used in the aerospace industry where rapid change in temperature, especially in the presence of burning fuel [10], or as a result of friction from the atmosphere [11] limit or make impossible the use of any other types of materials. There are over 300 materials with melting temperatures above 2000°C, but only about 15 have melting temperatures above 3000°C and include materials such as carbon, tungsten, titanium carbide, and rhenium [2].

The Ta-C binary system includes three carbides of interest: the face-centered-cubic (fcc) γ-TaC_y, the hexagonal-close-packed (hcp) α- or β-$Ta_2C_{y'}$, and the rhombohedral (trigonal) ζ-Ta_4C_{3-x}. Figure 1.1 shows the Ta-C phase diagram reported by Gusev *et al.* [1]. It is evident from the phase diagram that these carbides exhibit wide ranges of nonstoichiometries relative to their nominal structural chemical formulae.

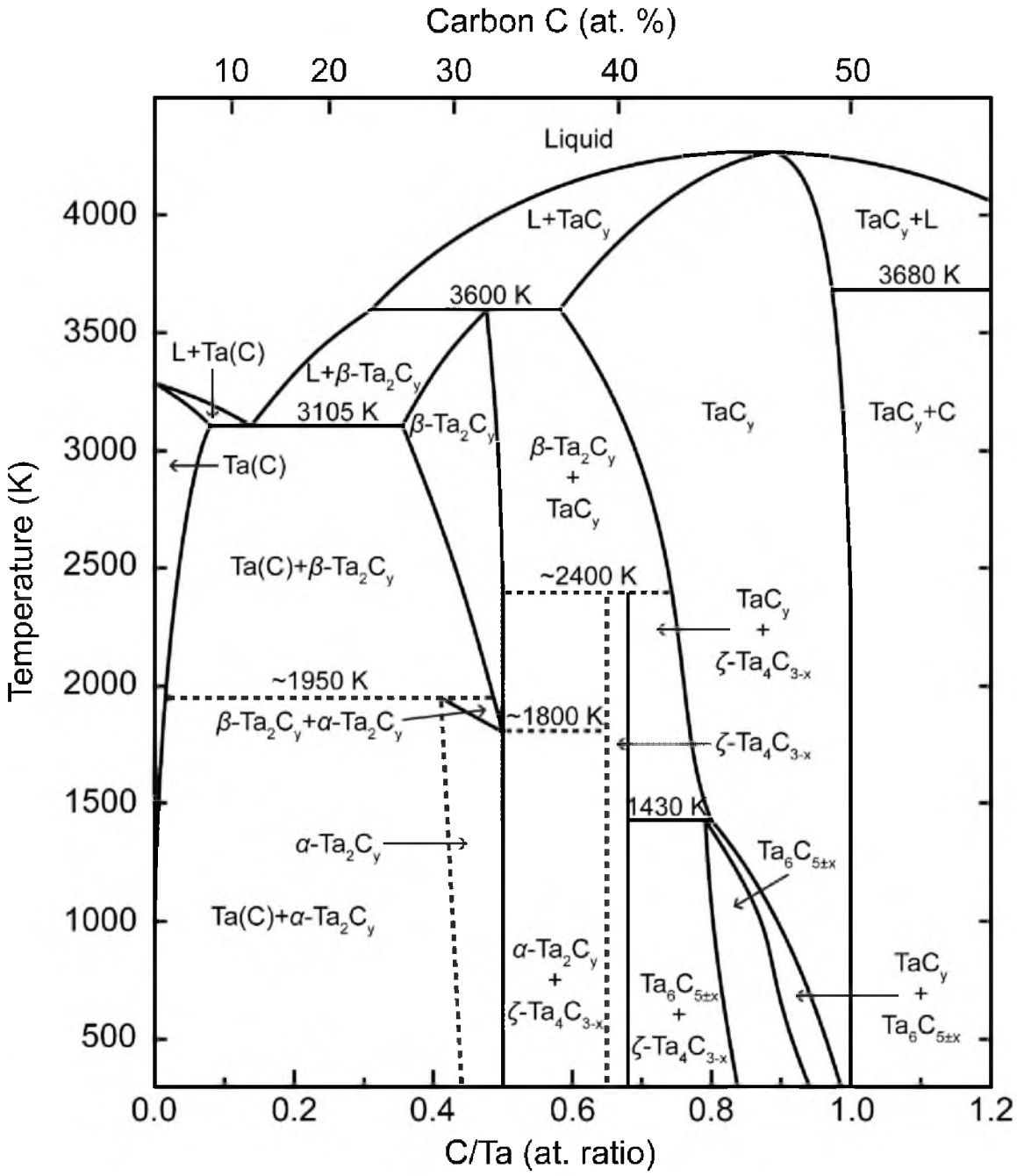

Figure 1.1 Phase diagram of the Ta-C system as reported by Gusev *et al.* [1].

The three carbides also offer some unique properties. The γ-TaC_y phase has an extremely high melting point ($T_m \approx 4000^oC$ for $TaC_{0.9}$), second only to HfC. The α/β-Ta_2C_y phase exhibits high oxidation resistance [9] and ablation resistance [10], and substantial plasticity at elevated temperatures [12]. It has been shown recently that tantalum carbides containing high weight fractions of the ζ-Ta_4C_{3-x} phase exhibit high fracture toughness ($K_c \approx 12.7$ MPa√m for 83 w% ζ-Ta_4C_{3-x} [3] and $K_c \approx 13.8$ MPa√m for 12 w% ζ-Ta_4C_{3-x} [5]).

Due to their high melting temperatures, Ta, and Ta carbides are difficult to sinter, and are often consolidated by hot-pressing [3, 13], canned hot-isostatic pressing (HIP) [14, 15], or spark plasma sintering (SPS) [5, 16]. Zhang *et al.* [13] hot-pressed γ-TaC powder compacts at 30 MPa. Without the addition of any sintering aids they obtained a density of 75% of theoretical by hot-pressing at 1900°C and the density increased to 96% of theoretical at 2400°C. With the addition of 0.36 w% B_4C or 0.43 w% B_4C and 0.13 w% C they were able to hot-press γ-TaC to a theoretical density of 96% at 2100°C. Hackett *et al.* [3] hot-pressed mixtures of γ-TaC and Ta with C/Ta atomic ratios of 1.0, 0.9, 0.8, 0.7 and 0.6 at 1800°C for 120 min without the use of sintering aids. The relative amounts of the phases obtained at the different C/Ta ratios were consistent with the phase diagram of Figure 1.1, with densities exceeding 96% of theoretical desnity. The composition corresponding to C/Ta = 0.6 produced a two-phase mixture of 83 w% of ζ-Ta_4C_{3-x} and 17 w% of α-Ta_2C and exhibited a high fracture toughness of 12.7 MPa√m in single-edge-precracked-beam (SEPB) tests. Liu *et al.* [5, 16] spark-plasma sintered γ-TaC and Ta powder mixtures corresponding to C/Ta ratios of 0.7 and 0.5 at temperatures ranging from 1600 to 1900°C. The 0.7 composition produced two-phase composites of

substoichiometric γ-TaC_y and ζ-Ta_4C_{3-x} with the amount of the latter phase increasing with temperature to 21 w% at 1900°C. These two-phase composites also exhibited high fracture toughness, with a reported value of 13.8 MPa√m for the material spark-plasma sintered at 1700°C [5]. The study proposed a two-stage phase conversion in which Ta and γ-TaC react to form substoichiometric γ-$TaC_{0.86}$ and α-$Ta_2C_{y'}$ at 1600°C and then further react to form γ-TaC_y and ζ-Ta_4C_{3-x} above 1700°C. Spark-plasma sintering of the 0.5 C/Ta ratio powder mixture at 1500°C produced dense (~96%), single-phase α-Ta_2C carbide, but its mechanical properties were inferior to those of the composites containing the ζ-Ta_4C_{3-x} phase [16].

The mechanism of toughening in the ζ-Ta_4C_{3-x} phase is not well understood. Difficulties in processing single-phase compacts of ζ-Ta_4C_{3-x} and lack of kinetic data on densification and phase formation are the major reasons for this lack of understanding. The ζ-Ta_4C_{3-x} phase is known to have a nano-lamellar subgrain structure with easy-cleaving basal planes similar to Ti_3XC_2 (X = Si, Al) [17-22]. This common feature between these two classes of materials plays a central role in their high fracture toughness. Recent studies by Morris *et al.* [23-25] have shown that the ζ-Ta_4C_{3-x} phase nucleates on the close packed planes in both the α-$Ta_2C_{y'}$ and the γ-TaC_y grains. When the ζ-Ta_4C_{3-x} phase nucleates within the γ-TaC_y grains it acquires a complex crisscrossing platelet morphology as a result of the multiple close-packed {111} planes in the fcc structure. Conversely, when the ζ-Ta_4C_{3-x} phase nucleates within α-$Ta_2C_{y'}$ grains it acquires a uniform parallel lamellar morphology, due to the single family of {0001} close-packed planes available in the hcp structure. Though ζ-Ta_4C_{3-x} has been shown to be stable at low temperatures, even after annealing, and/or pulverization [1], the kinetics

of its formation and the rate controlling mechanism(s) of its formation are not known.

There is a need to develop pressureless sintering of Ta-based materials to process near-net-shape components of high density, controlled phase content and microstructure. Particle sizes of the starting materials, for example, Ta metal and/or TaC, control the kinetics of formation and densification of the desired phase. Fine grained Ta metal powder is difficult to produce by conventional milling due to its ductility. Embrittlement of metals by hydrogenation has been successfully employed in the production of fine titanium, zirconium, and magnesium powders [26-28], and has been a processing step in the capacitor industry to make Ta powder [29-35]. Keeping Ta powder hydrogenated until alloying or secondary milling with powders such as γ-TaC_y, and dehydrogenating as part of the densification process could greatly improve sinterability by limiting the formation of agglomerates and removing surface oxides from Ta and γ-TaC_y powders. There is limited understanding of how milling of hydrogenated powders compare to non-hydrogenated powders relative to particle size, shape, agglomerate characteristics, and sintering characteristics.

1.2 Body-Centered-Cubic Ta Phase and Orthorhombic TaH_x Phase

Tantalum metal exists in two forms, α-Ta which has a *bcc* crystal structure with space group *Im3m* and a lattice constant of 3.3058 Å, and metastable β-Ta which has a tetragonal crystal structure with a space group *P42/mmm* and lattice constants of a = 10.194 Å and c = 5.313 Å. Carbon has limited solubility in the *bcc* Ta lattice at low temperatures (<1500°C) but can reach as high as 7.5 atomic % at a temperature of 2843°C, which corresponds to the liquid → Ta(C) + β-Ta_2C_y eutectic point [36].

Fine grained Ta metal powder is difficult to produce by conventional milling due to its ductility. The embrittlement of Ta by the dissolution of atomic hydrogen at a low temperature (~300-350^{o}C), phase transformation to a brittle metal hydride phase on cooling, comminution by milling and dehydrogenation is a common process for reducing particle size without significant oxygen contamination. Of the two primary Ta powder processing methods, mechanical processing can produce high purity powder but generally have low surface areas, while chemical processes, involving active reducing metals such as sodium, produce high surface area powders but they can suffer from broad bimodal distributions and the risk of contamination [37, 38]. Mechanical processing of capacitor grade Ta powder often involves hydrofluoric acid surface cleaning, wash removal of acid, hydrogenation, comminution, acid removal of contaminants, and dehydrogenation processing steps. The resulting powder forms a flake-like particle morphology, which is desired since such powders produce compacts with high green strength [31], and a requisite amount of porosity for desired electrical properties [32]. Though the flakes can attain an adequate specific surface area (0.5 m^2/g) [31], the flake morphology is not desired where high density Ta-based carbides with good mechanical properties are needed. Attempts at producing uniform nonagglomerated powder required multistep processing and the specific surface area of the powder was limited to about 1.2 m^2/g [34]. High surface area powders (S_w = 4 to 20 m^2/g) have been produced in some cases, but at the expense of significant oxygen contamination ($\geq$ 60000 ppm) [35, 39] which can form undesired low melting temperature Ta-O phases and inhibit densification [13].

The dissolution of atomic hydrogen in the bcc structure of Ta (α-Ta) results, upon

cooling to room temperature (T ~ 25°C), in the precipitation of the ordered orthorhombic (superlattice) phase, β-TaH_x (0.468 < x < 0.632), ordered monoclinic phase, δ-TaH_x (x > 0.667) or a mixture of the two phases [40-44]. Precipitation typically occurs within Ta grains where the hydrogen atoms occupy the tetragonal interstitial sites [45, 46]. As seen in the binary Ta-H phase diagram of Figure 1.2 [41, 44, 47], significant concentration of H can be dissolved in the Ta lattice at temperatures above ~61°C. As the β-TaH_x (or δ-TaH_x) precipitates grow, isotropic and anisotropic strains develop between the α-Ta and the precipitate phases, thus embrittling the grains and forming microcracks [45, 46]. Though not required, the use of a palladium catalyst can greatly increase the rate of hydrogenation [48]. Elevated temperatures are not, however, required as recently reported by Dunlap *et al.* [49] who showed that ball milling Ta in a H_2 atmosphere could result in the hydrogenation of the metal. Localized heating at media collision points was enough to diffuse H_2 into the material.

1.3 Hexagonal-Close-Packed Ta_2C Phase

Tantalum hemicarbide (Ta_2C) can exist in two states: (a) the ordered α-Ta_2C, and (b) the disordered β-Ta_2C. In both states the Ta atoms are arranged in the hcp crystal structure with a stacking sequence of ABABAB (see Figure 1.3) and a space group *Im3m*, and with carbon atoms taking up half of the octahedral interstices. The lattice parameters of the α-Ta_2C phase range from 3.100 to 3.102 Å for the *a* parameter and 4.931 to 4.940 Å for the *c* parameter. Since a large fraction of the octahedral sites are not occupied by the carbon atoms, the lattice can accept extra atoms without distorting and without significantly changing its lattice parameters [15].

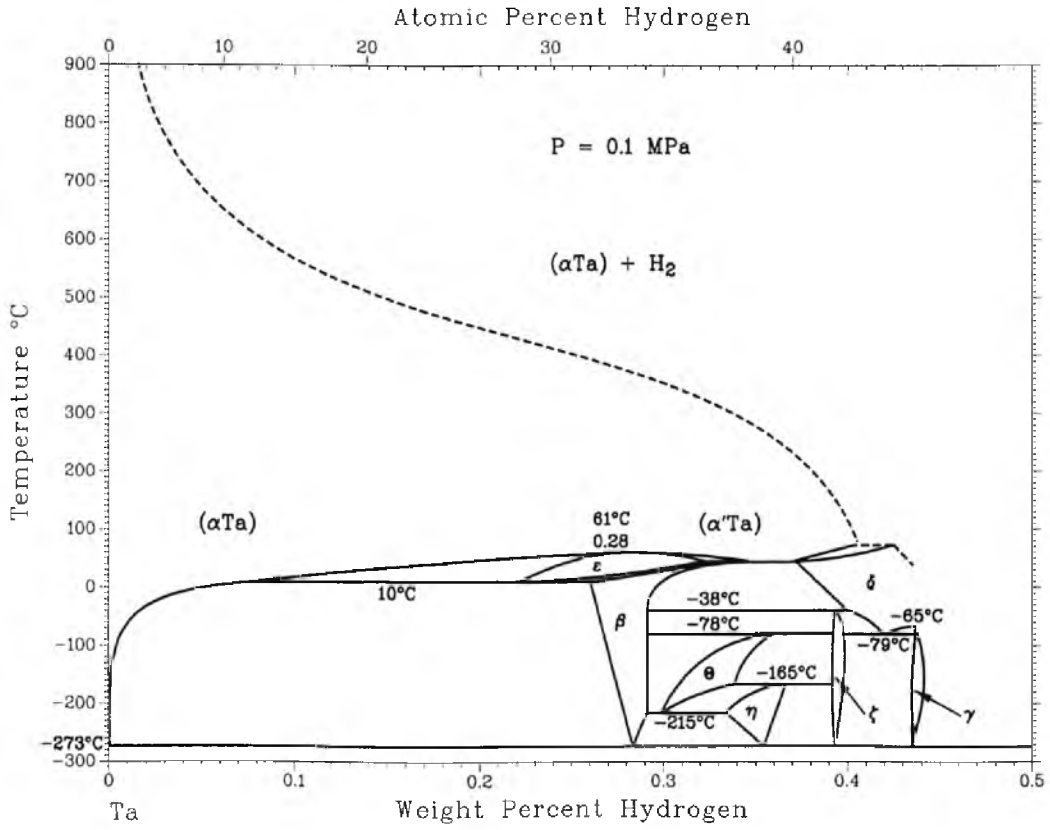

Figure 1.2 Phase diagram of the Ta-H system reported by San-Martin and Manchester [44, 47]. Reprinted with permission of ASM International. All rights reserved. www.asminternational.org

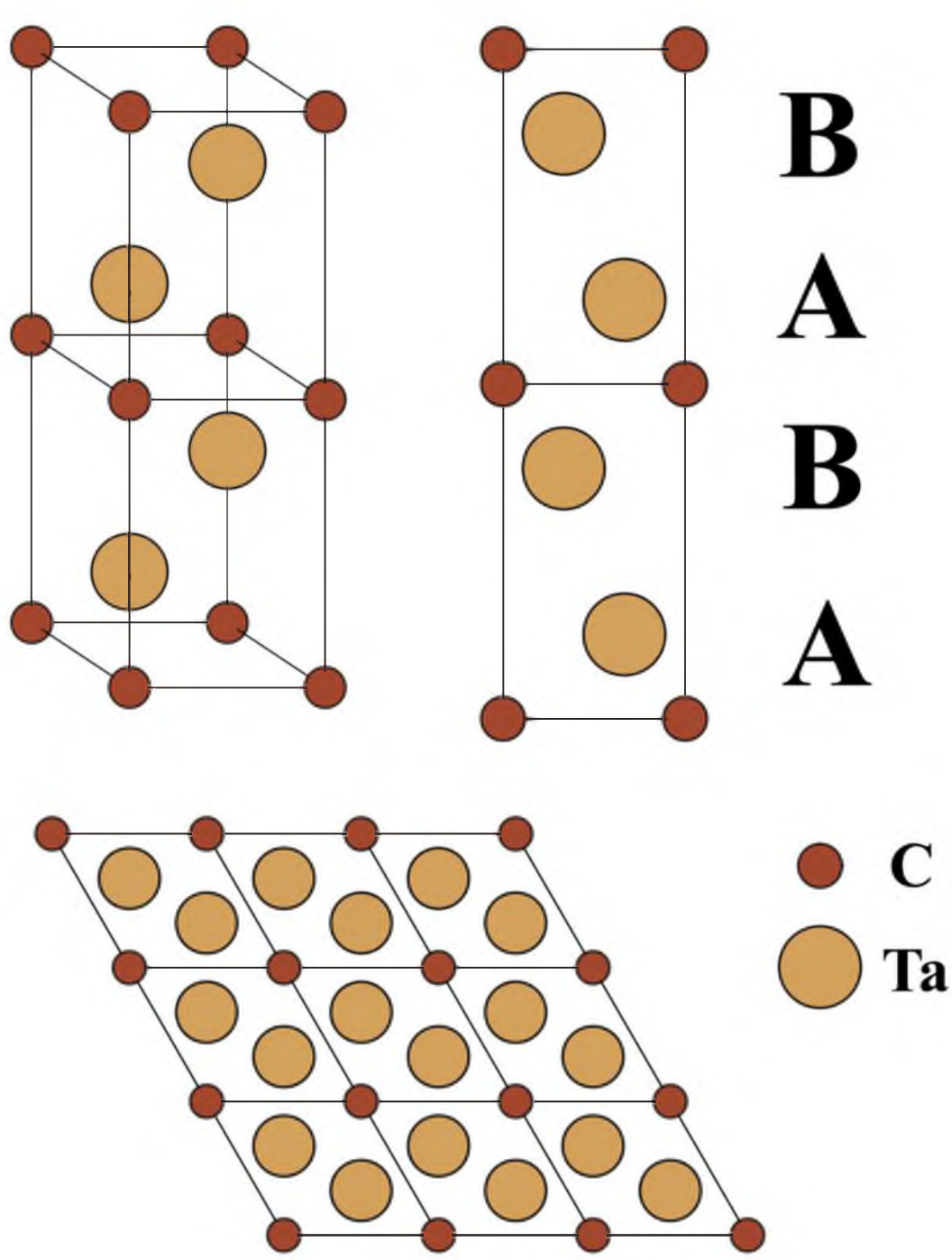

Figure 1.3 Illustration of the *hcp* α-Ta_2C phase showing its ABABAB Ta stacking sequence.

The α-Ta_2C phase (see Figure 1.1) exists from RT to approximately 1527°C and C/Ta atomic ratio from 0.44 to 0.5. Above 1527°C, the ordered α-Ta_2C transforms to the disordered β-Ta_2C phase. This order-disorder transformation pertains to the carbon atoms being ordered or disordered in the octahedral sites.

α-Ta_2C powder can be produced by combustion synthesis of Ta and carbon black powder mixtures [50], or it can be synthesized *in situ* during consolidation of Ta and TaC powder mixtures by hot pressing (HP), hot isostatic pressing (HIP) [9, 12, 14, 15], or spark plasma sintering [16]. Yeh and Liu [50] synthesized α-Ta_2C_y powder by self-propagating high-temperature synthesis (SHS) of Ta and carbon black using a Ti/carbon black ignition enhancer and a tungsten coil igniter. Samples were reacted in a stainless steel chamber and in high purity argon atmosphere. The effect of preheating temperature (100°C or 200°C) and compact green density were studied. It was found that reaction kinetics (flame-front propagation velocity) were enhanced when the green density was increased from 30% to 45% of theoretical density. At 30% theoretical density, the reaction products contained TaC as an intermediate phase, while compacts at 45% theoretical density were fully reacted. The activation energy associated with the α-Ta_2C synthesis, estimated by measuring the velocity of the propagating wave front, was found to be 299.3 kJ/mol. Compacts with higher green density had a faster propagating wave front than lower density green bodies.

Alexandre *et al.* [15] and De Leon *et al.* [12] fabricated α-Ta_2C_y materials for mechanical and creep testing, respectively, by HIPing Ta and TaC powder mixtures. Alexandre *et al.* HIPed billets of various compositions, with C/Ta atomic ratio ranging from 0.45 to 1. Powders were cold isostatically pressed at 230 MPa for 1 min reaching a

green density of 65% of theoretical density. The green compacts were then encapsulated in carbon-lined titanium containers, degassed in vacuum at 600°C before sealing, and HIPed at 1630°C at 195 MPa for 2 hr. Some compositions were further HIPed for an hour at 1950°C and 195 MPa. The HIPed materials reached greater than 98% theoretical density. Fracture toughness measured using the single edge notched beam (SENB) method was K_{1c} = 9.3 MPa$\sqrt{m}$ for the stoichiometric hemicarbide [15].

De Leon *et al.* [12] produced test bars for elevated temperature deformation studies by HIPing $Ta_2C_{0.94}$ billets from TaC and Ta powder mixtures at 200 MPa in an argon atmosphere at 1600°C. Test bars were cut into 3 mm x 4 mm x 45 mm dimensions and tested using a four-point flexural test at 1930°C in a graphite furnace and flowing argon. Basal and nonbasal dislocation slip and stacking faults were the two major deformation mechanisms in the α-Ta_2C materials. High resolution transmission electron microscopy determined that stacking faults were between Ta-Ta bonds and not Ta-C bonds. First principle calculations determined the stacking fault energy between Ta-Ta layers to be 3.5 eV and about 30 eV for Ta-C basal planes; an order of magnitude difference in energy [12].

Liu *et al.* [16] studied the mechanical properties and microstructures of spark plasma sintered α-Ta_2C. The rapid heating and cooling (~600°C/min and ~400°C/min, respectively) of Ta and TaC powder mixtures at 40 MPa of pressure in vacuum obtained greater than 95% theoretical density at temperatures as low as 1500°C when sintered for 60 min. Densification began at temperatures of 1300°C and it was determined that α-Ta_2C formation took longer than the densification process. An elongated microstructure started to form at 1700°C with grain aspect ratios of approximately 4.3. At temperatures

of 1900°C, small grains coalesced to form equiaxed clusters trapping pores at grain boundaries and preventing complete densification. The Vickers hardness, Young's modulus, and fracture toughness of the α-Ta_2C materials continually increased with increasing relative density reaching 11.8 GPa, 493 GPa, and 6.4 MPa√m, respectively, for the material sintered at 1900°C for 5 min and having a relative density of 97.5 %.

1.4 Rhombohedral ζ-Ta_4C_{3-x} Phase

The rhombohedral ζ-Ta_4C_{3-x} phase was first detected by R. Lesser and G. Brauer in 1958 when additional x-ray diffraction peaks were observed in compositions that were supposed to contain only hexagonal and cubic phases. The existence of ζ-Ta_4C_{3-x} was not confirmed until 1966 when I. Zaplatynsky [51] observed the phase in a two phase region of a partially-carburized Ta rod consisting of γ-TaC_y and ζ-Ta_4C_{3-x} between single phase regions of γ-TaC_y and α-Ta_2C. In order to produce enough ζ-Ta_4C_{3-x} a high-purity solid tantalum cylinder was carburized at 2300°C in vacuum and in direct contact with graphite powder. Half the cylinder was used to identify the various phases. The other half was ground in such a way as to remove the single phase γ-TaC_y and Ta_2C regions leaving only the γ-TaC_y and ζ-Ta_4C_{3-x} two-phase region. The two-phase region exhibited strong ζ-Ta_4C_{3-x} diffraction peaks prior to comminution to a 200-mesh powder. Upon comminution, however, the intensity of the peaks greatly diminished. Zaplatynsky concluded that ζ-Ta_4C_{3-x} is not an equilibrium phase but forms by diffusionless transformation from carbon deficient γ-TaC_y as a result of compressive stress induced by cooling and the difference in the coefficients of thermal expansion of γ-TaC_y and α-Ta_2C. It was thought grinding released the stress and transformed ζ-Ta_4C_{3-x} back to the cubic

phase.

The ζ-Ta_4C_{3-x} phase was isolated in 1967 by W.F Brizen and J.M. Tobin [52] when sufficient powder was obtained from microdrilling a narrow band of single phase ζ-Ta_4C_{3-x} formed by carburizing tantalum metal slabs in lampblack at long times between 1600°C and 2200°C . The ζ-Ta_4C_{3-x} phase was sandwiched between two phase regions containing either α-Ta_2C or γ-TaC_y and ζ-Ta_4C_{3-x}. The thickness of the ζ-Ta_4C_{3-x} layer could be increased by increasing annealing times or alternately carburizing and decarburizing the metal slabs. Using microprobe measurements the C/Ta ratio of three phases were estimated as 0.50, 0.71 and 0.74 for α-Ta_2C, ζ-Ta_4C_{3-x}, and γ-TaC_y, respectively. Samples sintered at 2300°C or higher contained two phase regions of α-Ta_2C or γ-TaC_y and ζ-Ta_4C_{3-x}.

The crystal structure of the ζ-Ta_4C_{3-x} phase was identified in 1970 by K. Yvon and E. Parthé [53] using single-crystal diffraction method. Identified as a trigonal (rhombohedral) structure, the unit cell consists of 12 close packed metal planes with a stacking sequence of ABABCACABCBC, a space group of $R\bar{3}m$, and with carbon atoms randomly occupying octahedral interstices (see Figure 1.4). The stacking sequence of the ζ-Ta_4C_{3-x} phase is a combination of both the *hcp* and the *fcc* (α-Ta_2C and γ-TaC_y) stacking sequences and can be considered a transitional crystal structure between the hemicarbide (α-Ta_2C) and the monocarbide (γ-TaC_y). The lattice parameters of the ζ-Ta_4C_{3-x} phase are 3.1216 Å for the *a* parameter and 30.058 Å for the *c* parameter [1].

Tantalum carbides containing significant weight fractions of the ζ-Ta_4C_{3-x} phase have been prepared by pressureless sintering [1], spark plasma sintering [5], hot-pressing [3, 4], and HIPing [24, 25]. Gusev *et al.* [1] pressureless sintered compacts of carbon

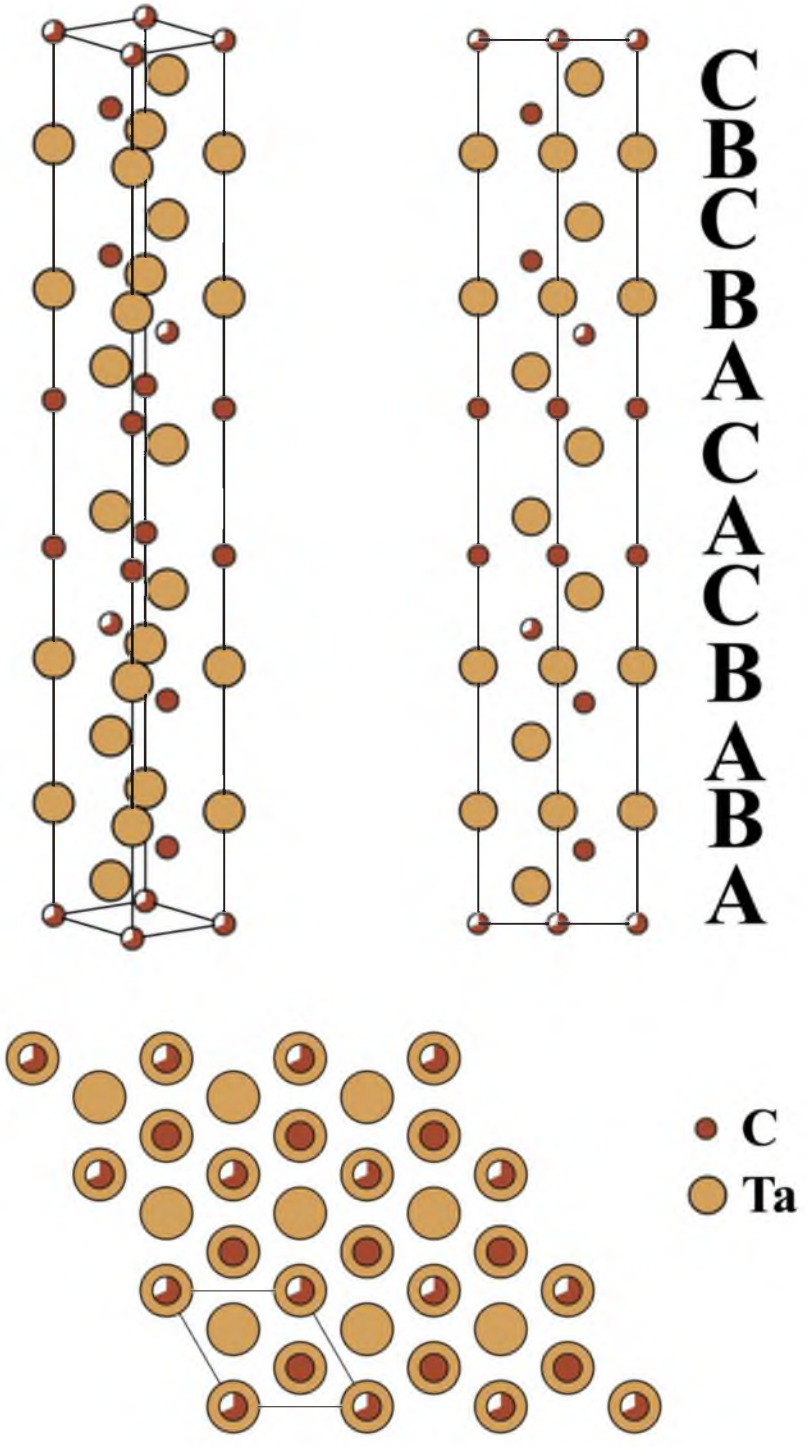

Figure 1.4 Illustration of the rhombohedral (trigonal) ζ-Ta_4C_{3-x} phase showing its ABABCACABCBC Ta stacking sequence.

black and powders of $TaC_{0.975}$ or $TaC_{0.75}$ at temperatures of 2000°C to 2130°C for 6 hr, with intermediate grinding after 3 hrs of sintering, for the purpose of determining atomic and vacancy ordering in the ζ-Ta_4C_{3-x} phase. One sample with a C/Ta atomic ratio of 0.685 produced a three phase powder containing 20 w% γ-TaC_y, 5 w% α-Ta_2C, and 75 w% ζ-Ta_4C_{3-x}, respectively. Results of the study indicated that the ζ-Ta_4C_{3-x} phase is stable from room temperature to approximately 2130°C, has a narrow homogeneity from $TaC_{0.65}$ to $TaC_{0.68}$, ordering of the carbon sublattice, and a significantly lower hardness (H_v ~ 9 GPa for $TaC_{0.685}$) when compared to the γ-TaC_y phase (H_v ~ 21 to 24 GPa).

Hackett *et al.* [3, 4] hot-pressed mixtures of Ta and γ-TaC powders with C/Ta atomic ratios of 0.7 and 0.6 to greater than 96% theoretical density at 1800°C for 120 min without the use of sintering aids, but with approximately 0.25 w% Co contamination from WC-Co milling media. The fracture toughness as measured by SEPB and flexural strength measured in four-point-bend were shown to increase with increasing w% ζ-Ta_4C_{3-x}. The compositions corresponding to C/Ta = 0.7 and 0.6 produced two-phase composites containing 45 and 83 w% of the ζ-Ta_4C_{3-x} phase, and the γ-TaC_y (C/Ta = 0.7) or the α-Ta_2C (C/Ta = 0.6) phase as the balance. The composites exhibited fracture toughness of 7.9 and 12.7 MPa$\sqrt{m}$, and flexural strengths of 488 and 672 MPa for the 0.7 and 0.6 compositions, respectively. The fracture surfaces of the two materials containing ζ-Ta_4C_{3-x} phase were highly faceted with cleavage crack planes and steps.

The microstructures and mechanical properties of spark plasma sintered (SPS) tantalum carbides of nominal composition$TaC_{0.7}$ from Ta and TaC powders were recently studied by Liu *et al.* [5]. Densification occurred at temperatures ranging from 1600°C to 1900°C and the sintered materials contained small quantities of ζ-Ta_4C_{3-x}, which was

credited with enhancing the fracture toughness ($K_c \approx 13.8$ MPa$\sqrt{m}$). The study proposed a two-step process in which Ta and γ-TaC react to form substoichiometric γ-$TaC_{0.86}$ and α-Ta_2C_y, at 1600°C and then further react to form γ-TaC_y and ζ-Ta_4C_{3-x} above 1700°C.

The high fracture toughness of the ζ-Ta_4C_{3-x} phase has been attributed to its lamellar substructure. This substructure has not only been seen in etched microstructures [1, 5, 25, 51, 52, 54], and fracture surfaces [3-5], but also by the larger than theoretically predicted reflections of the (00*l*) x-ray diffractions peaks, along the *c*-axis of the ζ-Ta_4C_{3-x} phase which is an indication of a textured microstructure [1]. Morris *et al.* [23-25] investigated the nucleation and growth of the ζ-Ta_4C_{3-x} phase by vacuum plasma spraying, sintering, and HIPing of TaC. During vacuum plasma spraying the volatilization of carbon in the plasma can be controlled, allowing for the fabrication of Ta-C materials with varying C/Ta ratio. It was found that the ζ-Ta_4C_{3-x} phase nucleated on the close packed planes in both the α-Ta_2C_y, phase and the γ-TaC_y phase. When the ζ-Ta_4C_{3-x} phase nucleates within the γ-TaC_y grains it acquires a complex crisscrossing platelet morphology in which the platelets tend to intersect at approximately 70°, equal to the orientation angle between {111} planes in γ-TaC. The platelets can terminate by impinging into other platelets, continue through the platelet, or span the entire TaC grain. Furthermore, the authors concluded that since the ζ-Ta_4C_{3-x} phase precipitated after the TaC phase, the ζ-Ta_4C_{3-x} phase has no effect on the grain microstructure of the material. Conversely, when the ζ-Ta_4C_{3-x} phase nucleates within α-Ta_2C_y, grains it acquires a uniform parallel lamellar morphology, due to the single family of {0001} close-packed planes available in the *hcp* structure.

1.5 Face-Centered-Cubic γ-TaC Phase

The *fcc* γ-TaC_y phase consists of a highly symmetric cubic *B1*(NaCl)-type structure, with a stacking sequence of ABCABC (see Figure 1.5), a completely filled Ta sublattice, and a random distribution of carbon atoms and structural vacancies in the carbon sublattice [55]. The γ-TaC_y phase exists over a wide stoichiometry from a C/Ta ratio of 0.58 to 0.98 at 3327°C and from 0.98 to 1.00 at room temperature. The lattice parameter of γ-TaC_y as a function of carbon deficiency in the carbon sublattice was studied by Bowman [56]. The lattice parameter a as a function of the C/Ta ratio (X) from 0.710 to 0.994 is shown in Eq. 1.1.

$$a = 4.3007 + 0.1563X \tag{1.1}$$

Solving the equation for $TaC_{1.000}$ gives a lattice parameter a of 4.4570 ± 0.0010 Å. Though Bowman's experimental analysis corresponded well to the earlier work of Lesser and Brauer [57], there was significant deviation in the results of Smirnova and Ormont [58], Robins [59], and Kempter and Nadler [60], and was attributed by Bowman to be a result of inhomogeneity in their samples.

The $Ta_6C_{5\pm x}$ phase is an ordered form of the γ-TaC_y phase and is found between the ζ-Ta_4C_{3-x} phase and the disordered γ-TaC_y phase (see Figure 1.1) [55]. The $Ta_6C_{5\pm x}$ phase exists over a wide stoichiometry from a C/Ta ratio of 0.85 to 0.95 at room temperature and proceeds through a peritectoid reaction at 1157°C into the γ-TaC_y and ζ-Ta_4C_{3-x} phases. Ordering of the carbon sublattice requires prolonged annealing at 1330°C for times ranging between 5 and 35 hr and then cooling to 477°C at 0.16 to

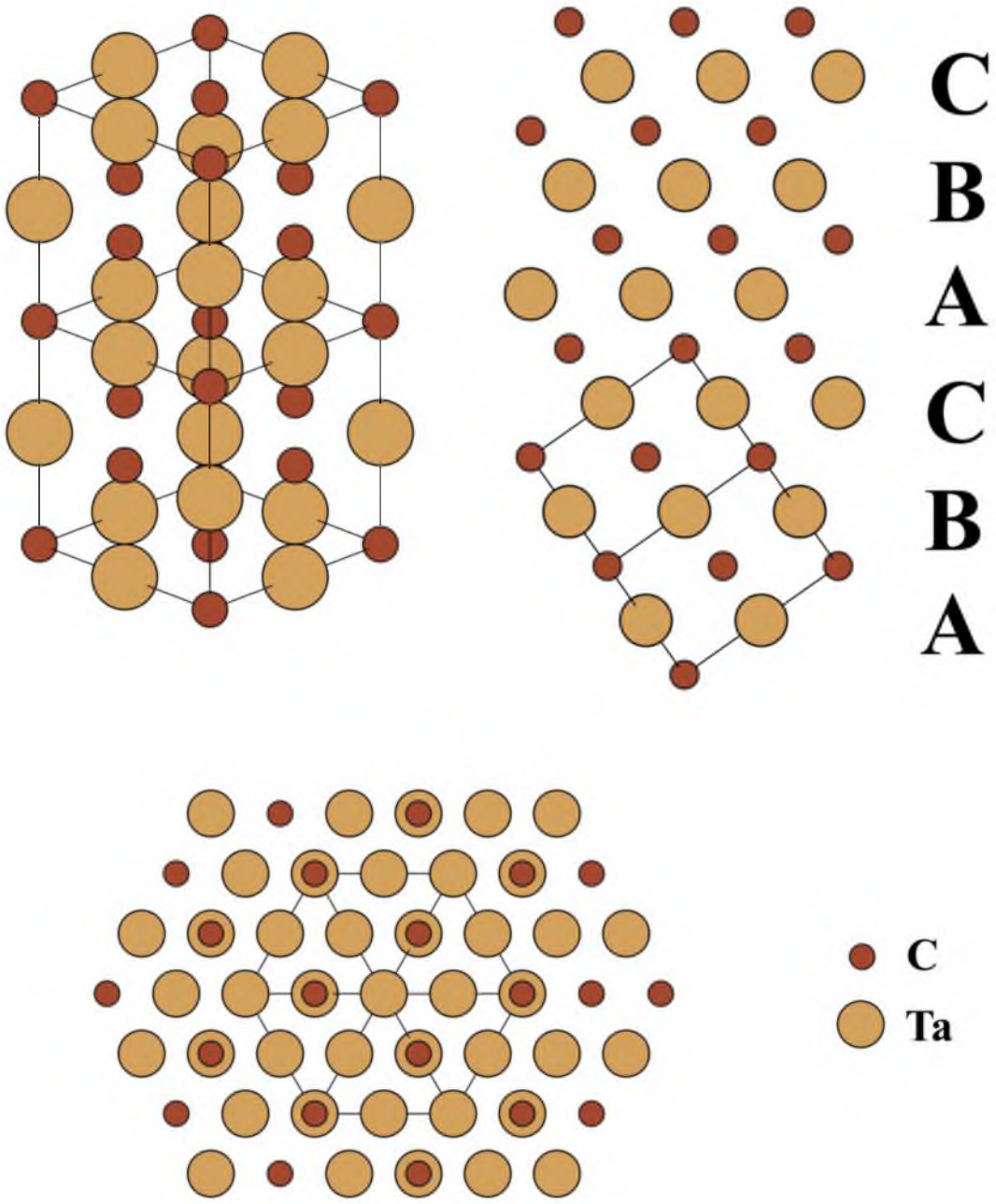

Figure 1.5 Illustration of the *fcc* γ-TaC_y phase showing its ABCABC Ta stacking sequence.

0.26°C/min and results in a small increase of the *B1* lattice parameter when compared to the γ-TaC_y phase[55]. Carbon ordering is not readily detected by XRD due to the significant difference in electron density between tantalum and carbon atoms. Instead, neutron diffraction is used to study carbon ordering in γ-TaC_y and $Ta_6C_{5\pm x}$. Superlattice reflections at around $2\theta \approx 20\text{-}23^\circ$ are an indication of ordering in γ-TaC_y. It was also found that rapid quenching could not prevent the ordering in the phase and that prolonged annealing would not result in a phase with long range ordering.

The TaC phase can be consolidated using a variety of methods including vacuum plasma spraying [61], hot-pressing [3, 4, 13], and HIPing [9, 14]. Zhang *et al.* [13] hot-pressed γ-TaC powder compacts at 30 MPa with sintering aids (B_4C powder and or phenolic resin) and without sintering aids at temperatures ranging from 1900°C to 2400°C. Without the addition of any sintering aids they obtained a density of 75% of theoretical density by hot-pressing at 1900°C, 85% of theoretical density at 2100°C, and 96% of theoretical density at 2400°C. With the addition of 0.78 w% C or 0.36 w% B_4C and 0.13 w% C the density increased to 87% and 96 % of theoretical density, respectively, when hot-pressed at 2100°C. Densification with sintering additives was accompanied by significant grain growth. The increase in density with the addition of sintering aids was attributed to the reaction of oxide layers (Ta_2O_5) with B_4C and C to form γ-TaC, B_2O_3, and CO byproducts. The grain sizes of γ-TaC hot-pressed at 2100°C without additives, with the addition of 0.78 w% C, and with the addition of 0.36 w% B_4C and 0.13 w% C were 1.3 μm, 9.0 μm, and 17.8 μm, respectively.

Hackett *et al.* [3, 4] hot-pressed compacts from Ta and γ-TaC powder mixtures with C/Ta atomic ratios of 1.0, 0.9, and 0.8 to greater than 96% theoretical density at

1800°C for 120 min. The hot-pressed compacts reached higher density at lower temperatures than Zhang *et al.* [13] and this was attributed to approximately 0.25 w% Co contamination from wear of the milling media. The mean grain sizes of the three compositions decreased with decreasing carbon content and were 7.7 ± 4.5, 6.4 ± 3.7, and 5.8 ± 2.4 μm, respectively, for the 1.0, 0.9, and 0.8 C/Ta atomic ratios. Flexural strength increased from 504.6 ± 88.2 MPa for the 0.8 composition to 655.3 ± 36.9 MPa for the 1.0 composition, while Vickers hardness decreased from 20.0 ± 0.5 GPa to 13.5 ± 0.2 GPa, respectively. Fracture toughness was low compared to materials containing the ζ-Ta_4C_{3-x} phase and were reported to be 3.8 ± 0.1 MPa√m for the 0.8 and 0.9 compositions and 5.3 ± 0.1 MPa√m for the 1.0 composition. The fracture toughness and hardness measurements for the 0.8 composition were comparable to those reported by Alexandre *et al.* [14] for a similar composition.

1.6 Slip Systems in Ta-C Phases

As can been seen in Figure 1.3 and Figure 1.4, the α-Ta_2C and ζ-Ta_4C_{3-x} crystal structures are composed of alternating Ta-C and Ta-Ta bonds along the basal plane. The α-Ta_2C structure has one group of Ta-Ta bonds located between the *A* and *B* planes. The ζ-Ta_4C_{3-x} structure has three groups of Ta-Ta bonds located between the *B* and *A* planes, the *A* and *C* planes, and the *C* and *B* planes. A theoretical examination of the slip system in α-Ta_2C, performed by Wang *et al.* [62] using density function theory, determined that slip follows a hierarchy system with the basal plane {0001}, prismatic plane $\{10\bar{1}0\}$ and the pyramidal planes $\{10\bar{1}\bar{1}\}$ and $\{10\bar{1}1\}$ composing the preferred slip systems with each of the four planes containing Ta-C and Ta-Ta layers. It was found that slip primarily

occurred on the basal plane along the $<11\bar{2}0>$ direction, providing two degrees of freedom, while pyramidal slip $\{10\bar{1}1\}$ along the $<\bar{2}113>$ direction would be the next probable slip system, supposedly becoming more prevalent at higher temperatures, providing an addition two degrees of freedom. Within the basal plane, slip was easier between the Ta-Ta metallic layers, which have a spacing of 2.41 Å, than between Ta-C layers, which have a spacing of 1.25 Å. The second most likely slip system, the $\{10\bar{1}1\}$ plane along the $<\bar{2}113>$ direction also corresponding to the Ta-Ta layers, also contains the second largest interplanar spacing. It thus appears that Ta-Ta layers of large spacing play a major role in the ductile properties of not only the α-Ta_2C crystal system but must also play a major role in the ζ-Ta_4C_{3-x} crystal system. The γ-TaC structure, on the other hand, does not contain any Ta-Ta bonds and has a Ta-C bond spacing in the basal plane of 1.29 Å making plastic deformation more difficult.

1.7 Toughening Mechanisms in Ceramics

There are two primary mechanisms that can increase a cracks resistance to growth: a) crack tip deflection, and b) crack tip shielding [63]. Both of these mechanisms can be engineered with modifications to a material's microstructure and both have been extensively researched. In crack tip deflection, regions of weakness such as grain boundaries, anisotropy in single crystals, and fibrous or plate-like microstructure cause a propagating crack to tilt or twist by some angle away from its initial direction, increasing the applied stress intensity needed for further propagation. Investigations by Faber *et al.* [64] for deflections by spheres, rods, and discs found that the increase in fracture toughness depended on particle shape and density of the particles and not by particle size

[63].

In crack-tip shielding, a material's resistance to crack growth is enhanced by reduction of the crack-tip stress intensity by one of the following mechanisms: a) bridging of cracks by ligaments, b) transformation toughening, or c) microcracking [63]. In ligament bridging, a secondary phase such as fibers, whiskers, or anisotropic (elongated) grains bridge the crack and the crack-closure tractions applied by the ligaments reduce the crack-tip stress intensity. In hot-pressed SiC-platelet/Al_2O_3 composites, where the volume fraction of SiC was 0.3, microstructural observations showed both crack deflection and grain bridging (frictional bridging and ligament bridging) were the dominant toughening mechanisms [65]. Since the composite materials contained randomly distributed SiC-platelets oriented along one directions, it allowed for three unique crack propagating directions to be explored. As a result it was shown that crack deflection was the dominant toughening mechanism and contributed to a total fracture toughness of 7 to 8 MPa$\sqrt{m}$. In an in-depth study of the toughening mechanisms of reinforced silicon nitride ceramics it was shown that the microstructure, specifically the grain size of needlelike β-Si_3N_4 grains within the bulk α-Si_3N_4 matrix, played a critical role in the reinforcement and ultimately the fracture toughness of the materials [66]. Materials with a large volume fraction of grains with aspect ratios greater than 4 had fracture toughness greater than 8 MPa$\sqrt{m}$, while samples without such grains had fracture toughness of 6 MPa$\sqrt{m}$. Microstructures with needlelike β-Si_3N_4 grains of diameter smaller than 1 μm exhibited elastic bridging and pull-out, while larger diameter grains primarily contributed to crack deflection. Frictional bridging was seen regardless of needlelike grain size.

1.8 R-Curve Behavior in Ceramics

Fracture toughness, when measured continuously as a function of crack extension, can provide valuable information about a material's resistance to fracture. Materials that show increasing crack growth resistance (K_R) with crack extension, such as polycrystalline ceramics with elongated grains, are said to have a rising R-curve and tend to exhibit narrow strength distributions and high reliability [67-70]. In materials that exhibit R-curve behavior there are two criteria required for a crack to extend under stable conditions. In the first, the crack-driving force must be equal to the crack-growth resistance as indicated in Eq (1.2):

$$K_a(a) = K_R(a) \tag{1.2}$$

In Eq. (1.2) $K_a(a)$ is the applied stress intensity for a crack of length a, and $K_R(a)$ is the crack-growth resistance. The second criterion, which defines stable crack-growth, is defined in Eq. 1.3.

$$\frac{dK_a(a)}{da} < \frac{dK_R(a)}{da} \tag{1.3}$$

Figure 1.6 illustrates plots of applied stress intensity, $K_a(a)$ (black dashed lines) as function of crack length at five loads for an SEPB test specimen. Also shown in the figure is a hypothetical crack-growth resistance curve ($K_R(a)$) (red line). In the figure, a_o represents the initial crack size; a_1 represents a critical crack length at which, when a force of P_3 is applied, the applied stress intensity, $K_a(a)$, and crack growth resistance,

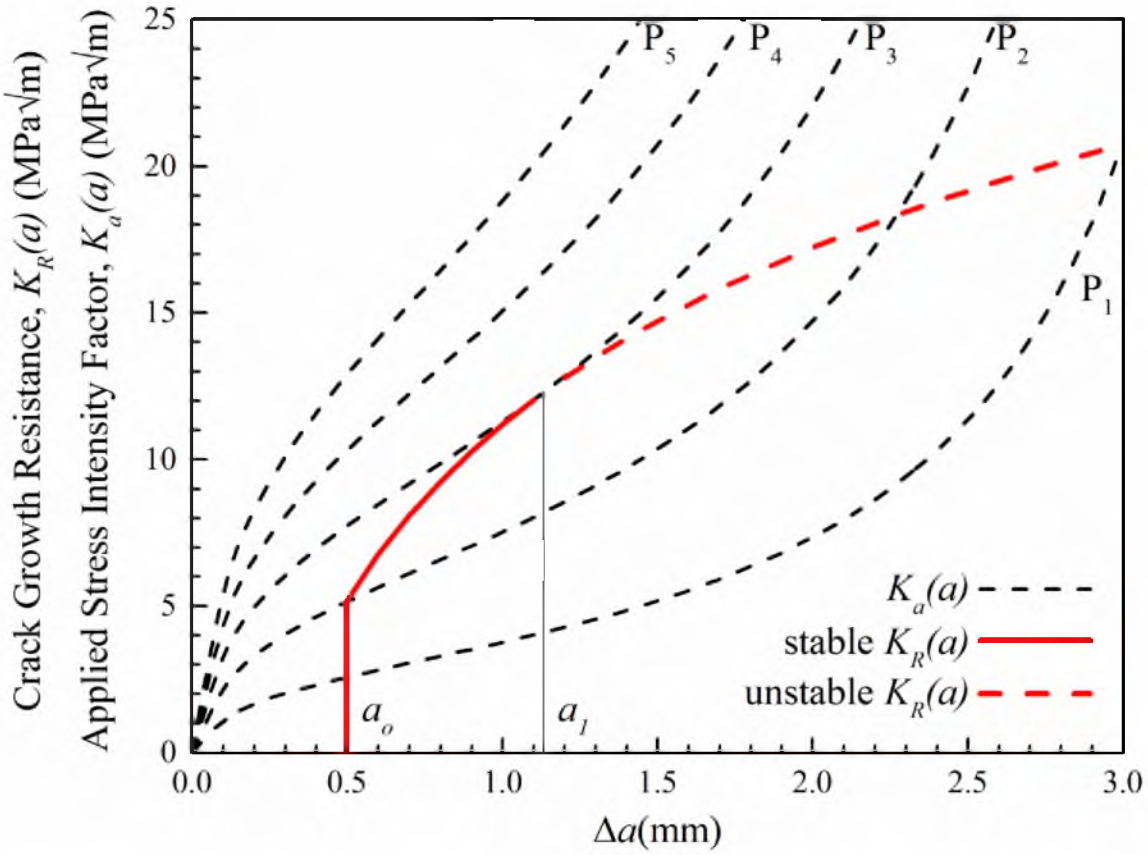

Figure 1.6 Illustration of a crack growth resistance ($K_R(a)$) R-curve overlaid on top of applied stress intensity factor ($K_a(a)$) curves.

$K_R(a)$ are equal, satisfying Eq. 1.2 for stable crack growth. Additionally, the slope of $K_R(a)$ is equal to $K_a(a)$. Crack growth between a_0 and a_1 would satisfy Eq. 1.3 for stable crack growth and as a result a crack would grow stably. For crack lengths greater than a_1, the slope of $K_R(a)$ is less than that of $K_a(a)$ and therefore does not satisfy Eq. 1.3 for stable crack growth. As a result a crack would grow unstably. Illustrations like Figure 1.6 can be used to determine the loading condition that will maintain stable crack growth. The applied stress intensity curves depend not only on applied load, but also crack size and shape, specimen geometry, and testing configuration. The crack-growth resistance curve is dependent on the mechanism of toughening, the microstructural changes that occur at the crack tip as a result of crack growth, and specimen configuration.

The high fracture toughness of ζ-Ta_4C_{3-x} is believed to be the result of toughening mechanisms very similar to those seen in Ti_3XC_2 (X = Si, Al) materials [17-22]. A side by side examination of indented Ti_3SiC_2 and Ta_4C_{3-x} materials, as reported by El-Raghy *et al.* [19] and Hackett [4], respectively, show similar characteristics. Indented Ti_3SiC_2 showed no median or lateral indentation cracks common in many structural ceramics. Delamination and crack deflections on and along the basal planes were observed along with debonding, pullout, and deformation of single grains. The authors also reported that a significant number of the delaminated grains buckled in a manner as to produce "wavy" or "kinked" grains [19]. The ability to buckle grains without fracturing the lamella was given as evidence that the Ti_3SiC_2 microstructure had microscale plasticity at room temperatures [19]. Hackett's observation of indented $TaC_{0.7}$ and $TaC_{0.6}$ microstructures that contained 45 w% and 83 w% ζ-Ta_4C_{3-x}, respectively, showed significant delamination and crack deflection (cleavage cracks) on and along basal plans, grain

breakup, and buckling [3, 4]. High magnification images were not obtained, so the "wavy" or "kinked" grain morphology and evidence of microscale plasticity was not established. Materials containing only the fcc TaC_y phase with compositions of $TaC_{0.8}$, $TaC_{0.9}$, and $TaC_{1.0}$ had median cracks propagating away from the corners of the indentations. Both intergranular and trans-granular crack propagation was observed.

With a nano-lamellar subgrain structure and very high fracture toughness, the ζ-Ta_4C_{3-x} phase is expected to exhibit rising R-curve behavior and a number of toughening mechanisms, including crack-wake bridging, and frictional pullout, similar to what is seen in fine grained and course grained Ti_3SiC_2 [20]. Coarse-grained Ti_3SiC_2 consisting of grains 50 – 200 μm in diameter and 5 – 20 μm in thickness exhibited higher fracture toughness than fine-grained Ti_3SiC_2 microstructures consisting of grains 3 - 10 μm in diameter and approximately 3 μm in thickness [20]. R-curve for a fine-grained material with an initial crack size of 10 mm in a compact-tension specimen started at ~8 MPa√m and increased to ~9.5 MPa√m following approximately 1.5 mm of crack extension. For the coarse-grained material, initial crack size appeared to affect the initial toughness. For an initial crack size of 8.3 mm, R-curve started at ~8.5 MPa√m and increased to ~14 MPa√m following approximately 4 mm of crack extension, while for an initial crack size of 13 mm R-curve started at ~11 MPa√m and increased to ~16 MPa√m following approximately 2.7 mm of crack extension [20].

CHAPTER 2

EXPERIMENTAL PROCEDURES

2.1 Introduction

The experimental procedures are grouped in four sections: Powder preparation, powder compaction for pressureless sintering of Ta and TaC powder, consolidation of Ta and TaC powder mixtures, materials characterization, and mechanical testing. The powder preparation section covers the hydrogenation and the milling of Ta, TaH_x, and TaC powders. The powder compaction for pressureless sintering section describes the compaction techniques used to make pellet and billet samples from milled compositions. The section on consolidation describes the conditions used in pressureless and pressure-assisted sintering, and the conditions used for the kinetic analysis of powder reactions and compact densification. The materials characterization section describes all the non-mechanical characterization techniques and equipment used to study powders and densified compacts while the materials testing section described hardness, fracture toughness, flexure strength, and R-curve testing procedures and testing equipment.

2.2 Powder Preparation

A Ta metal powder (Grade 73MR-0001, Inframat Advanced Materials LLC, Manchester, CT) and a γ-TaC powder (Grade 100, Global Tungsten & Powders Corp,

Towanda, PA) were used as the starting powders to react and produce ζ-Ta_4C_{3-x}. Use of γ-TaC powder as the carbon source instead of carbon powder is preferred because it provides better control of chemistry by limiting carbon volatilization during pressureless sintering. Secondly, tracking of carbon weight fraction during heating and sintering is also not very accurate due to its low atomic weight and weight percent relative to γ-TaC. The Ta powder was reported to be 99.95 % pure with oxygen (500-1800 ppm) and niobium (<50 ppm) as the major impurities. The mean particle size was in the range, 5-10 μm. The γ-TaC powder was reported as containing major impurities of tungsten (300 ppm), niobium (340 ppm) and oxygen (970 ppm). The mean particle size was 0.9 μm.

As will be discussed in Chapters 3 and 4, the ductility of the Ta powder resulted in an agglomerated powder that suppressed densification during pressureless sintering and limited the amount of ζ-Ta_4C_{3-x} phase formed. The need to develop a pressureless sintering method required a Ta powder that was both equiaxed in particle morphology and small in particle size. To achieve these goals, Ta powder was hydrogenated and embrittled prior to comminution. Ta powder with 0.03 w% $PdCl_2$ catalyst (Cat. No.: AC19520-0250, Fisher Scientific, Pittsburgh, PA) or 0.04 w% $Pd(NO_3)_2$ catalyst (Product No.: 11035, Alfa Aesar, Ward Hill, MA) were mixed by shaking in a polyethylene (PE) bottle with acetone as the medium. Hydrogenation of the dried Ta powder was carried out in a stainless steel chamber. The chamber was heated to and held at 300-350^{o}C for 4 to 8 hr in flowing ultra-high purity (99.99%) hydrogen gas. The sample was cooled to room temperature in flowing hydrogen. The powder was then poured into an acetone bath to avoid spontaneous reaction with air. The powder-acetone mixture was left to dry in air.

To compare particle size reduction and change in particle morphology during

comminution, samples of the as-received and H_2-treated Ta powders were separately ball-milled (Model SPEX/CertiPrep 8000 Mixer/Mill, SPEX Sample Prep, Metuchen, NJ) in hexane for 15 min in a 55ml WC-Co lined crucible with powder to WC-Co media (3/16" Tungsten Carbide Satellites, Union Process, Akron, OH) weight ratios of 1:10, 1:25, and 1:50. In addition to studying the effect of hydrogenation and comminution on Ta powder morphology, two Ta metal sheet specimens, 8 x 8 mm in dimension, polished to a 1 μm finish were hydrogenated as previously described. One sheet specimen was coated with a thin layer of $Pd(NO_3)_2$ catalyst by dissolving it in acetone, dripping onto the polished surface and letting it to air dry. The other Ta sheet specimen was not treated.

As-received Ta powder and γ-TaC powder were milled at C/Ta atomic ratios of 0.5, 0.55, 0.625, and 0.66 by rolling in hexane in a 500 ml high-density poly(ethylene) (HDPE) jar and WC-Co media at 110 rpm for 8 hr. The powder to media weight ratio was 1:10. After milling, the mixtures were air dried and designated $TaC0.50^a$, $TaC0.55^a$, $TaC0.625^a$, and $TaC0.66^a$, respectively.

A second batch of powder of the C/Ta = 0.66 composition was prepared by milling a mixture of H_2-treated Ta powder and γ-TaC powder. The H_2-treated Ta powder was separately ball-milled in hexane for 60 min using a paint shaker (Model 1410, Red Devil Equipment Co., Plymouth, MN) in a 500 ml HDPE jar in hexane with powder to WC-Co media weight ratio of 1:10. After the addition of γ-TaC powder the mixture was balled-milled for an additional 60 min using the paint shaker under the same conditions. After milling, the mixtures were air dried. The powder batch was designated $TaC0.66^b$.

A third batch of powder of the C/Ta = 0.66 composition was planetary milled using as-received Ta powder and γ-TaC powder in hexane in a 500 mL ZrO_2 crucible and WC-

Co media at 300 rpm and 60 min. The powder to media weight ratio was 1:10. After milling, the mixture was air dried and designated $TaC0.66^{c}$.

2.3 Powder Compaction for Pressureless Sintering of Ta and TaC Powder Mixtures

Milled $TaC0.66^{a}$, $TaC0.66^{b}$ and $TaC0.66^{c}$ powders were uniaxially pressed into approximately 5 g pellets of 14.27 mm diameter at 280 MPa.

$TaC0.66^{a}$ pellets were sintered in Ar in a graphite furnace while resting on Mo sheets using a heating rate of 40°C/min and held isothermally at 1700°C and 1800°C for times of 600, 6000 and 60000 s. The pellets were cooled in Ar to room temperature.

To investigate and monitor the formation of transient phases by reaction of Ta and γ-TaC prior to forming the equilibrium ζ-Ta_4C_{3-x} phase, the $TaC0.66^{b}$ pellets were annealed in Ar in a molybdenum (Mo) furnace using a heating rate of 40°C/min and held isothermally from 900°C to 1300°C for 6000 s. From 1600°C to 1900°C pellets were sintered for 6000 s in a graphite furnace as described before. A second set of pellets was annealed at 900°C, 1000°C, 1100°C and 1200°C for times ranging between 0 and 60000 s to investigate the kinetics of the formation of the transient α-Ta_2C_y, phase. A final set of pellets was sintered at 1600°C, 1700°C, and 1800°C for times ranging between 0 and 60000 s to investigate the kinetics of formation of the equilibrium ζ-Ta_4C_{3-x} phase. All the pellets were cooled to room temperature in the Ar atmosphere.

A final set of pellets of the $TaC0.66^{c}$ material was sintered at 1675°C, 1700°C, 1730°C, and 1800°C for times ranging between 0 and 30000 s to investigate the kinetics of formation of the equilibrium ζ-Ta_4C_{3-x}. All the pellets were sintered as described

previously.

2.4 Consolidation of Ta and TaC Powder Mixtures

The $TaC_{0.50}$[a], $TaC_{0.55}$[a], $TaC_{0.625}$[a], $TaC_{0.66}$[a] powders were hot pressed into billets (45 mm x 45 mm x 5 mm) in an argon atmosphere using a heating rate of 25°C/min from room temperature to 1500°C and then heated to 1800°C at 7°C/min and held isothermally for 7200 s at a pressure of 28 MPa. The pressure was maintained while cooling to 800°C and further cooled to room temperature without the pressure. The billets were designated $TaC_{0.50}$[a](HP), $TaC_{0.55}$[a](HP), $TaC_{0.625}$[a](HP) and $TaC_{0.66}$[a](HP), respectively. A hot-pressed $TaC_{0.66}$[a](HP) billet was HIPed (American Isostatic Presses, Inc., Columbus OH) using a heating/cooling rate of 10°C/min from room temperature to 1800°C and held isothermally for 120 min at a pressure of 207 MPa. Pressure was held during heating and cooling at 207 MPa. The hot-pressed and HIPed material was designated $TaC_{0.66}$[a](HP+HIP).

For pressureless sintering, a mixture of the $TaC_{0.66}$[b] powder was uniaxially pressed into billets (70 mm x 70 mm x 7 mm) at 18.2 MPa pressure and then cold-isostatically pressed at 310 MPa. The billets were packed in γ-TaC powder and heated in a graphite-lined furnace at a rate of 6°C/min from room temperature to 350°C in vacuum and held for 20 min to degas hydrogen. The furnace was then backfilled with argon and heated at 25°C/min to 1500°C and then heated to 1900°C at 7°C/min and held isothermally for 100 min. The billets were cooled to room temperature in Ar and designated $TaC_{0.66}$[b](PS). A pressureless sintered billet was HIPed as previously described at 1800°C for 100 min. The pressureless sintered and HIPed billet was

designated TaC0.66[b](PS+HIP).

Billets were ground and cut (Quality Magnetics Corp, Compton, CA) to size B test bars (3 mm x 4 mm x 45 mm) as specified in ASTM standard C 1161-02c [71].

2.5 Materials Characterization

Following milling, the powder particle morphology was studied using a scanning electron microscope (SEM, Model S-3000N, Hitachi High Technologies America, Inc., Dallas, TX). Specific surface areas of the powder samples were measured by the gas-adsorption technique (Model Gemini V, Micromeritics Instrument Corp., Norcross, GA). Particle-size distribution was measured using a laser-diffraction particle-size analyzer (Model LS 230, Beckman Coulter, Inc., Miami, FL) in the Mie mode using suspensions of powders in a 50/50 w% water/glycerol solution.

Phase contents of all materials were assessed using an x-ray diffractometer (XRD, Model Philips X'Pert-MPD, PANalytical Inc., Westborough, MA). Prior to analysis pellets annealed from 900°C to 1300°C were pulverized using an alumina mortar and pestle. Pellets sintered at and above 1500°C had approximately 0.5 mm of top surface ground away and were polished to a 600 grit finish prior to XRD analysis. Crystalline phases present were identified and lattice parameters of the phases in the powder, pellet, and billet samples were measured using an XRD software (X'Pert High Score Plus, Version 2.2d, PANalytical, Almelo, Netherlands) and calculated by the Rietveld refinement method. Crystallographic structural data (powder diffraction file, ICDD, USA) for bcc Ta (space group $Im\bar{3}m$, JCPDS: 1-071-4641), hcp α-Ta_2C (space group $P\bar{3}m1$, JCPDS: 1-071-2677), fcc γ-TaC_y (space group $Fm\bar{3}m$, JCPDS: 1-071-6207),

tetragonal TaH_x (space group *I4/mmm*, JCPDS: 1-089-4074), hcp WC (space group $P\bar{6}m2$, JCPDS: 1-089-2727), and the hcp $Ta_{0.703}O_{1.65}$ (space group *P6/mmm*, JCPDS: 1-073-0005) were used. A crystallographic data card was constructed for the trigonal ζ-Ta_4C_{3-x} phase by referencing Gusev *et al.* [1] with a space group of $R\bar{3}m$ and initial lattice parameters of $a = b = 3.1216$ Å and $c = 30.058$ Å. Three carbon atoms at 3b, 3a, and 6c had atomic positions of (0,0,0), (0,0,0.5), and (0,0,0.4170) and occupancy factors of 0.6756, 0, and 1, respectively. Two Ta atoms at 6c had atomic positions of (0,0,0.1273) and (0,0,0.291) and occupancy factors of 1, respectively. Multiple refinement steps were carried out including scale factor, flat background, zero shift, lattice parameters, half-width, preferred orientation, peak shape parameters, and B isotropic in an effort to minimize the goodness of fit (GOF) parameter for any particular X-ray diffraction pattern. The H-contents of the tantalum hydrides, i.e., x in TaH_x, were estimated by comparing the lattice parameters of TaH_x as a function of x reported by San-Martin and Manchester [44].

The kinetics of phase formation was analyzed using a software (OriginPro 9.0.0, OriginLab Corporation, Northampton, MA). Data were analyzed using nonlinear curve fitting features of the software. Select samples were polished to a 0.1 μm finish and etched using a mixture of 20 mL H_2O, 5 mL HNO_3, 3 mL HCl, and 12 mL HF for approximately 60 to 90 s. Etched surfaces were examined by optical microscope. Grain size measurements and w% phase content were also studied using electron backscatter diffraction (EBSD) using a field emission gun scanning electron microscope (Phillips XL/30 FEGSEM, Eindhoven, Netherlands) equipped with a sensitive charge-coupled device (CCD) camera and EBSD software (OIM Analysis and Data Collection, Version

7, EDAX).

2.6 Mechanical Testing

Fracture strength was measured in four-point bending using type B specimens with a 40 mm support span and a 20 mm loading span as described in ASTM Standard C 1161-02.[14] The test fixtures used to apply load in four-point bending also conformed to the specifications of the standard. [71]. Fracture strength was calculated using Eq. 2.1:

$$\sigma_f' = \frac{3P(S_o - S_i)}{2bd^2} \tag{2.1}$$

where σ_f' is the apparent flexural strength, P is the breaking force, S_o is the length of the support span, S_i is the length of the loading span, b is the specimen width, and d is the specimen thickness. All the test specimens had a 45° chamfer of 0.12 mm size machined into the long edges to reduce edge stress concentration points. As a result of the chamfer the moment of inertia is reduced. Equation 2.2 was used to correct the flexural strength:

$$\sigma_f = F\sigma_f' \tag{2.2}$$

where σ_f' is the apparent flexural strength as calculated using Eq. 2.1, σ_f is the corrected flexural strength, and F is the correction factor calculated to be 1.0069 for a type B specimen with a 0.12 mm chamfer. Fracture toughness was measured by the single-edge precracked-beam (SEPB) test method as described in ASTM Standard C 1421-10 [72].

The SEPB tests used the same type B specimens as those used in the four-point bend tests. The specimens were precracked using three Vickers indents at a load of approximately 100 N, and a bridge compression loading fixture described in the standard. The initial crack was infiltrated with an ink to delineate the crack front and measure the initial crack length, a_0. The initial crack lengths were typically in the range, 1.5 to 2.4 mm. Both the four-point bend and the SEPB tests were conducted using a universal testing machine (Model 5969, Instron, Norwood, MA) with a 1 kN load cell. Fracture toughness was calculated using Eq. 2.3

$$K_{Ic} = \left[\frac{P[S_o - S_i]}{BW^{3/2}}\right]\left[\frac{3[a/W]^{1/2}}{2[1-a/W]^{3/2}}\right] f \tag{2.3}$$

where:

$$f = 1.9887 - 1.326[a/W] - \frac{\{3.49 - 0.68[a/W] + 1.35[a/W]^2\}[a/W]\{1-[a/W]\}}{\{1+[a/W]\}^2}$$

where K_{Ic} is the fracture toughness (MPa$\sqrt{}$m), B is the specimen dimension perpendicular to the crack length (m), W is the specimen dimension parallel to the crack length (m), and a is the crack length (m). Microhardness was measured using a Vickers indenter (Leco Model LM-100, St. Joseph, MI) at 0.49 N to 9.8 N with 15 sec hold time. Hardness was measured in accordance with ASTM standard E384-10$^{\varepsilon 2}$ [73]. Vickers hardness, H_V, in units of GPa, was calculated using Eq. 2.4:

$$H_v = 0.0018544\frac{P}{d^2} \tag{2.4}$$

where d is the mean diagonal length of the Vickers impressions in units of mm.

Crack growth resistance (K_R) was measured using SEPB specimens in four-point bending. A 0.3 mm deep notch was cut into the 3 mm wide side of the specimens placed in tension. Specimens were precracked as outlined in ASTM standard C 1421-10 [72] such that the initial crack length (a_o) was in the range, 1.1 to 2.1 mm. Bars were loaded in 0.5 N increments at 0.01 mm/min cross-head displacement rate and the displacement was held fixed for 5 seconds. If during the displacement hold the load dropped by more than 0.5 N, the specimen was unloaded and the crack length was measured using an optical microscope equipped with a micrometer specimen stage. From the minimum load at each fixed displacement and the corresponding crack length measured using an optical microscope, the applied stress-intensity factor was calculated.

CHAPTER 3

HYDROGENATION OF TANTALUM FOR EFFICIENT COMMINUTION

3.1 Introduction

This chapter reports the results of a study of hydrogenation of Ta metal powder and its beneficial effect on particle size reduction and morphology, and reduced agglomeration by milling. The kinetics of hydrogenation were significantly enhanced by the use of a palladium catalyst. Microhardness measurements on a hydrogenated Ta metal sheet confirmed the increased hardness and decreased fracture toughness of the hydrogenated metal relative to the untreated metal sheet.

3.2 Particle Size Reduction of Untreated and H_2-Treated Ta Powder

Table 3.1 compares specific surface areas (m^2/g) of four batches of untreated and H_2-treated Ta powders. The first batch consisted of as-received Ta powder and a sample of Ta powder that was H_2-treated, but not milled. The other three batches consisted of untreated and H_2-treated powder samples that were milled with powder to media weight ratios of 1:10, 1:25 and 1:50. In all four cases, the specific surface area was greater for the H_2-treated powder as compared to the untreated powder. For the H_2-treated powder,

Table 3.1 Specific surface areas (m^2/g) of four batches of untreated and H_2-treated Ta powders.

Powder to Media Weight Ratio	Specific Surface Area (m^2/g)	
	Untreated	H_2-Treated
Unmilled	0.14	0.17
1:10	0.27	0.69
1:25	0.28	0.78
1:50	0.35	0.82

the specific surface area increased from 0.17 m^2/g for the unmilled powder to 0.82 m^2/g for the powder sample milled with 1:50 weight ratio of the powder and the media. For the same conditions, the increase in surface area of the untreated Ta powder was from 0.14 m^2/g (unmilled) to 0.35 m^2/g for the powder sample milled with 1:50 weight ratio of the powder and the media.

Figures 3.1 and 3.2 show particle-size distributions of the H_2-treated powder and the untreated powder, respectively. In each figure, the particle size distributions are shown for the following: (a) unmilled powder, (b) powder milled with 1:10 weight ratio of the powder and the media, (c) powder milled with 1:25 weight ratio, and (d) powder milled with 1:50 weight ratio. Both the untreated and the H_2-treated powders showed shifts in the particle-size distributions of the milled powders to smaller particle sizes relative to the unmilled powders. There was, however, an interesting difference in the trends of the most probable particle size, i.e., the mode, of the two powders with the milling condition. In the unmilled state, the modes were 20 μm and 22 μm for the untreated and the H_2-treated powder, respectively. On milling with 1:10 weight ratio of the powder and the media, the mode of the untreated powder decreased to 9.4 μm, while the mode for the H_2-treated powder decreased to 5.9 μm. Thus, there was greater comminution of the H_2-treated powder than the untreated powder. Milling with increased ball-to-charge ratio did not benefit comminution significantly. For the H_2-treated powder, the mode decreased modestly to 4.9 μm and 4.4 μm for the powders milled with 1:25 and 1:50 weight ratios of the powder and the media, respectively. The untreated powder showed an unexpected trend. The mode increased from 9.4 μm to 12 μm and 16 μm as the weight ratio of the powder and the media was decreased from 1:10 to 1:25 and 1:50.

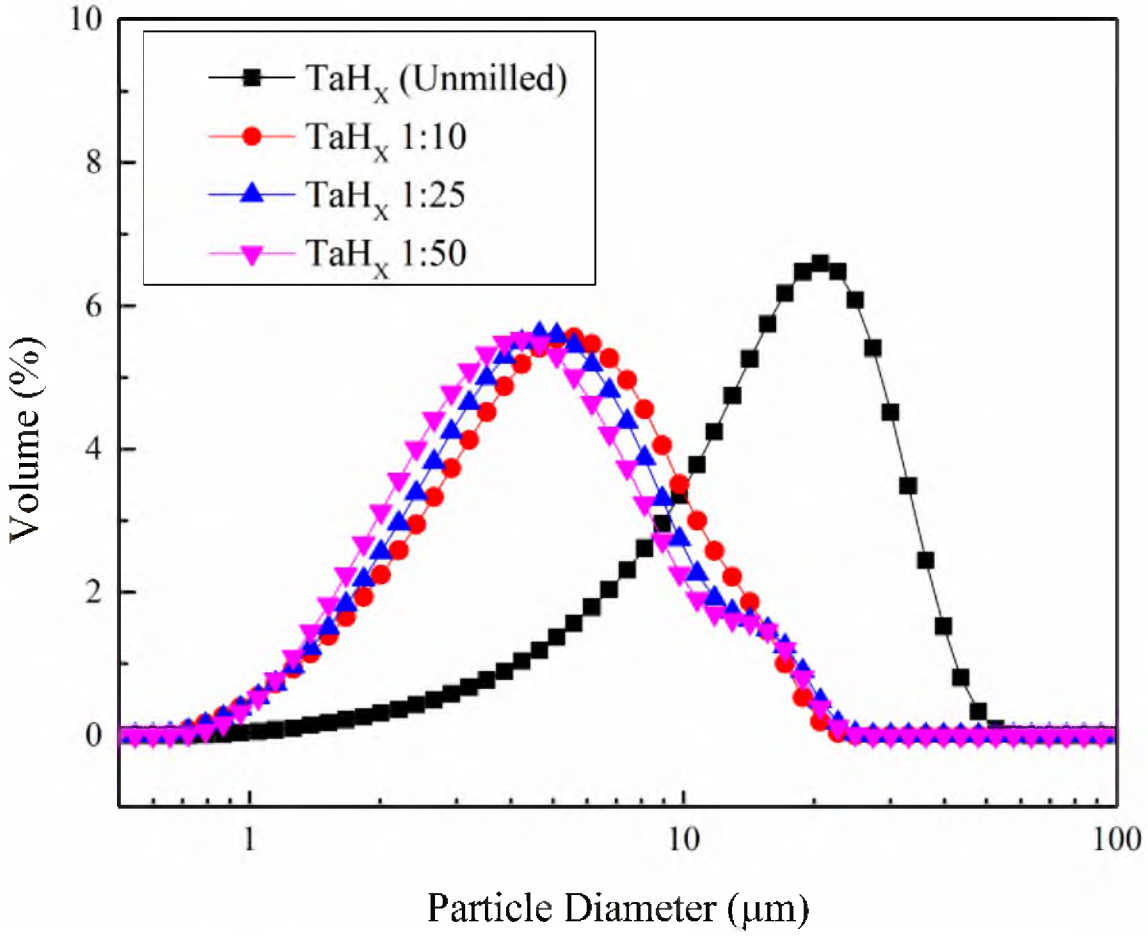

Figure 3.1 Particle size distributions of unmilled and milled, hydrogen-treated Ta powders as a function of powder to media weight ratio.

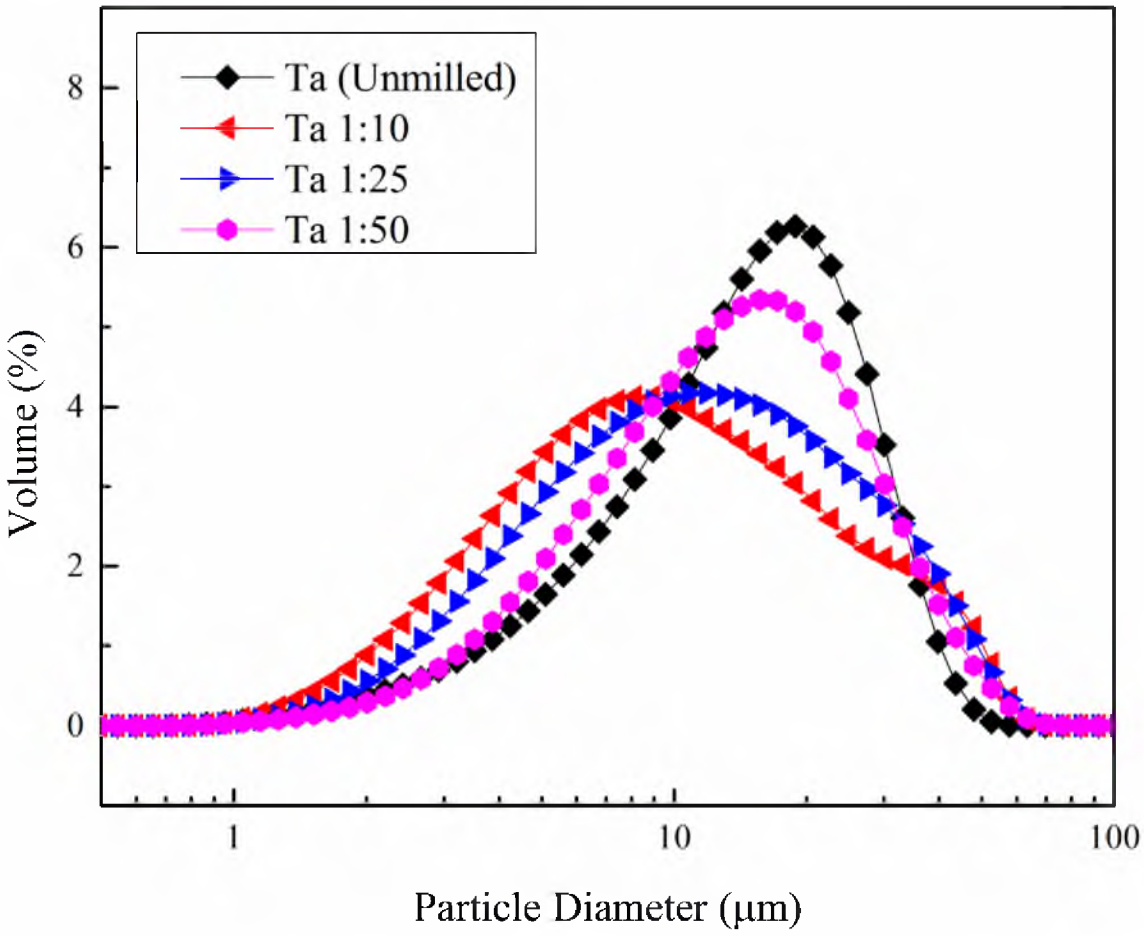

Figure 3.2 Particle size distribution of unmilled and milled, untreated Ta powders as a function of powder to media weight ratio.

This result suggests that milling Ta powder with higher weight ratio of the media results in increased deformations and flattening of the particles or possibly even welding of the particles.

SEM images of untreated, and H_2-treated Ta powders are shown in Figure 3.3. Both the as-received Ta powder and the H_2-treated, unmilled powder had similar powder characteristics. The powders consisted of agglomerates of two different sizes of primary particles, large polyhedral particles in the 5-10 μm size range, and small particles extending into the submicron size range. The small particles appeared to be equiaxed or nearly spherical in shape. A significant number of the agglomerates were linear chains of the large primary particles linked by grain boundaries. The measured particle size distributions of these powders reflected the size distributions of the agglomerates, with some ranging up to 60-70 μm. H_2-treated, unmilled Ta powder had similar agglomerate and primary particle morphologies with no indication of particle cracking as a result of H_2-induced phase transformation.

Untreated, milled Ta powders exhibited distinctly different particle shapes. Particles appeared flat, highly deformed, and varied greatly in size (see Figures 3.3(c) and 3.3(e)). Large plate-like agglomerates formed in all untreated Ta powders ranging in size upwards of 100 μm, as seen in Figure 3.3(e), for the untreated Ta powder milled with 1:50 weight ratio. The morphology of these particles appears closer to capacitor grade powder [31, 32] but would be undesirable for the sintering of high density bodies. H_2-treated, milled Ta powders had an equiaxed particle shape with a significant number of particles under 5 μm and few particles larger than 10 μm, as seen in Figure 3.3(d), for the H_2-treated Ta powder milled with 1:10 weight ratio. SEM images of the H_2-treated Ta

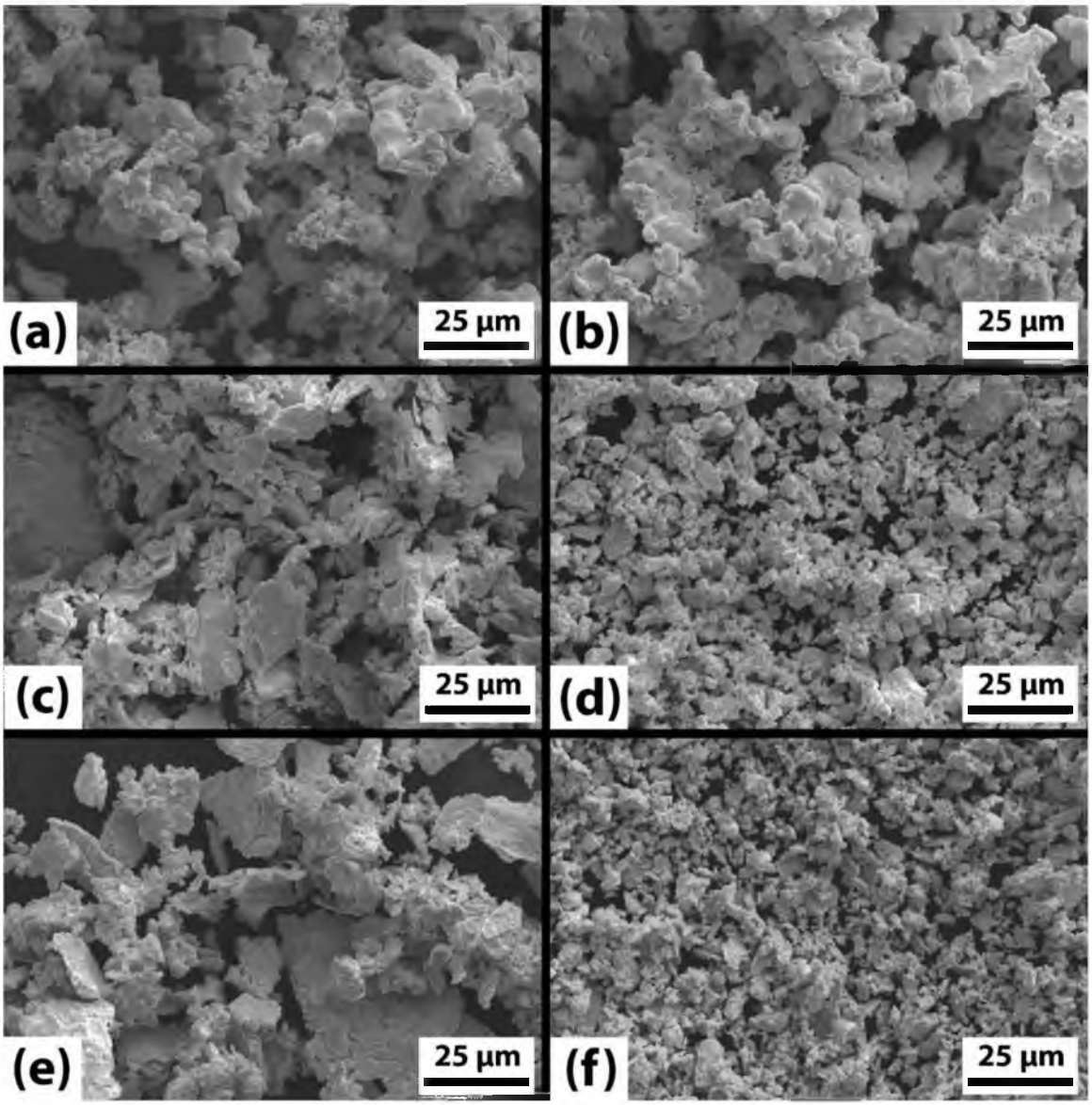

Figure 3.3 SEM images of (a) as-received Ta powder, (b) H_2-treated, unmilled Ta powder, (c) untreated Ta powder milled with 1:10 weight ratio of the powder and the media, (d) H_2-treated Ta powder milled with 1:10 weight ratio, (e) untreated Ta powder milled with 1:50 weight ratio, and (f) H_2-treated Ta powder milled with 1:50 weight ratio.

powder milled with 1:50 weight ratio showed that particles were generally more uniform in size and did not appear deformed or plate-like (see Figure 3.3(f)).

3.3 Phase Transitions in the H_2-Treated Ta

Figure 3.4 shows X-ray diffraction patterns of the untreated and the H_2-treated Ta powders in both the unmilled and the milled conditions. The diffraction pattern of the as-received Ta powder, Figure 3.4(a), could be identified as that of the bcc α-Ta with three peaks that could be indexed as (011), (002) and (112) lattice planes. The shoulders seen in the (002) and the (112) peaks are due to the $K_{\alpha 1}$ and the $K_{\alpha 2}$ radiations of the XRD copper target source. Any minority phases, if present, were below the detection limit of XRD. The Rietveld refinement estimated the lattice parameter of Ta as 3.305 Å. The diffraction pattern of the untreated, milled powder (Figure 3.4(b)) showed the three Ta peaks, but the peaks were broader when compared to the peaks of the as-received Ta powder. The broadening of the peaks is likely due to the deformation of the primary particles during milling. In addition to the Ta peaks, the milled Ta powder showed three minor peaks that were identified as belonging to hcp δ-WC. Ball milling with high powder-to-media weight ratio produces wear of the WC-Co media and the container. Rietveld refinement estimated the weight percent of WC as 11 with the balance being bcc α-Ta. The WC contamination can be minimized by tailoring the powder-to-media ratio, or eliminated completely by using TaC milling media.

The H_2-treated, unmilled Ta powder (see Figure 3.4(c)) showed three diffraction peak groups at Bragg angles slightly smaller than the peaks observed for the untreated Ta

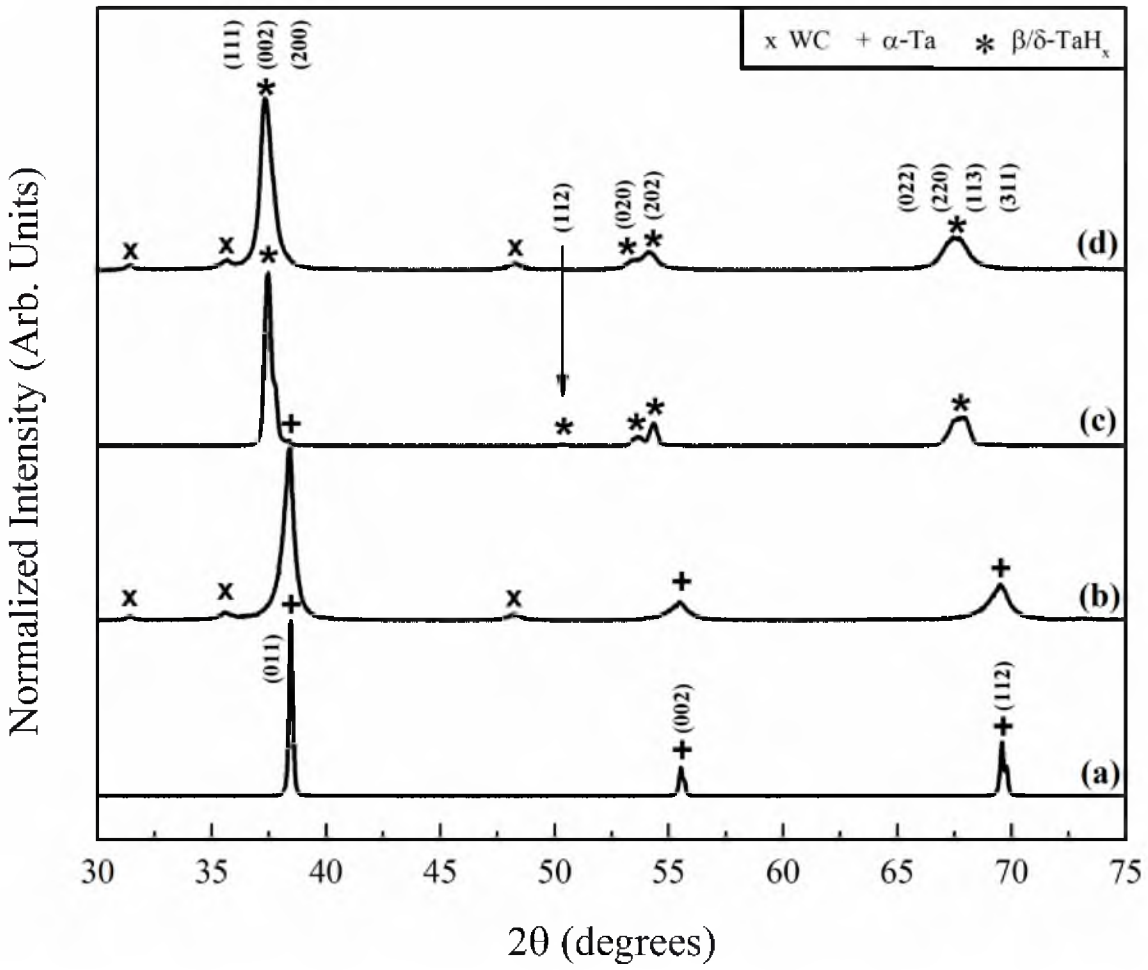

Figure 3.4 XRD patterns of (a) as-received Ta powder, (b) untreated Ta powder milled with 1:50 weight ratio of the powder and the media, (c) H_2-treated, unmilled Ta powder, and (d) H_2-treated Ta powder milled with 1:50 weight ratio.

powder. All three groups showed peak splitting which was especially evident for the peaks at $2\theta = 54^{o}$ and 68^{o}. In addition to the three primary peak groups, minor peaks with relative intensities < 1 % formed at approximately 42.5^{o}, 50.4^{o}, 57.8^{o}, and 71.1^{o}. The peak shifts, peak splitting and the formation of minor peaks are indicative of the formation of an orthorhombic phase, where the H atoms are ordered in specific tetrahedral sites of the unit cell [43]. The diffraction pattern was identified as that of 100 w% orthorhombic β-TaH_X phase with the lattice parameters, A = 4.760 Å, B = 3.418 Å, and C = 4.788 Å. The diffraction pattern of the H_2-treated and milled Ta powder, Figure 3.5(d), showed both additional broadening of the peaks due to deformation and the presence of minor peaks associated with the δ-WC phase (~6.4 w%). The minor peaks associated with the orthorhombic phase were no longer evident, likely as a result of broadening beyond the detection ability of the XRD.

TaH_X phases are often identified as monoclinic since the minor orthorhombic lattice peaks are difficult to detect using XRD [43, 44]. Additionally, since γ, the axial angle for the monoclinic unit cell of TaH_X, is close to 90^{o}, the phase can be successfully characterized using the tetragonal crystal structure [46]. The orthorhombic phase is a superstructure of the monoclinic phase and both describe the same crystal structure as explained by Asano et al. [42, 43]. The monoclinic lattice parameters can be calculated from the orthorhombic lattice parameters using the following transformations [42, 43]:

$$\gamma = \cos^{-1}\left[\frac{\left(\frac{A}{C}\right)^2 - 1}{1+\left(\frac{A}{C}\right)^2}\right] \qquad (3.1)$$

$$a = b = \frac{A}{\left[2(1+\cos\gamma)\right]^{1/2}} \tag{3.2}$$

$$c = B \tag{3.3}$$

In Equations (3.1 to 3.3), *a, b* and *c* are the lattice parameters of the monoclinic lattice. Rietveld refinement of the H_2-treated Ta powder favored the orthorhombic structure over the tetragonal structure, likely as a result of being able to match up the minor orthorhombic peaks which do not exist for the tetragonal structure. San-Martin and Manchester [44] have reported lattice parameters for β-TaH_x using the monoclinic unit cell as a function of the hydrogen concentration, x. The lattice parameters measured for the H_2-treated Ta powder correspond to a hydrogen atomic concentration of approximately 37 atomic %, or a nominal composition of β-$TaH_{0.59}$. This composition is close to β-$TaH_{0.56}$, the phase boundary of the β phase at 25°C [44].

Figure 3.5 shows the X-ray diffraction patterns of the as-received and the H_2-treated Ta sheet specimens. The diffraction pattern for the as-received Ta sheet specimen, Figure 3.5(a), showed the three peaks corresponding to the (011), (002) and (112) lattice planes of the bcc α-Ta metal just like the as-received Ta powder with a lattice parameter of 3.307 Å. The Ta sheet specimen H_2-treated without the catalyst, Figure 3.5(b), did not show signs of peak splitting as seen in the H_2-treated Ta powder samples, but did show slight shifts to smaller 2θ angles indicating an isotropic lattice expansion. The lattice parameter of the bcc unit cell increased to 3.326 Å, indicating that approximately 9

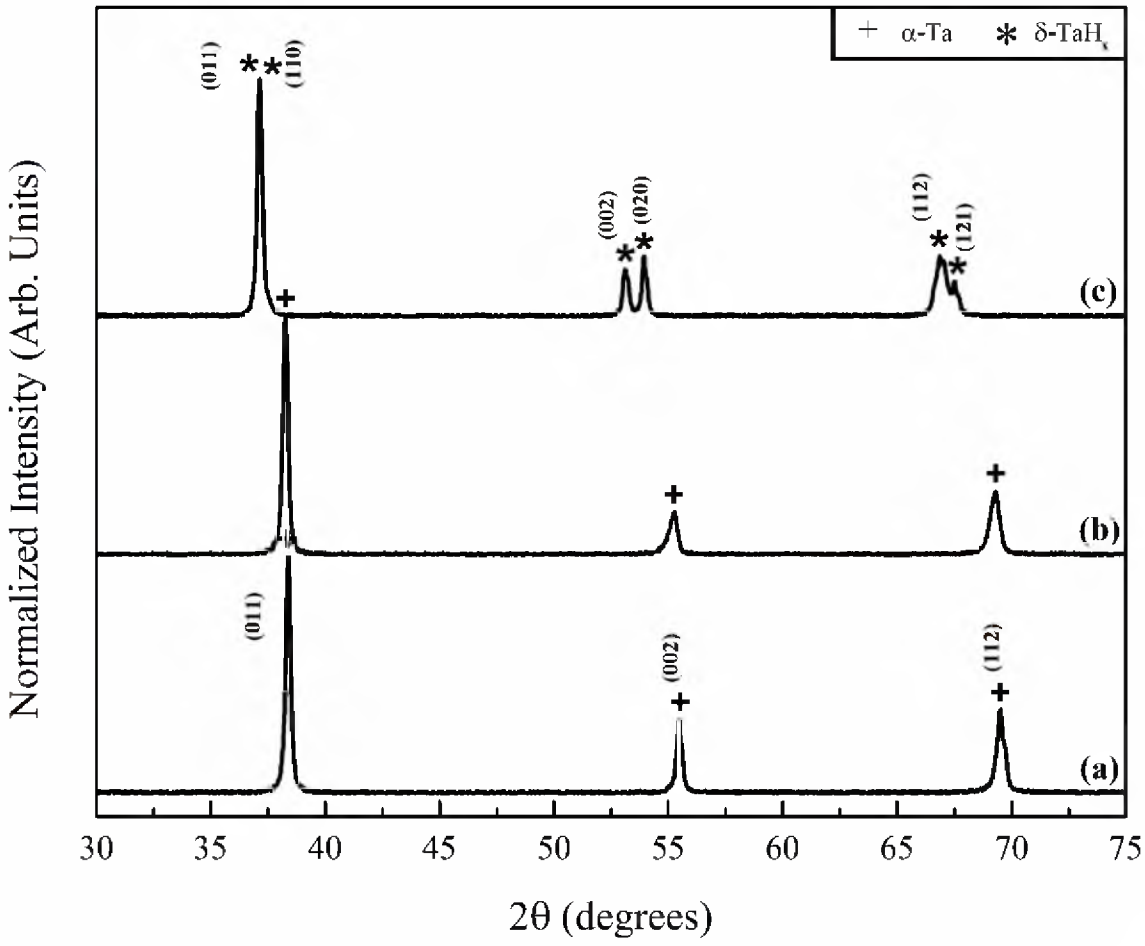

Figure 3.5 XRD patterns of (a) as-received Ta sheet, (b) Ta sheet H_2-treated without the catalyst, and (c) Ta sheet H_2-treated with $Pd(NO_3)_2$ catalyst.

atomic % H was dissolved in the cubic lattice [44, 74]. The Ta sheet specimen H_2-treated with the catalyst (Figure 3.5(c)) had both peak splitting and a significant shift to smaller 2θ angles. There was no evidence of the formation of minor orthorhombic peaks such as those seen in the H_2-treated Ta powder sample. Instead, the Ta sheet specimen H_2-treated with the catalyst was identified as the monoclinic (pseudo-tetragonal) δ-TaH_X phase. [40, 44, 46]. Rietveld refinement using the tetragonal crystal structure determined $a = b =$ 3.397 Å, and c = 3.442 Å, which corresponds to a hydrogen atomic concentration of approximately 42 %, or a composition of δ-$TaH_{0.72}$ in the single-phase δ-TaH_X region of the phase diagram [44]. The higher concentration of H in the Ta sheet specimen treated with the catalyst relative to the uncatalyzed powder could be attributed to two possible reasons: (a) The Ta sheet specimen was polished prior to the H_2-treatment, which could have removed any protective oxide layer improving H adsorption and diffusion; (b) the concentration of the catalyst on the surface of the Ta sheet was likely higher than the average concentration of catalyst on the Ta powder resulting in faster H adsorption.

An X-ray diffraction measurement was also made on the catalyst-free surface of the Ta sheet specimen treated with the catalyst and showed full conversion to the δ-TaH_X phase with near identical lattice parameters. The formation of δ-TaH_X on the non-catalyzed side of the catalyzed Ta sheet specimen can be explained by the high H diffusion rate constant of 3.24 x 10^{-5} cm^2/s at 350°C [75] and the fast catalyst-aided H adsorption [48].

Table 3.2 lists the w% of the WC contamination for the four conditions of milling as determined by Rietveld refinement of the powder x-ray diffraction patterns. Contamination increased with increasing ball-to-charge ratio and was greater for the as-

Table 3.2 Weight % of WC in Ta powders for the four conditions of milling as estimated by Rietveld refinement.

Powder to Media Weight Ratio	w% WC	
	Untreated	H_2-Treated
Unmilled	0	0
1:10	0.8	0.8
1:25	4.7	3.4
1:50	11	6.4

received Ta powder than the H_2-treated Ta powder. Milling media was weighed before and after milling and changed less than 0.1 % (< 0.2 g) for all samples. The WC contamination was likely due to the wear of the WC container.

3.4 Embrittlement of Hydrogenated Ta Metal

Figure 3.6 plots Vickers hardness of untreated and H_2-treated Ta sheet specimens as functions of indentation load. At 4.9 N load, the Vickers hardness of Ta sheet specimens of (a) untreated, (b) H_2-treated without the Pd catalyst, and (c) H_2-treated with the Pd catalyst were 0.9 GPa, 1.0 GPa and 1.9 GPa, respectivey. Though there was limited hardening of the catalyst-free sheet specimen relative to the untreated sheet specimen at 4.9 N load, there was significant hardening at low indentation loads. Thus, for example, at an indentation load of 0.49 N, the hardness of the Ta sheet H_2-treated without the catalyst was 1.9 GPa, while that of the untreated specimen was 1.1 GPa. This suggests that the near surface of the catalyst-free Ta sheet was harder than the bulk when compared to the untreated Ta sheet, possibly as a result of strain from interstitial H in the bcc Ta lattice, which can be as high as 0.8 % [46]. Though no morphological changes were observed on the surfaces of the H_2-treated Ta sheet surfaces, as has often been reported in hydrogenation studies of single and polycrystalline metals [46], SEM images of microhardness indentations showed microcracks (Figure 3.7). Indentations on the as-received Ta sheet specimen, Figure 3.7(a), did not result in any crack formation at the maximum load applied (4.9 N). Short cracks parallel to the square edges of the Vickers impressions were noted on Ta sheet specimen H_2-treated without the catalyst (Figure 3.7(b)). Ta sheet specimen H_2-treated with the catalyst showed long radial cracks along

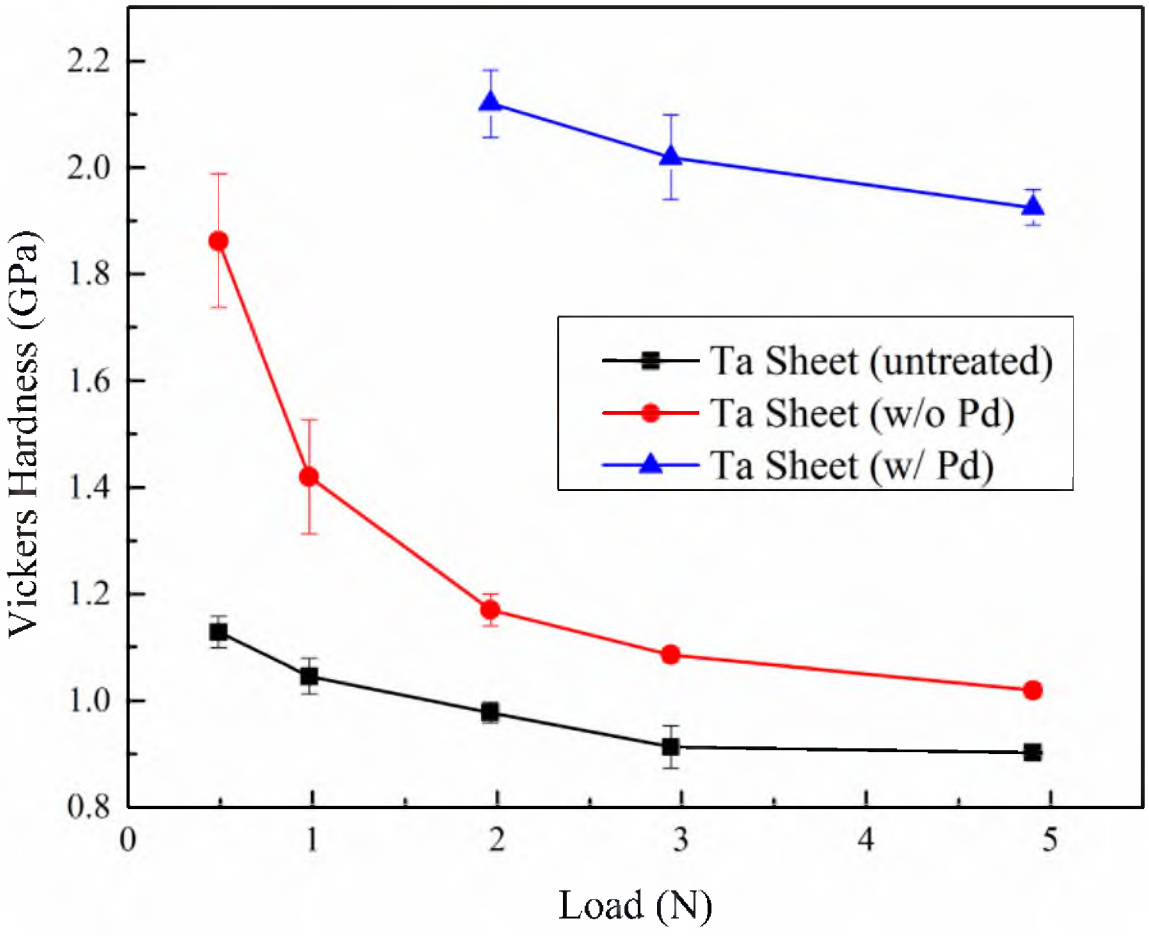

Figure 3.6 Vicker's hardness values for as-received and H_2-treated Ta sheet specimens as functions of indentation load.

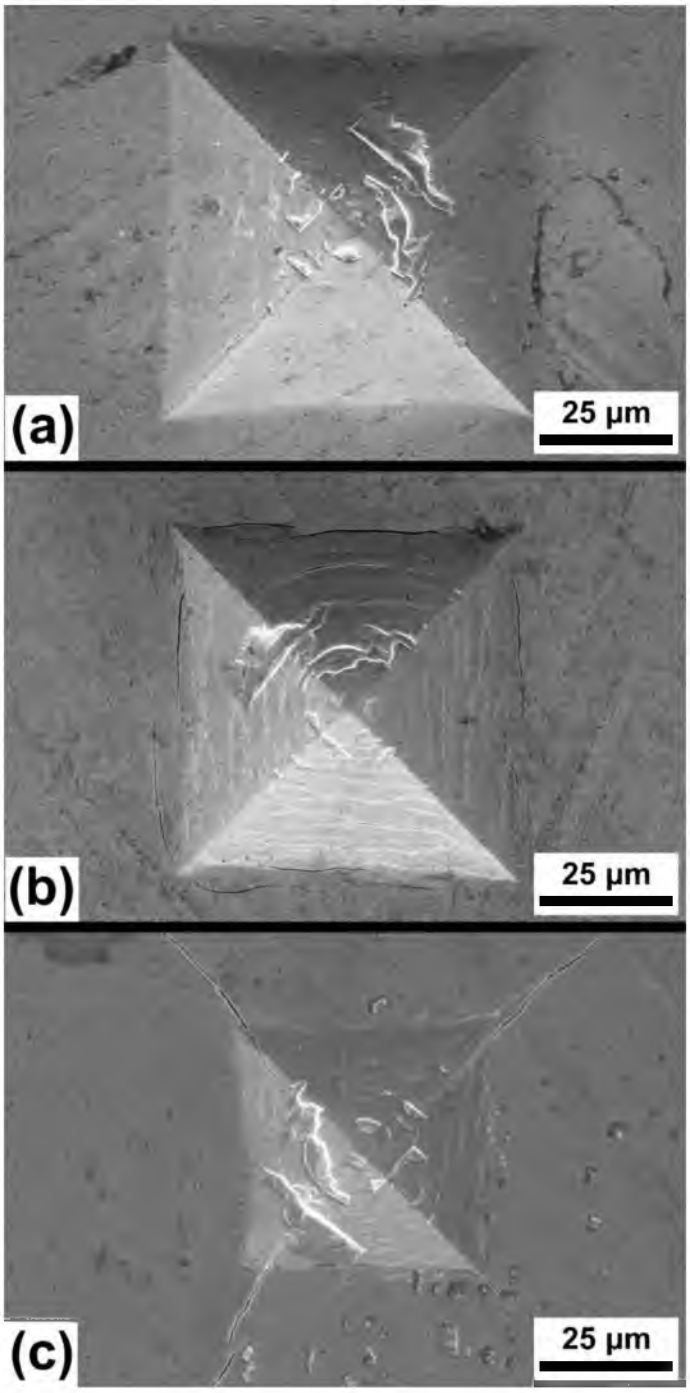

Figure 3.7 SEM images of the Vickers hardness impressions of (a) 4.9 N Vickers indent on as-received Ta sheet specimen, (b) 4.9 N Vickers indent on Ta sheet specimen H_2-treated without the catalyst, and (c) 4.9 N Vickers indent on Ta sheet specimen H_2-treated with the catalyst.

the diagonals of the Vickers impression (Figure 3.7(c)). This is a confirmation of the embrittlement and decrease of the fracture toughness of the TaH_x phase relative to the Ta metal, which is the main reason for the efficient comminution of hydrogenated Ta.

CHAPTER 4

PROCESSING OF DENSE ζ-Ta_4C_{3-x} BY PRESSURELESS SINTERING OF Ta AND TaC POWDERS MIXTURE

4.1 Introduction

This chapter reports the results of a study of the kinetics of formation of ζ-Ta_4C_{3-x} from Ta and γ-TaC powders during pressureless sintering. The results showed a four-stage process consisting of (a) decomposition of β-TaH_x above 300-350°C, (b) the conversion of the Ta metal to α-Ta_2C_y, and a concurrent depletion of C in γ-TaC_y at temperatures ranging from 900 to 1200°C, (c) equilibration of α-Ta_2C and γ-$TaC_{0.78}$ phases at temperatures between 1200°C and 1500°C, and (d) the conversion of the α-Ta_2C and the γ-$TaC_{0.78}$ phases to ζ-Ta_4C_{3-x} at temperatures above 1500°C. The analyses of the kinetics revealed a low activation energy for the formation of the α-Ta_2C_y, phase in the second stage, while a high activation energy characterized the formation of the ζ-Ta_4C_{3-x} phase. The kinetics of formation of the ζ-Ta_4C_{3-x} phase was enhanced by hydrogenation of the Ta powder, which increased its sinterability by reducing particle size. This processing innovation enabled the compacts to be pressureless sintered to greater than 94% of theoretical density. However, the maximum ζ-Ta_4C_{3-x} content was limited to 86 w% with the balance consisting of γ-TaC_y and a trace amount of a Ta oxide phase.

4.2 TaC0.66 Powder Characteristics

The specific surface areas of the as-received Ta and γ-TaC powders were 0.14 m^2/g and 0.93 m^2/g, respectively. The specific surface areas of the milled $TaC0.66^a$, $TaC0.66^b$ and $TaC0.66^c$ powder samples were 0.85 m^2/g, 0.89 m^2/g and 1.21 m^2/g, respectively. The particle-size distributions of the three powders are shown in Figure 4.1. The $TaC0.66^a$ powder showed a bimodal distribution with modes at 1.8 μm and 27 μm. The primary distribution with the 1.8 μm mode is likely that of γ-TaC, which is the smaller and the harder phase. The secondary distribution with the 27 μm mode is broad with particle sizes ranging from 10 to 60 μm, likely a result of the deformation, flattening and agglomeration of the Ta particles. The $TaC0.66^b$ powder showed one major distribution with a mode of 2.4 μm and a minor distribution with a mode of 11 μm. The primary distribution was broad and likely consisted of γ-TaC and smaller H_2-treated Ta particles. The secondary distribution likely contained larger H_2-treated Ta agglomerates between 5 μm and 20 μm in size. The $TaC0.66^c$ powder showed a bimodal distribution with modes at 1.8 μm and 14 μm. Both distributions were broad and contained approximately equal volume of particles. The secondary distribution with the 14 μm mode contained particles up to 60 μm in size. SEM images of the milled powders are shown in Figure 4.2. The $TaC0.66^a$ powder (Figure 4.2(a)) showed particles with two distinct morphologies. Smaller particles under 5 μm in size were distributed among flat, highly deformed plate-like agglomerated particles ranging in size upwards of 60 μm. Figure 4.2(b) shows the SEM image of the milled $TaC0.66^b$ powder. The powder contained equiaxed particles with a significant number under 1 μm and few particles larger than 5 μm. The particles did not appear deformed or plate-like. Figure 4.2(c) shows

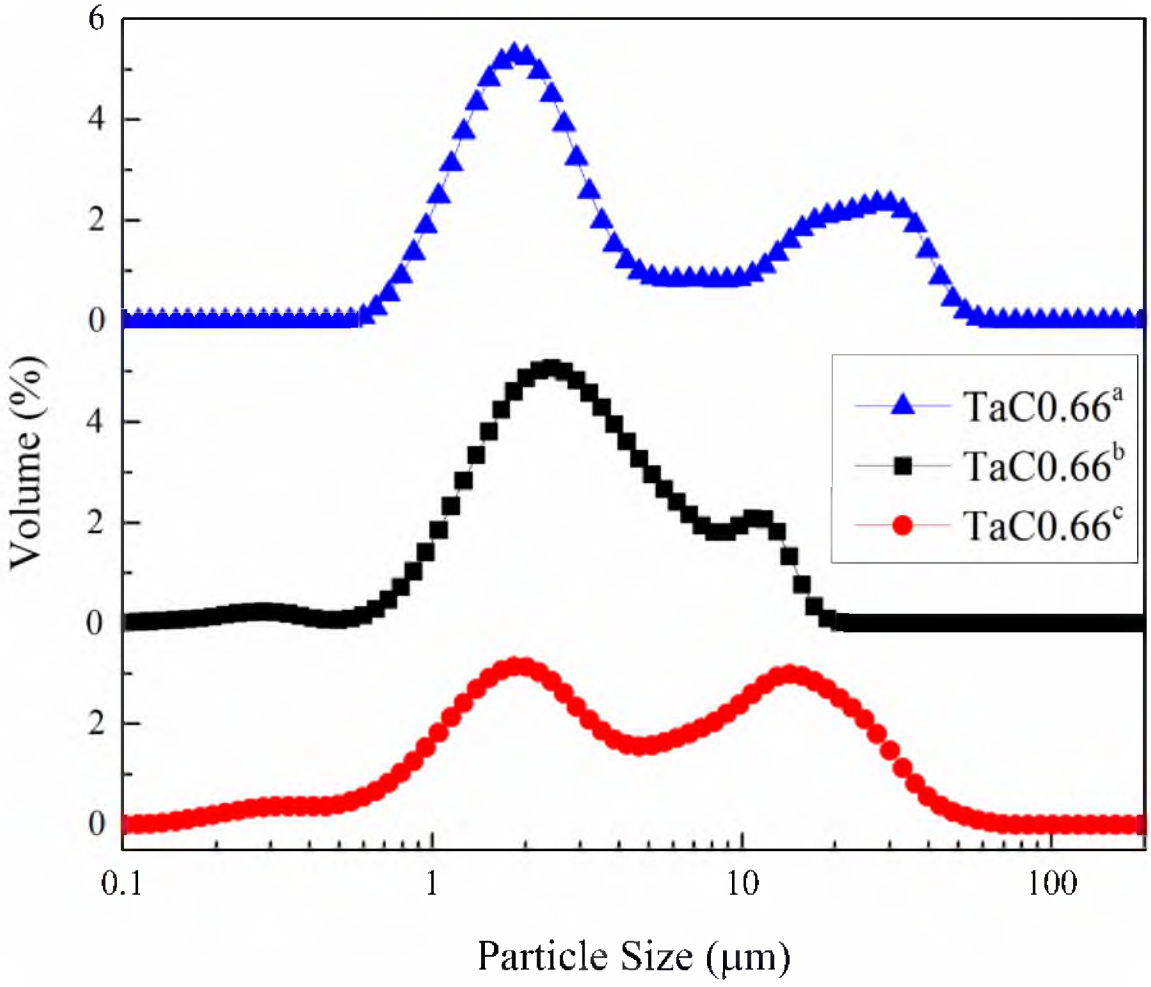

Figure 4.1 Particle size distributions of milled $TaC_{0.66}^{a}$, $TaC_{0.66}^{b}$ and $TaC_{0.66}^{c}$ powders.

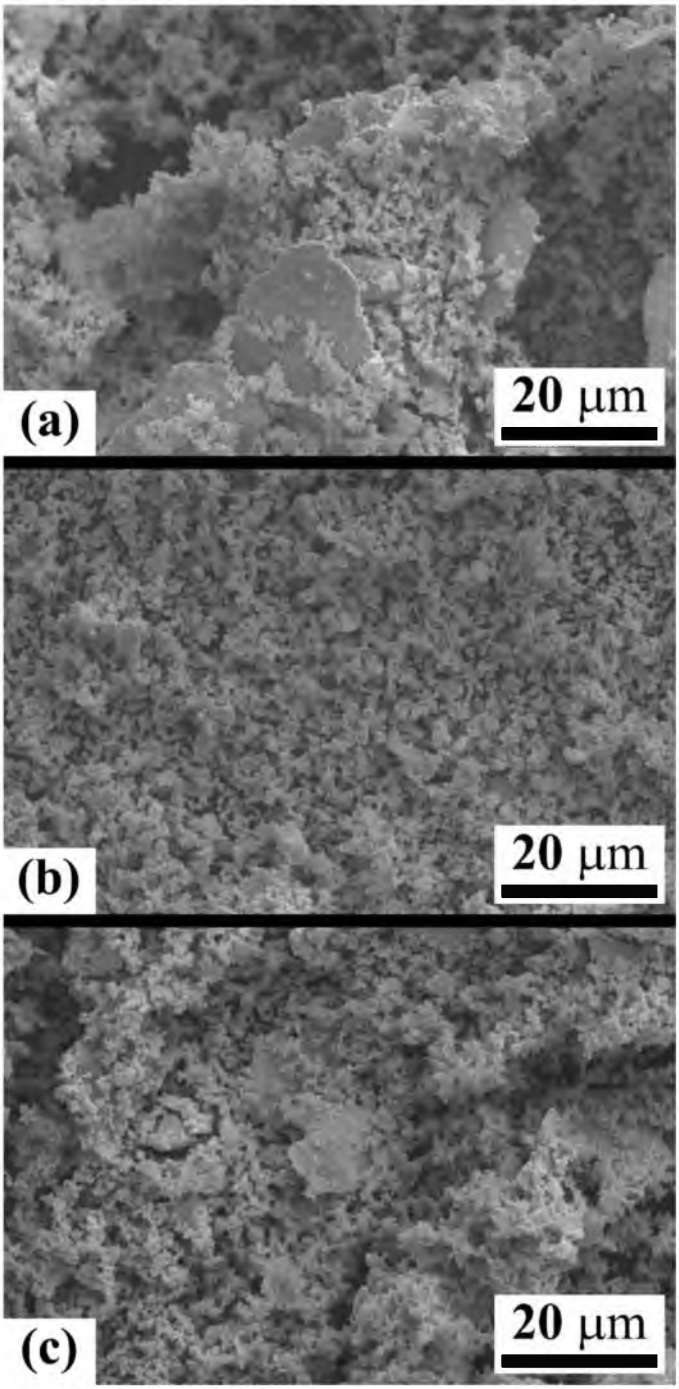

Figure 4.2 SEM images of milled (a) $TaC_{0.66}$[a], (b) $TaC_{0.66}$[b], and (c) $TaC_{0.66}$[c] powders.

the SEM image of the milled $TaC_{0.66}^{c}$ powder. The powder contains two distinct morphologies. Smaller equiaxed particles under 5 μm in size were distributed among larger agglomerated particles ranging in size upwards of 30 μm.

4.3 Densification and Phase Evolution in TaC0.66 Pellets During Sintering

Figure 4.3 shows plots of densities, expressed as percent of theoretical densities, measured on the $TaC_{0.66}^{a}$ and $TaC_{0.66}^{b}$ pellets as functions of time during sintering at different temperatures. The theoretical densities used to normalize the measured densities were based on the phase contents as measured by the Rietveld refinement technique and the theoretical densities of the various phases present in the sintered pellets. The pellets of the $TaC_{0.66}^{a}$ powder reached a maximum density of 66 % of theoretical density after sintering at 1800°C for 60000 s. However, the same powder could be hot-pressed and HIPed to a density of 99.1 % of theoretical density at 1800°C and 7200 s. The pellets of the H_2-treated and milled powder, $TaC_{0.66}^{b}$, reached a density of 94.8 % of theoretical density, when sintered at 1800°C for 60000 s. All $TaC_{0.66}^{b}$ pellets sintered at 1700°C for more than 6000 s attained greater than 93% of theoretical density. The pellets of the planetary milled powder, $TaC_{0.66}^{c}$, reached a density of 91.1 % of theoretical density, when sintered at 1800°C for 30000 s.

The lack of densification in the $TaC_{0.66}^{a}$ pellets had a detrimental effect on the formation of the ζ-Ta_4C_{3-x} phase. Figure 4.4 shows the X-ray diffraction patterns of the starting powder and of the partially-sintered pellets of $TaC_{0.66}^{a}$. The starting powder (Figure 4.4(a)) contained the bcc Ta and the fcc γ-TaC_y phases. Figures 4.4(b) and 4.4(c)

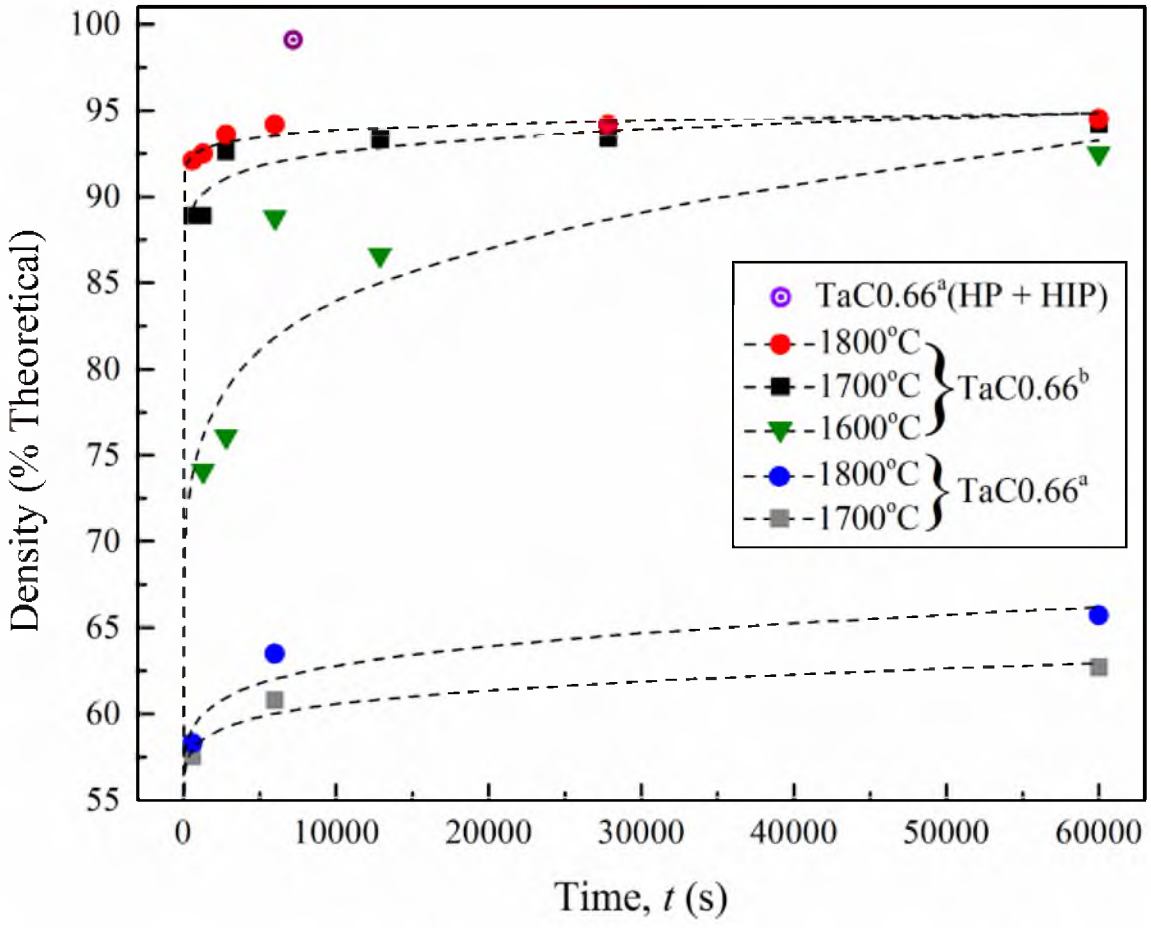

Figure 4.3 Increase in densities of $TaC_{0.66}^{a}$ and $TaC_{0.66}^{b}$ pellets as functions of time during sintering at different temperatures.

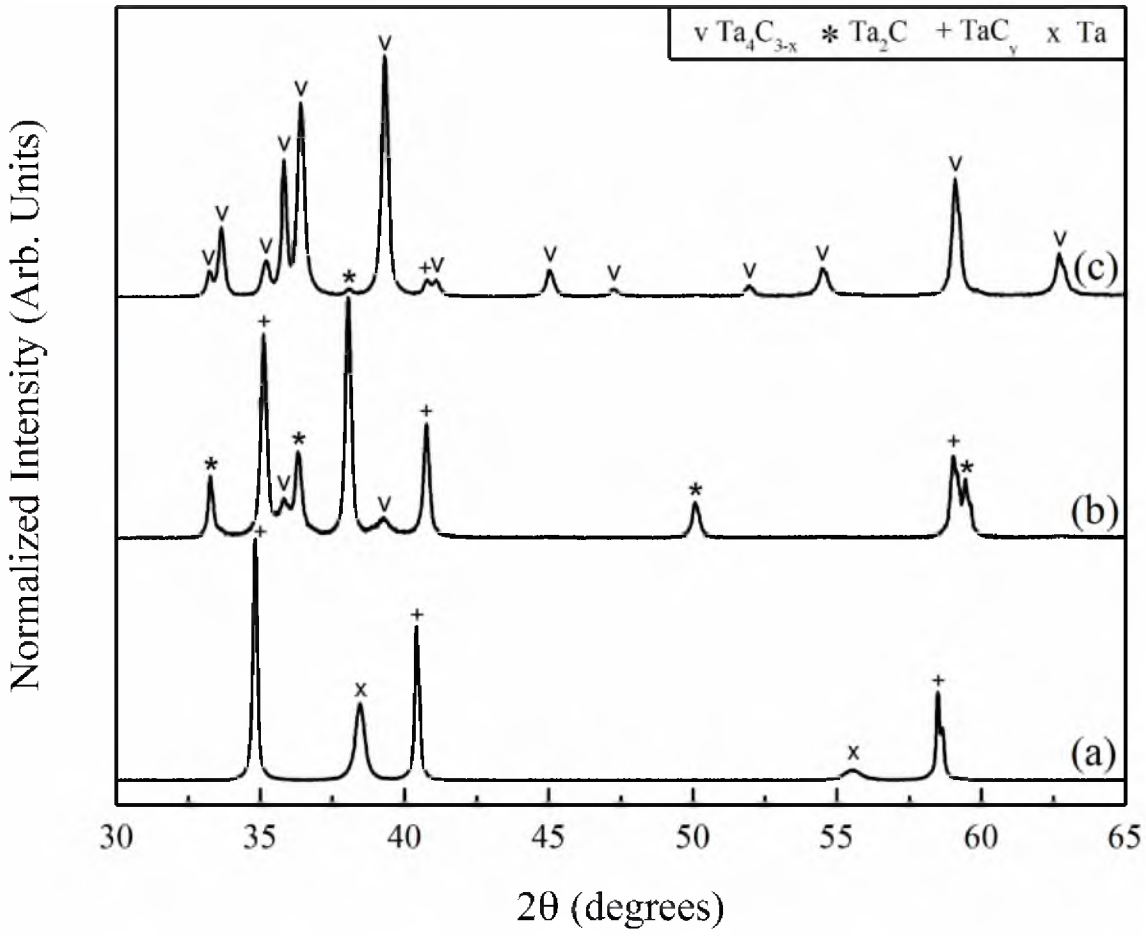

Figure 4.4 X-ray diffraction patterns of (a) as-prepared TaC0.66[a] powder, (b) a pellet of TaC0.66[a] partially-sintered at 1800°C and 60000 s and (c) a hot-pressed and HIPed billet of TaC0.66[a](HP+HIP).

show the XRD patterns of a pellet sintered at 1800°C for 60000 s and the hot-pressed and HIPed billet, respectively. The amount of the ζ-Ta_4C_{3-x} phase formed during pressureless sintering, as determined by Rietveld analysis of the XRD patterns, never exceeded approximately 0.23 weight fraction with the balance being α-Ta_2C_y, and γ-TaC_y where y = 0.78, as indicated by the change in the lattice parameter [56]. The hot-pressed and HIPed billet contained approximately 0.95 weight fraction ζ-Ta_4C_{3-x} phase with the balance made up of the α-Ta_2C_y, and γ-TaC_y phases. There was no indication of peaks associated with the WC phase; however, there were two minor peaks (I/Imax < 1%) at approximately 23° and 28° 2θ which could represent the Ta_2O_5 phase, but were too weak to be identified as any one specific Ta oxide phase.

Figure 4.5 shows the X-ray diffraction patterns of the $TaC0.66^b$ powder and of the partially-sintered pellets. The starting powder (Figure 4.5(a)) contained the orthorhombic β-TaH_x and the fcc γ-TaC_y phases. Figures 4.5(b) through 4.5(e) show X-ray diffraction patterns of pellets sintered at 1600°C through 1900°C for 6000 s. Approximately, 0.11-0.13 weight fraction ζ-Ta_4C_{3-x} phase formed at 1600°C in 6000 s. The formation of the ζ-Ta_4C_{3-x} phase was strongly influenced by temperature. The amount of the ζ-Ta_4C_{3-x} phase formed in 6000 s increased to 0.75 weight fraction at 1700°C, and between 0.83 and 0.86 weight fraction at 1800°C and 1900°C. The amount of the ζ-Ta_4C_{3-x} phase never exceeded approximately 0.86 weight fraction at any temperature or time with the balance being γ-TaC_y with a C/Ta ratio of y = 0.78, as indicated by the lattice parameter shift.

Figure 4.6 shows the X-ray diifraction patterns of the $TaC0.66^c$ powder and of the partially sintered pellets. The starting powder (Figure 4.6(a)) contained the bcc Ta and the fcc γ-TaC_y phases. The peaks corresponding to the Ta phase were broad relative to

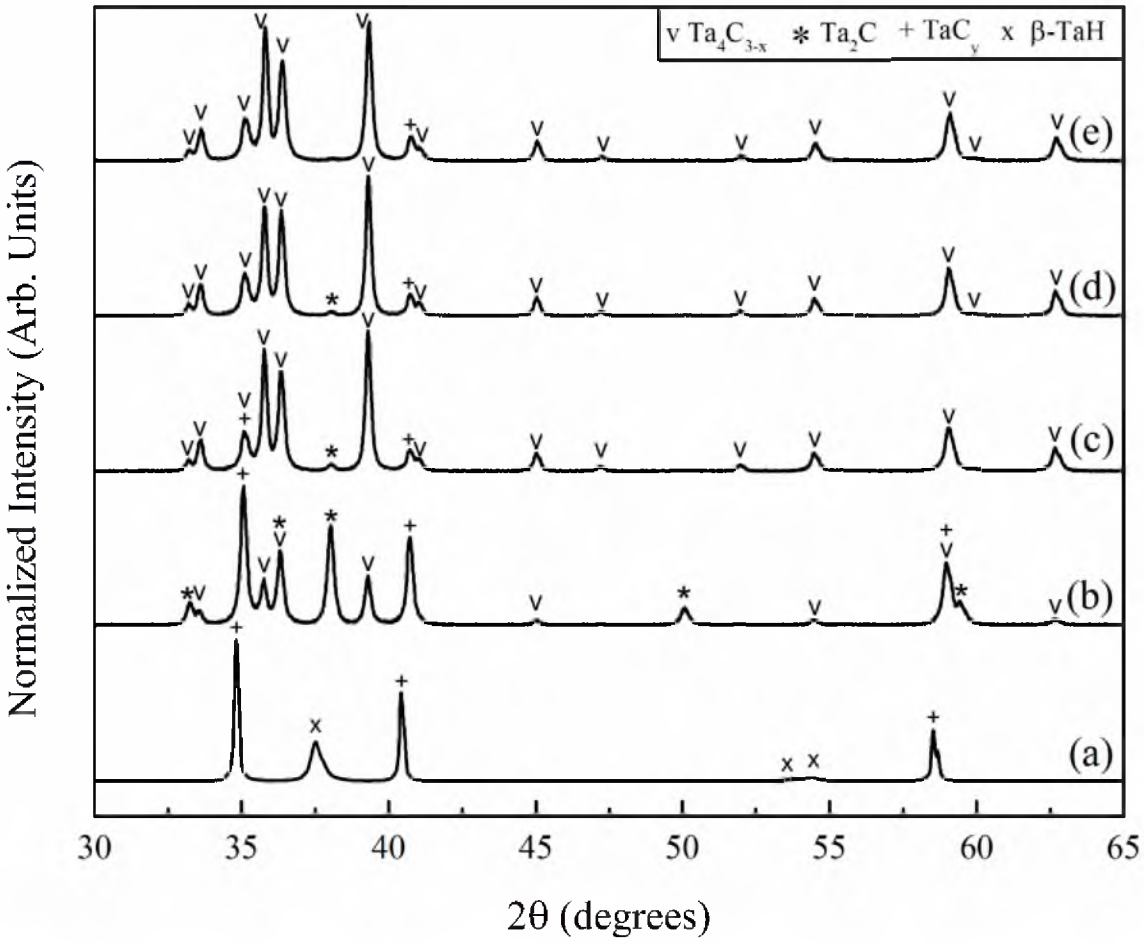

Figure 4.5 X-ray diffraction patterns of (a) as-prepared TaC0.66[b] powder, and pellets sintered for 6000 s at temperatures of (b) 1600°C, (c) 1700°C, (d) 1800°C, (e) 1900°C.

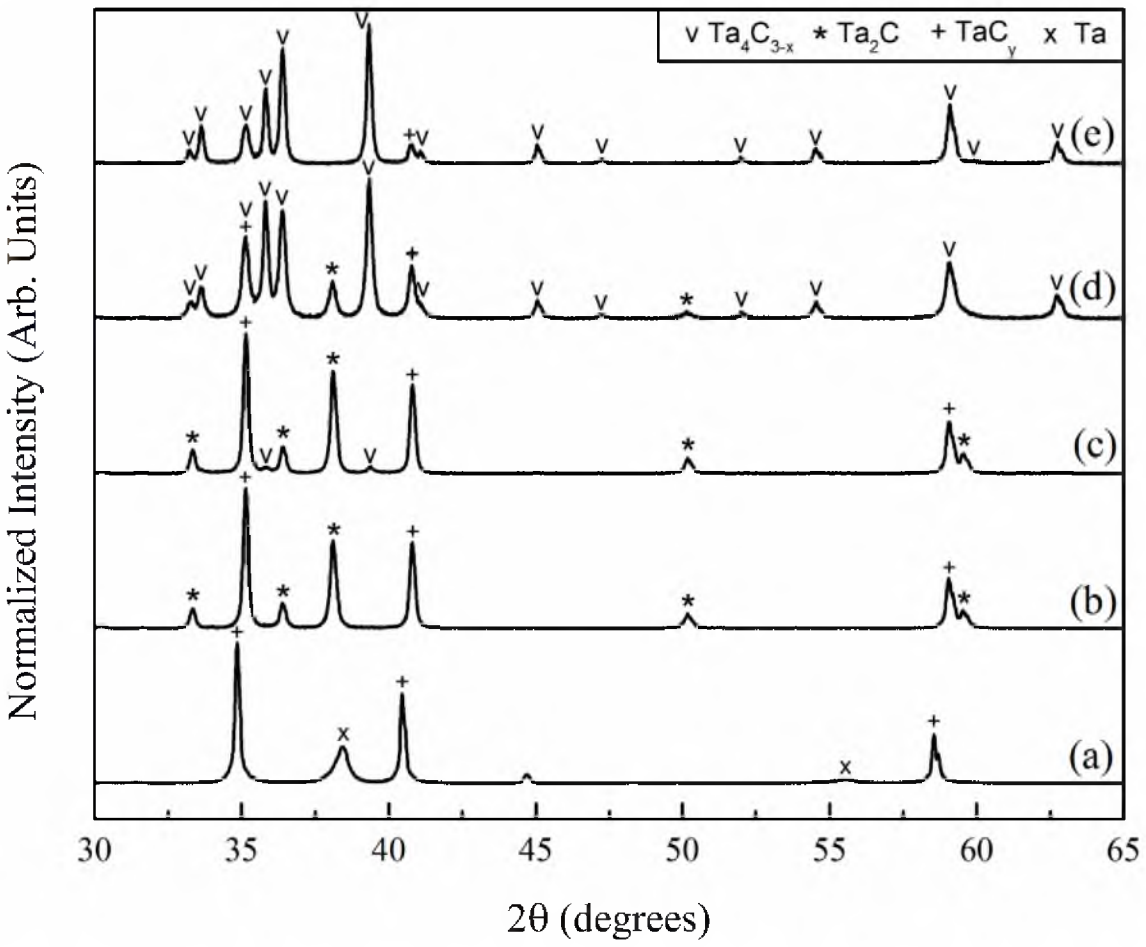

Figure 4.6 X-ray diffraction patterns of (a) as-prepared TaC0.66[c] powder, and pellets sintered for 6000 s at temperatures of (b) 1675°C, (c) 1700°C, (d) 1730°C, (e) 1800°C.

the TaC0.66[a] powder, likely as a result of induced strain and stress from the high energy planetary milling. Figures 4.6(b) through 4.6(e) show X-ray diffraction patterns of pellets sintered at 1675°C through 1800°C for 6000 s. Approximately, 0.07 weight fraction ζ-Ta_4C_{3-x} phase formed at 1700°C in 6000 s. The formation of the ζ-Ta_4C_{3-x} phase was strongly influenced by temperature. The amount of the ζ-Ta_4C_{3-x} phase formed in 6000 s increased to 0.66 weight fraction at 1730°C, and 0.86 weight fraction at 1800°C. The amount of the ζ-Ta_4C_{3-x} phase never exceeded approximately 0.86 weight fraction at any temperature or time with the balance being γ-TaC_y with a C/Ta ratio of y = 0.78, as indicated by the lattice parameter shift.

4.4 Phase Evolution in TaC0.66[b] Pellets During Sintering

Figure 4.7 shows plots of the weight fraction of the various phases present in the TaC0.66[b] pellets after sintering for 6000 s at temperatures ranging from 900 to 1900°C. Also plotted in Figure 4.7 is y, the C/Ta atomic ratio in the phase, γ-TaC_y obtained from lattice parameter correlation with composition [56]. At temperatures below 900°C, the phase composition of the pellets was essentially the same as that of the starting powder, i.e., 0.66 weight fraction γ-TaC and 0.34 weight fraction β-TaH_x. Beginning at about 900°C, the amount of the Ta phase decreased and the amount of the α-$Ta_2C_{y'}$ phase increased. Concurrently, there was a decrease in y, the C/Ta atomic ratio in γ-TaC_y. This suggested that the Ta metal phase was converted to the α-$Ta_2C_{y'}$ phase by the transport of C from the γ-TaC_y phase. A temporary increase in γ-TaC_y is also observed, and though initially unexpected, is consistent with Hartmann's [76] determination that during the carburization of Ta metal the γ-TaC_y phase nucleates at Ta grain boundaries along with

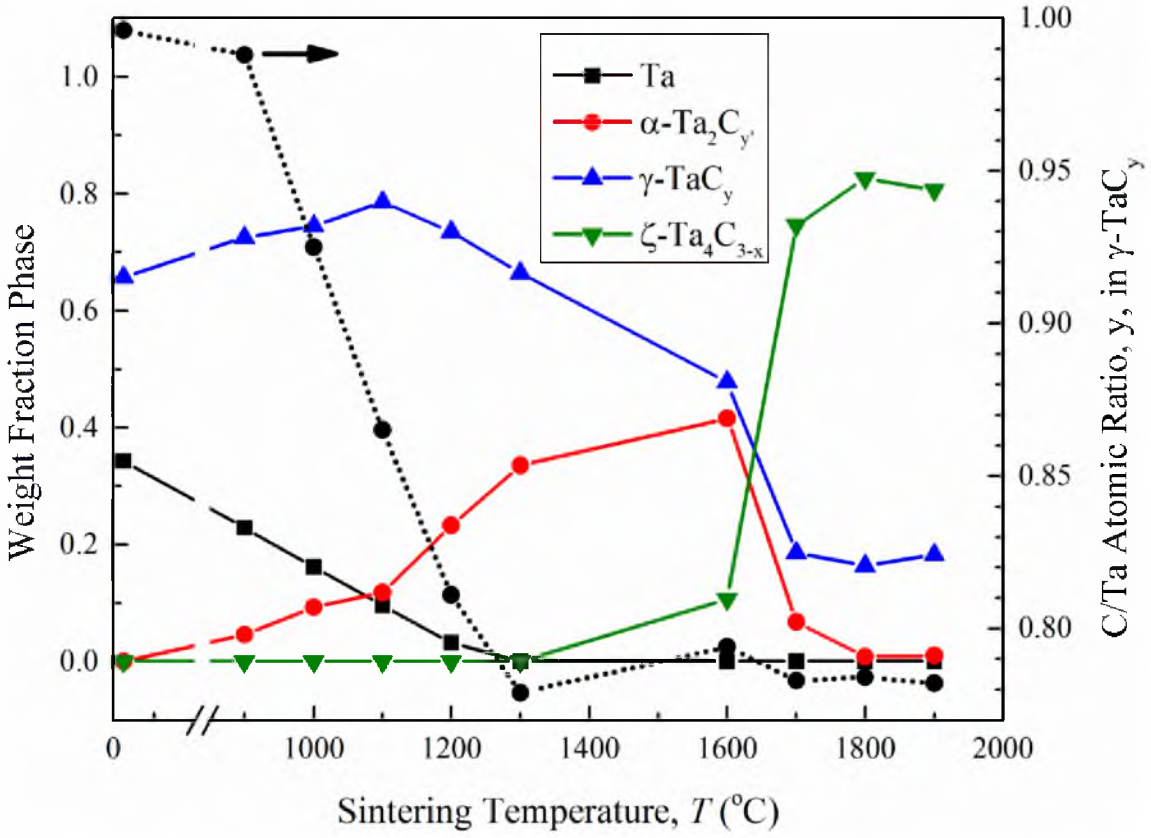

Figure 4.7 Weight fractions of Ta, α-$Ta_2C_{y'}$, γ-TaC_y, and ζ-Ta_4C_{3-x} phases formed in the pellets of $TaC_{0.66}$[b] powder at temperatures between 900°C and 1900°C at hold times of 6000 s.

the α-Ta_2C_y, phase. At approximately 1100°C, there was a rapid increase in α-Ta_2C_y, formation coinciding with a rapid decrease in γ-TaC_y content while Ta continued to decrease. There was no detectable amount of Ta at 1300°C. The C/Ta atomic ratio of γ-TaC_y began to decrease at temperatures above 900°C and reached a minimum level of approximately 0.78 at 1300°C. Of importance to note, at 1300°C, there was approximately 0.34 weight fraction α-Ta_2C_y, and 0.66 weight fraction γ-$TaC_{0.78}$. These are equal to the weight fraction contents of β-TaH_x and γ-TaC in the starting $TaC_{0.66}$[b] powder, signifying that β-TaH_x was directly transformed to α-Ta_2C_y. At 1600°C, the amount of the α-Ta_2C_y, phase increased to 0.42 weight fraction and that of the γ-TaC_y phase decreased to 0.48 weight fraction, and there was evidence for the formation of the rhombohedral ζ-Ta_4C_{3-x} phase (0.11 weight fraction). The formation of the ζ-Ta_4C_{3-x} phase occurred rapidly above 1600°C, with 0.75 weight fraction being formed at 1700°C and reaching approximately 0.86 weight fraction at 1800°C with the balance being γ-TaC_y and a trace amount of the α-Ta_2C_y, phase. The formation of the α-Ta_2C_y, phase and its subsequent equilibration with the γ-TaC_y phase appeared to be a critical step prior to the formation of the ζ-Ta_4C_{3-x} phase at higher temperatures. A detailed kinetics study of the formation of the α-Ta_2C_y, phase at temperatures ranging from 900°C to 1200°C and of the formation of the ζ-Ta_4C_{3-x} phase above 1600°C were conducted.

4.5 Kinetics of Formation of α-Ta_2C_y,

Figure 4.8 shows plots of the weight fractions of α-Ta_2C_y, formed as functions of time at temperatures ranging from 900 to 1200°C. The formation of the α-Ta_2C_y, phase occurred rapidly with about 0.03 weight fraction being formed at 900°C in 600 s. There

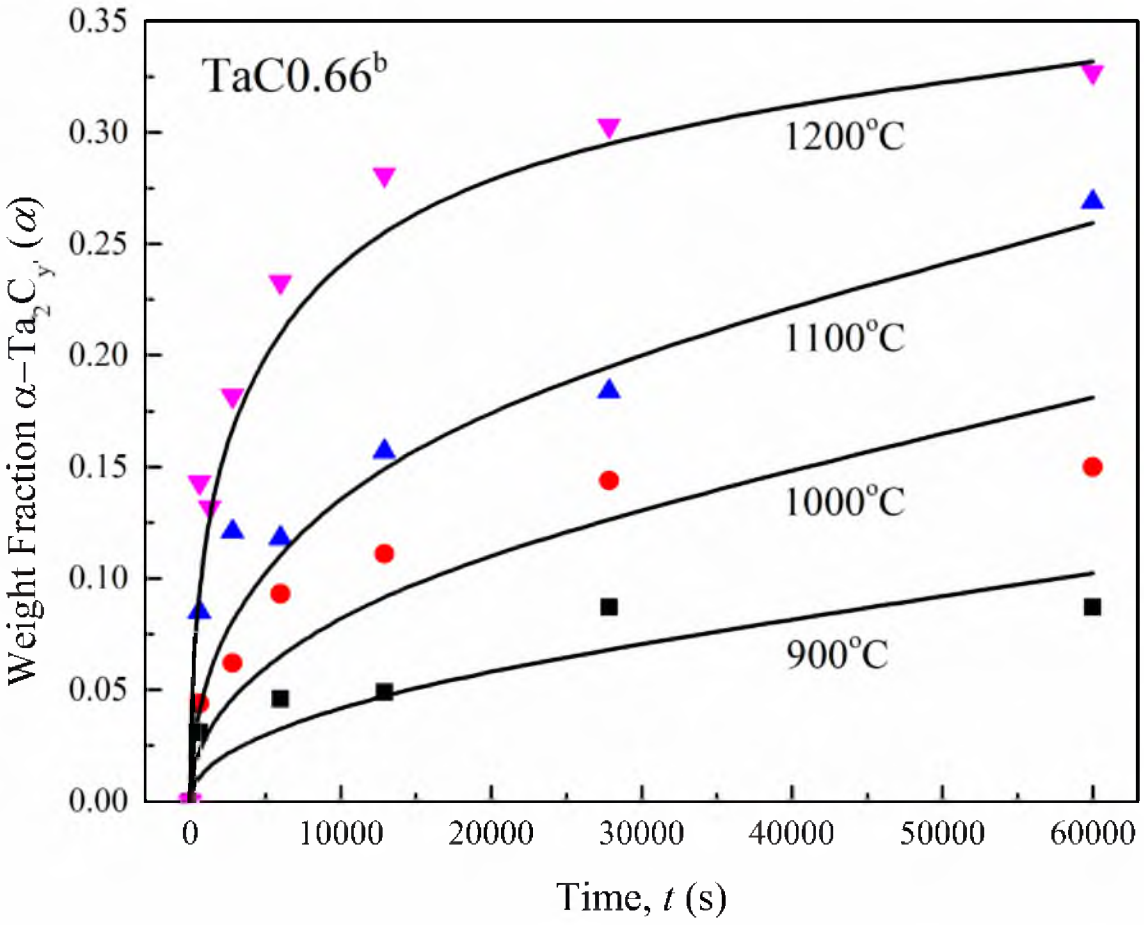

Figure 4.8 Weight fractions of α-Ta_2C_y formed in the TaC0.66[b] pellets as functions of time and temperature.

was no evidence of incubation time even at the lowest temperature investigated, 900°C. The transformation rate decreased monotonically with increasing time and the amount transformed approached a plateau value at 60000 s. Both the transformation rate at a given time and the plateau value of the fraction transformed at 60000 s increased with increasing temperature. Similar trends have been seen in spark plasma sintering [16]. The weight fraction of α-Ta_2C_y formed at 1200°C and 60000 s was 0.33, close to the weight fraction of β-TaH_x in the starting powder.

The weight fraction of α-Ta_2C_y, $\alpha(t,T)$, as a function of time t and temperature, T, could be described by the following form of the Johnson-Mehl-Avrami-Kolmogorov (JMAK) equation [77-80]:

$$\alpha(t,T) = \alpha_\infty \left[1 - \exp\left\{-\sqrt{(kt)}\right\}\right] \tag{4.1}$$

In Eq. (4.1), α_∞ is the maximum weight fraction of α-Ta_2C_y that can be formed from β-TaH_x (0.34 for the TaC0.66[b] powder), and k is a temperature-dependent rate constant. The lines fitted to the data in Figure 4.8 are the "best fits" of Eq. (4.1) with values of the rate constant k estimated at each temperature by nonlinear regression analysis. The temperature dependence of the resulting rate constants was analyzed using the following Arrhenius equation:

$$k = k_o \exp\left(-\frac{Q_1}{RT}\right) \tag{4.2}$$

In Eq. (4.2), k_o is a pre-exponential factor, Q_1 is the activation energy, and R is the gas constant. Figure 4.9 shows a plot of $\log_{10}k$ versus $1/T$. The linear plot confirmed that Eq. (4.2) adequately described the temperature dependence of k. The activation energy Q_1 obtained from the slope was 219 ± 21 kJ/mol.

In order to confirm the kinetics of the formation of the α-Ta_2C_y, phase as functions of time at temperatures ranging from 900 to 1200°C, pellets of the C/Ta = 0.50 composition, processed using the same conditions as the $TaC0.66^b$ pellets, were prepared. As seen in Figure 4.10 the formation of the α-Ta_2C_y, phase occurred rapidly with about 0.04 weight fraction being formed at 900°C in 600 s. As with the $TaC0.66^b$ pellets, there was no evidence of incubation time even at the lowest temperature investigated, 900°C. The weight fraction of α-Ta_2C_y, formed at 1200°C and 60000 s was 0.74. The transformation rate decreased monotonically and was fitted using Eq. (4.1) where α_∞ = 1.0. The temperature dependence of the resulting rate constants are seen in Figure 4.11. The linear plot confirmed that Eq. (4.2) also adequately described the temperature dependence of k in the C/Ta = 0.50 pellets. The activation energy Q_1 obtained from the slope was 222 ± 28 kJ/mol, close to the value for the $TaC0.66^b$ pellets.

4.6 Kinetics of Formation of ζ-Ta_4C_{3-x}

Figure 4.12 shows plots of the weight fraction of the ζ-Ta_4C_{3-x} phase formed during sintering at various temperatures in pellets of both $TaC0.66^a$ and $TaC0.66^b$ powders. In the $TaC0.66^a$ pellets, the formation of ζ-Ta_4C_{3-x} was sluggish with only 0.23 weight fraction being formed at 1800°C in 60000 s. In the $TaC0.66^b$ pellets, on the other hand, ζ-Ta_4C_{3-x} formed rapidly over narrow ranges of both time and temperature. At

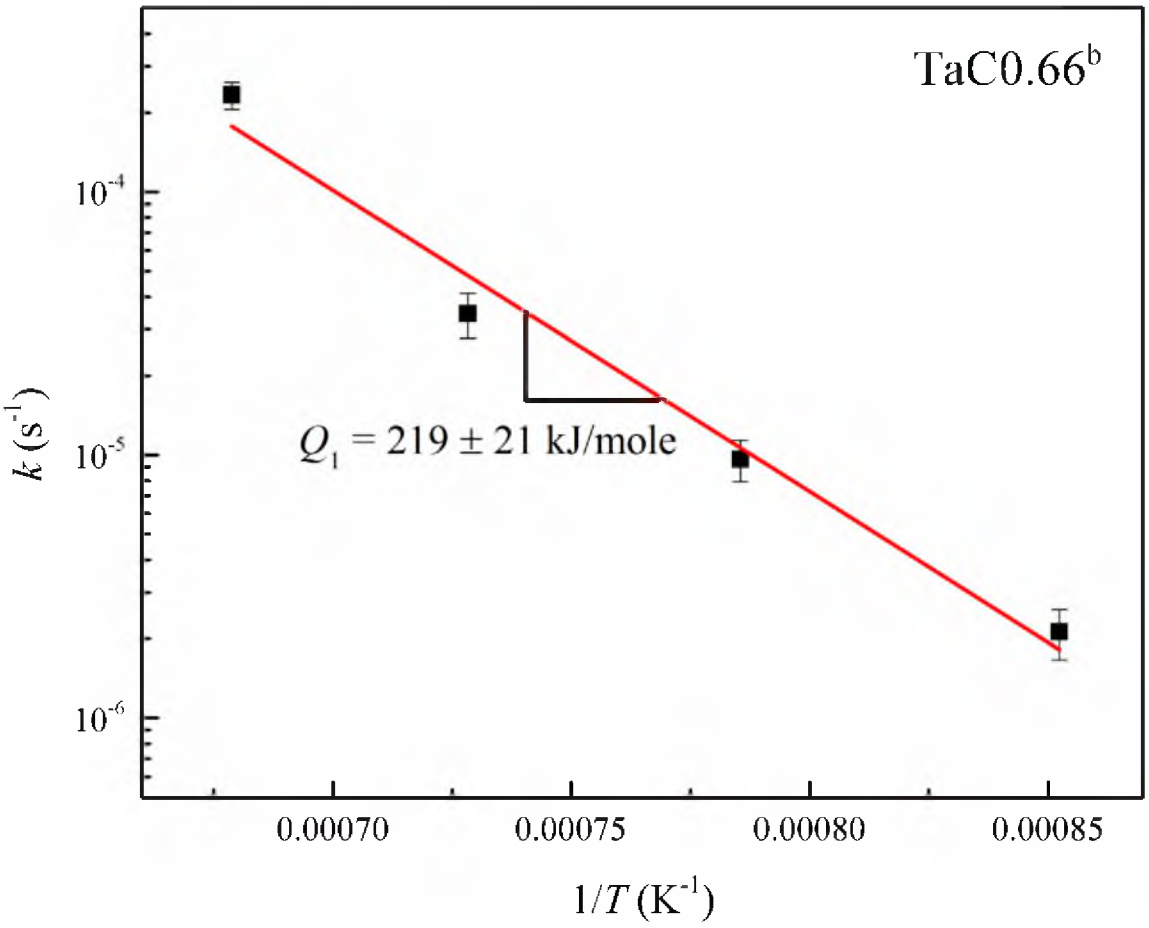

Figure 4.9 Plot of $\log_{10}k$ vs $1/T$ for the kinetics of formation of the α-Ta_2C_y phase.

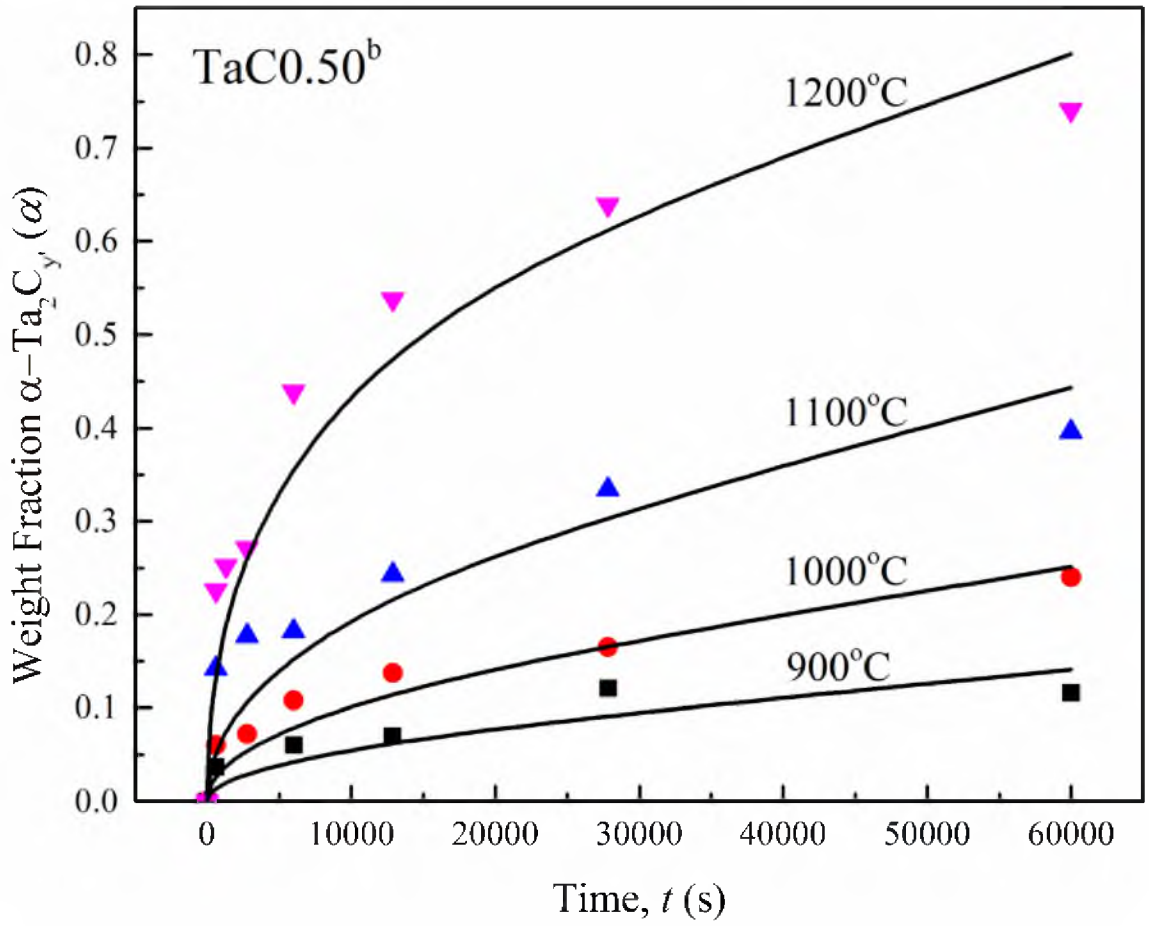

Figure 4.10 Weight fractions of α-$Ta_2C_{y'}$ formed in C/Ta = 0.50 pellets as functions of time and temperature.

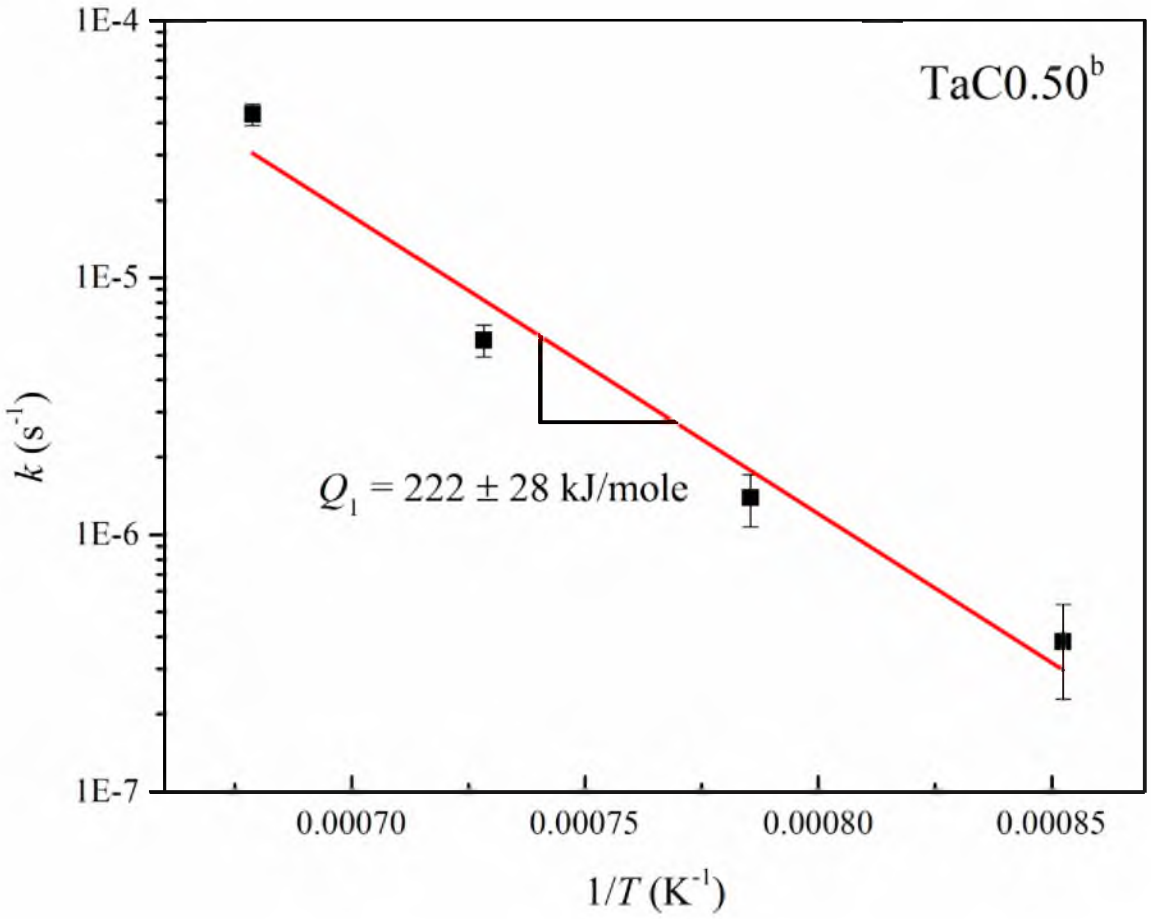

Figure 4.11 Plot of $\log_{10}k$ vs $1/T$ for the kinetics of formation of the α-Ta_2C_y phase for the C/Ta = 0.50 pellets.

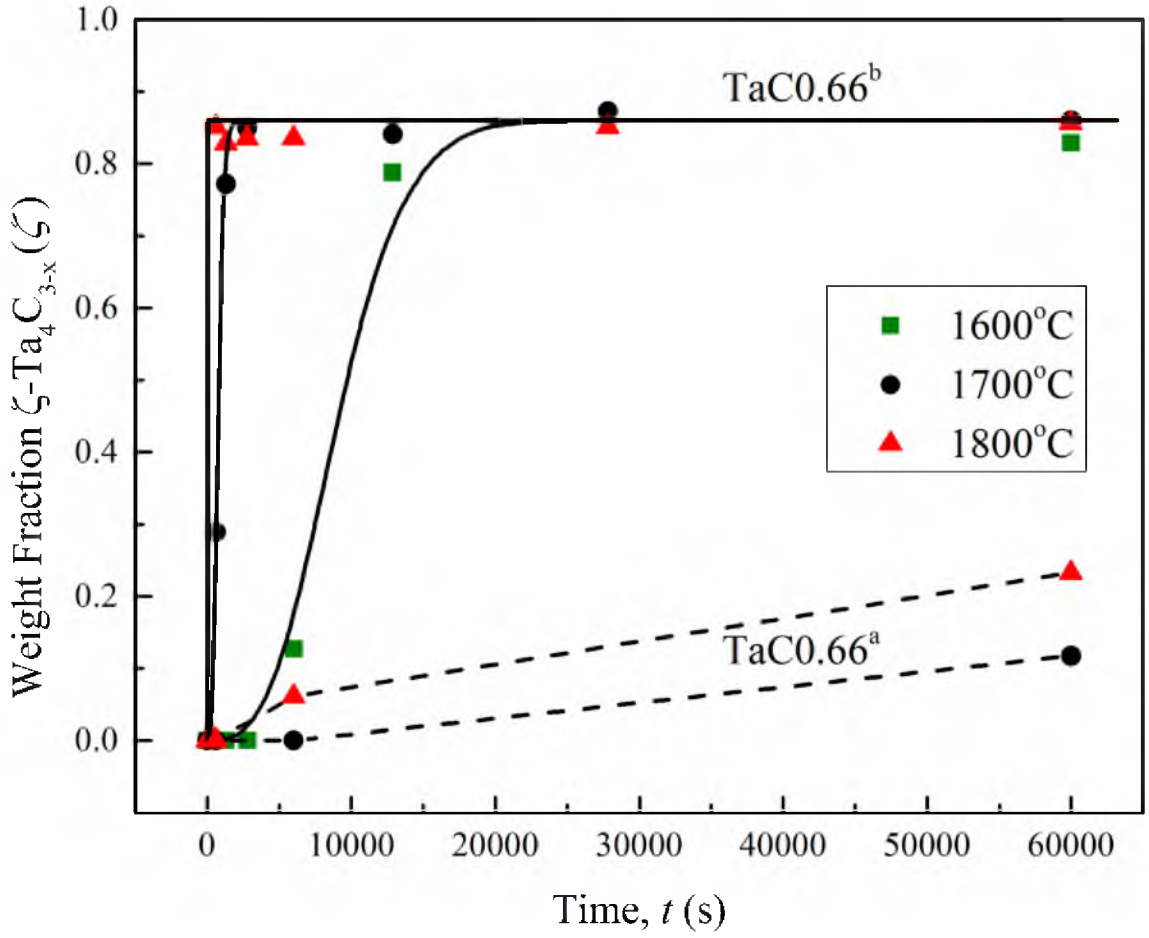

Figure 4.12 Weight fraction of ζ-Ta_4C_{3-x} phase formed in the $TaC_{0.66}$[a] and $TaC_{0.66}$[b] pellets at temperatures between 1600°C and 1800°C.

1600°C, for example, there was no evidence of ζ-Ta_4C_{3-x} after sintering for 2780 s. The weight fraction of the ζ-Ta_4C_{3-x} phase increased to 0.13 in 6000 s and to 0.78 in 12900 s. Thus, there was a clear incubation period associated with the formation of ζ-Ta_4C_{3-x} at this temperature. Increasing the sintering temperature to 1700°C and 1800°C almost completely eliminated the incubation period. At 1800°C, a maximum weight fraction of approximately 0.86 was obtained in only 600 s. Further increase in either time or temperature did not increase the maximum weight fraction of ζ-Ta_4C_{3-x} that could be obtained in pressureless sintering.

The kinetics of formation of the ζ-Ta_4C_{3-x} phase during pressureless sintering of the TaC0.66[b] pellets could be described by the following form of the JMAK equation:

$$\zeta(t,T) = \zeta_\infty \left[1 - \exp\left\{-(\kappa t)^3\right\}\right] \tag{4.3}$$

In Eq. (4.3), $\zeta(t,T)$ is the weight fraction of ζ-Ta_4C_{3-x} formed in time, t, and temperature, T, ζ_∞ is the maximum weight fraction of ζ-Ta_4C_{3-x} that could be obtained in pressureless sintering, κ is a temperature-dependent rate constant. The "best fits" of Eq. (4.3) with the optimized values of the rate constants are shown by the solid lines in Figure 4.12. It is noted that Eq. (4.3) gives adequate fits to the data including the representation of the incubation period observed at 1600°C. The temperature dependence of the rate constant, κ, could also be described by the Arrhenius equation. This is illustrated in Figure 4.13. The activation energy for the formation of ζ-Ta_4C_{3-x} was, however, significantly higher, Q_2 = 1007 ± 151 kJ/mole.

Figure 4.14 shows plots of the weight fraction of the ζ-Ta_4C_{3-x} phase formed

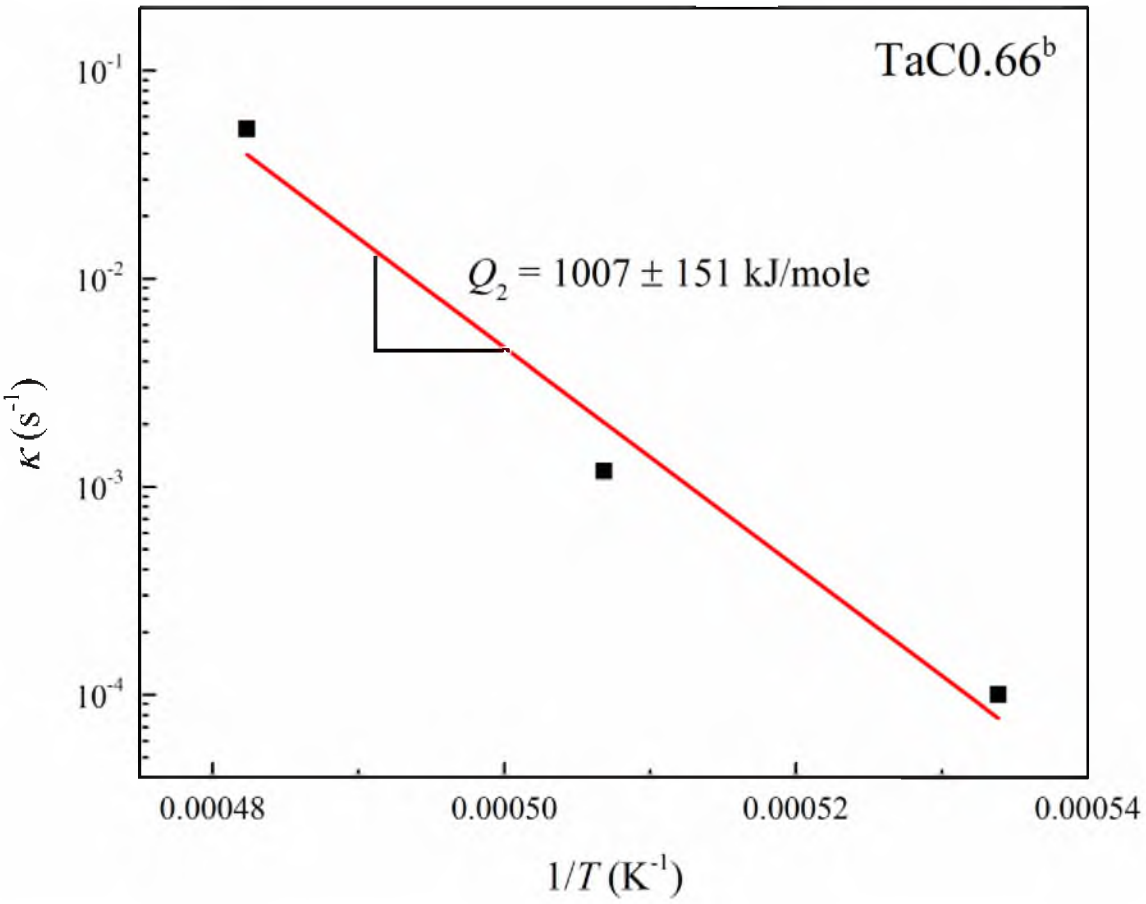

Figure 4.13 Plot of $\log_{10} \kappa$ vs $1/T$ for the kinetics of formation of the ζ-Ta_4C_{3-x} phase in the $TaC0.66^b$ pellets.

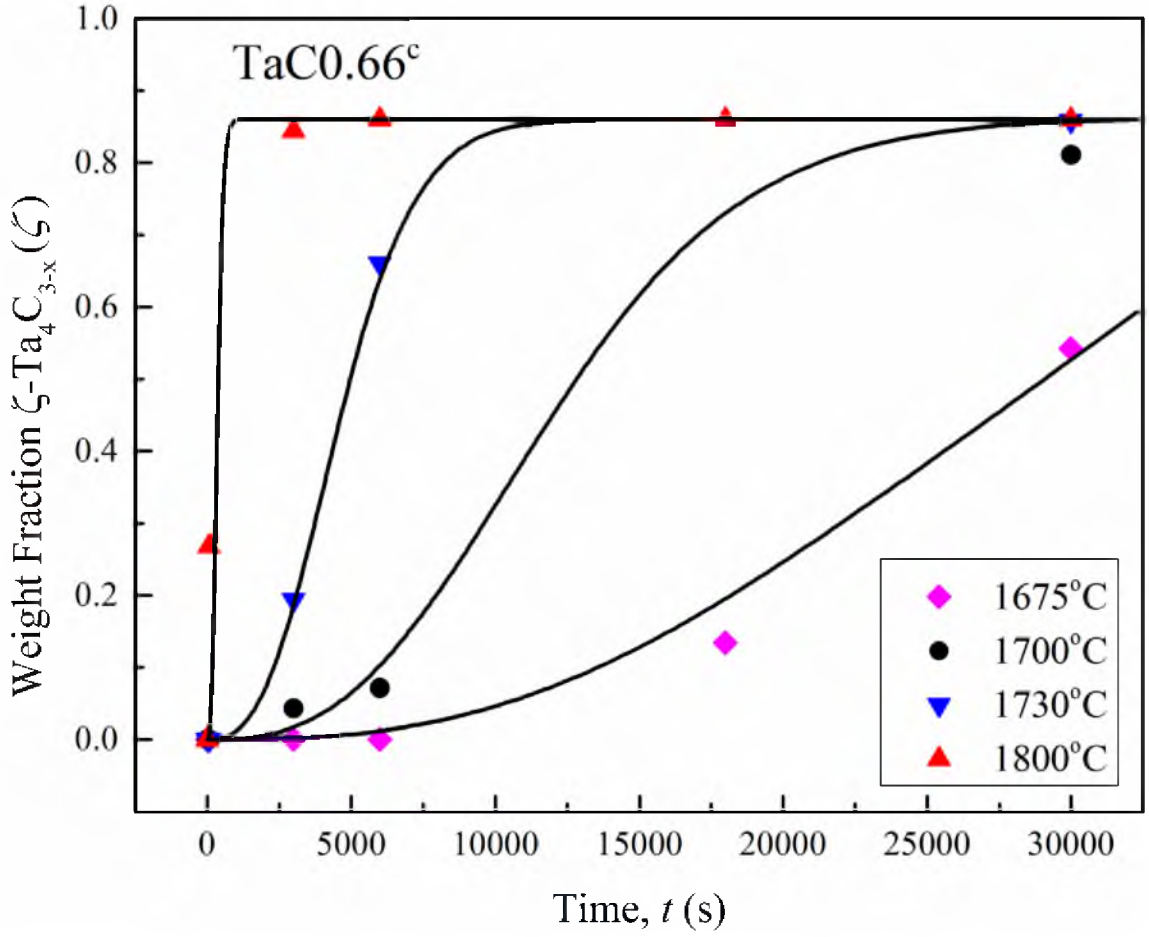

Figure 4.14 Weight fraction of ζ-Ta_4C_{3-x} phase formed in the $TaC_{0.66}^{c}$ pellets at temperatures between 1675°C and 1800°C.

during sintering at various temperatures in pellets of the TaC0.66[c] powder. The ζ-Ta_4C_{3-x} phase formed rapidly over narrow ranges of both time and temperature. At 1675°C, for example, there was no evidence of ζ-Ta_4C_{3-x} after sintering for 6000 s. The weight fraction of the ζ-Ta_4C_{3-x} phase increased to 0.13 in 18000 s and to 0.54 in 30000 s. At 1700°C there was no evidence of ζ-Ta_4C_{3-x} after sintering for 60 s. The weight fraction of the ζ-Ta_4C_{3-x} phase increased to 0.07 in 6000 s and to 0.81 in 30000 s. The incubation period was also present at 1730°C but was absent at 1800°C. At 1800°C, a maximum weight fraction of approximately 0.86 was obtained in 6000 s. Further increase in time did not increase the maximum weight fraction of ζ-Ta_4C_{3-x} that could be obtained in pressureless sintering of the TaC0.66[c] pellets.

The "best fits" of Eq. (4.3) with the optimized values of the rate constants are shown by the solid lines in Figure 4.14. It is noted that Eq. (4.3) gives adequate fits to the data including the representation of the incubation period observed at 1675°C, 1700°C and 1730°C. The temperature dependence of the rate constant, κ, could also be described by the Arrhenius equation. This is illustrated in Figure 4.15. The activation energy for the formation of ζ-Ta_4C_{3-x} in the TaC0.66[c] pellets was Q_2 = 1170 ± 42 kJ/mole, very close to the TaC0.66[b] pellets. The significance of the activation energies estimated and of the JMAK exponents fitted to the kinetics of formation of both α-Ta_2C_y and ζ-Ta_4C_{3-x} phases will be addressed in the Discussion section.

4.7 Optical and EBSD Analyses of the Microstructures

Figure 4.16(a) and Figure 4.16(b) show microstructures of a pellet of the TaC0.66[b] powder sintered at 1800°C for 6000 s and the TaC0.66[a](HP+HIP) billet hot-

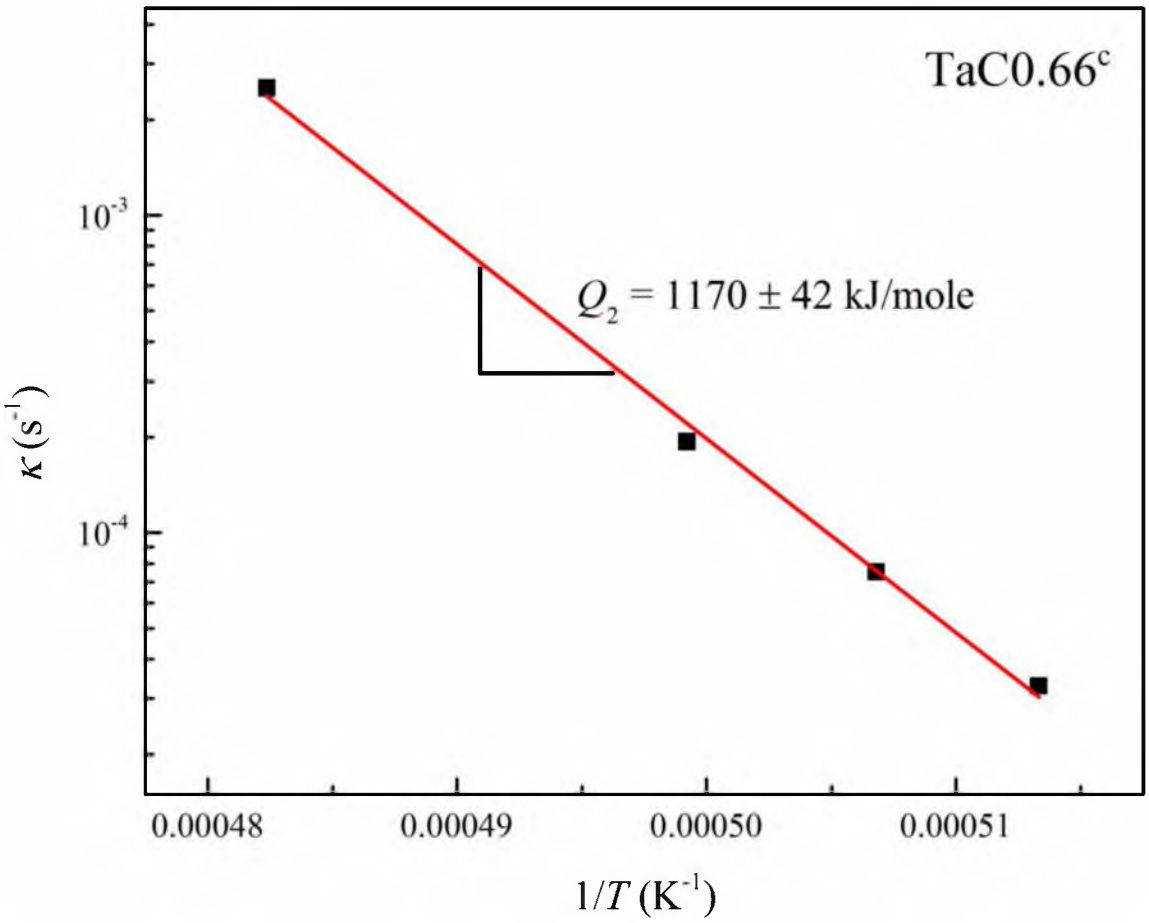

Figure 4.15 Plot of $\log_{10} \kappa$ vs $1/T$ for the kinetics of formation of the ζ-Ta_4C_{3-x} phase in the $TaC0.66^c$ pellets.

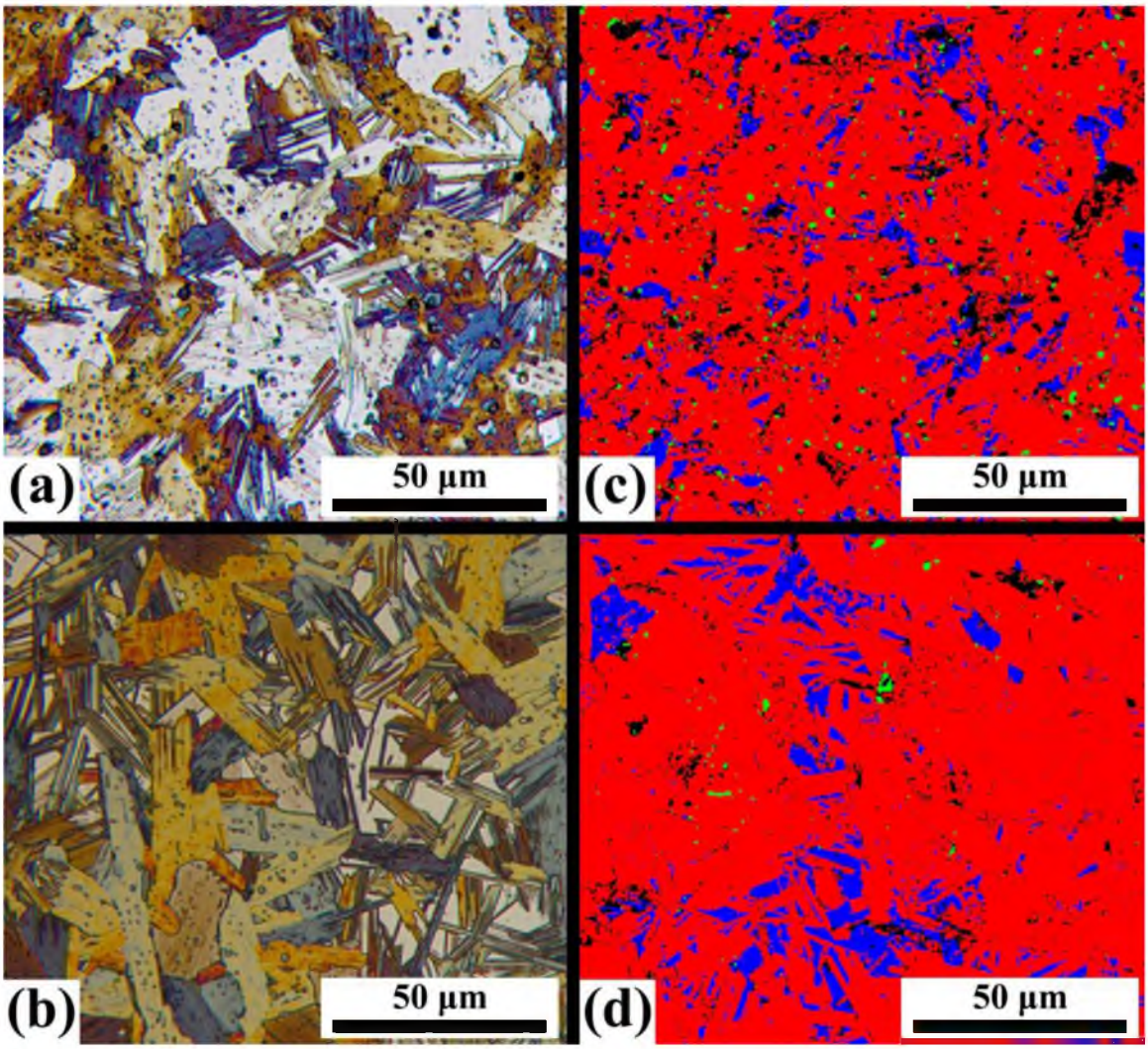

Figure 4.16 Optical images of etched microstructures of (a) a TaC0.66[b] pellet sintered at 1800°C for 6000 s, and (b) a TaC0.66[a](HP+HIP) billet, and EBSD image maps of (c) the TaC0.66[b] pellet sintered at 1800°C for 6000 s, and (d) the TaC0.66[a](HP+HIP) billet. Color code for EBSD: red: ζ-Ta_4C_{3-x}; blue: γ-$TaC_{0.78}$; green: δ-Ta_2O_{5-x}; black: undetermined phase(s) including voids.

pressed and HIPed at 1800°C, respectively. The sintered pellet showed uniform microstructure consisting of elongated, plate-shaped grains of the ζ-Ta_4C_{3-x} phase, 10-20 μm in size. There was evidence of a lamellar substructure within the grains, with each lamella ranging in thickness from 40 to 300 nm. The lamellar substructure was more apparent in some grains, not so in others, presumably due to differences in the orientations of the individual grains. The lamellar substructure becomes very apparent on a polished and indented surface of the $TaC_{0.66}^{a}$(HP+HIP) billet, as shown in Figure 4.17. In addition to the lamellar substructure, there was evidence of second-phase particles, pullout of the particles, and some residual porosity. The sizes of these features were much smaller than the grain size of the ζ-Ta_4C_{3-x} phase. The microstructures of the pellets sintered at 1700°C and 1900°C were very similar to that for the pellet sintered at 1800°C. In particular, there was no evidence of growth of the ζ-Ta_4C_{3-x} phase as the sintering temperature was increased.

The microstructure of the $TaC_{0.66}^{a}$(HP+HIP) billet (Figure 4.16(b)) was inhomogeneous at a macroscale. There were regions of the microstructure that consisted of a cluster of plate-shaped grains with parallel lamellae and dispersion of second phases/voids within the grains. These clusters were surrounded by regions where the ζ-Ta_4C_{3-x} phase had a needle-like structure with multiple orientations. The grain boundaries were not well-defined within this structure. There was evidence of a retained parent phase in between the needles.

Figure 4.16(c) and Figure 4.16(d) show EBSD images of the microstructure of the $TaC_{0.66}^{b}$ pellet sintered at 1800°C and of the $TaC_{0.66}^{a}$(HP+HIP) billet hot-pressed and HIPed at 1800°C, respectively. These images were designed to represent the different

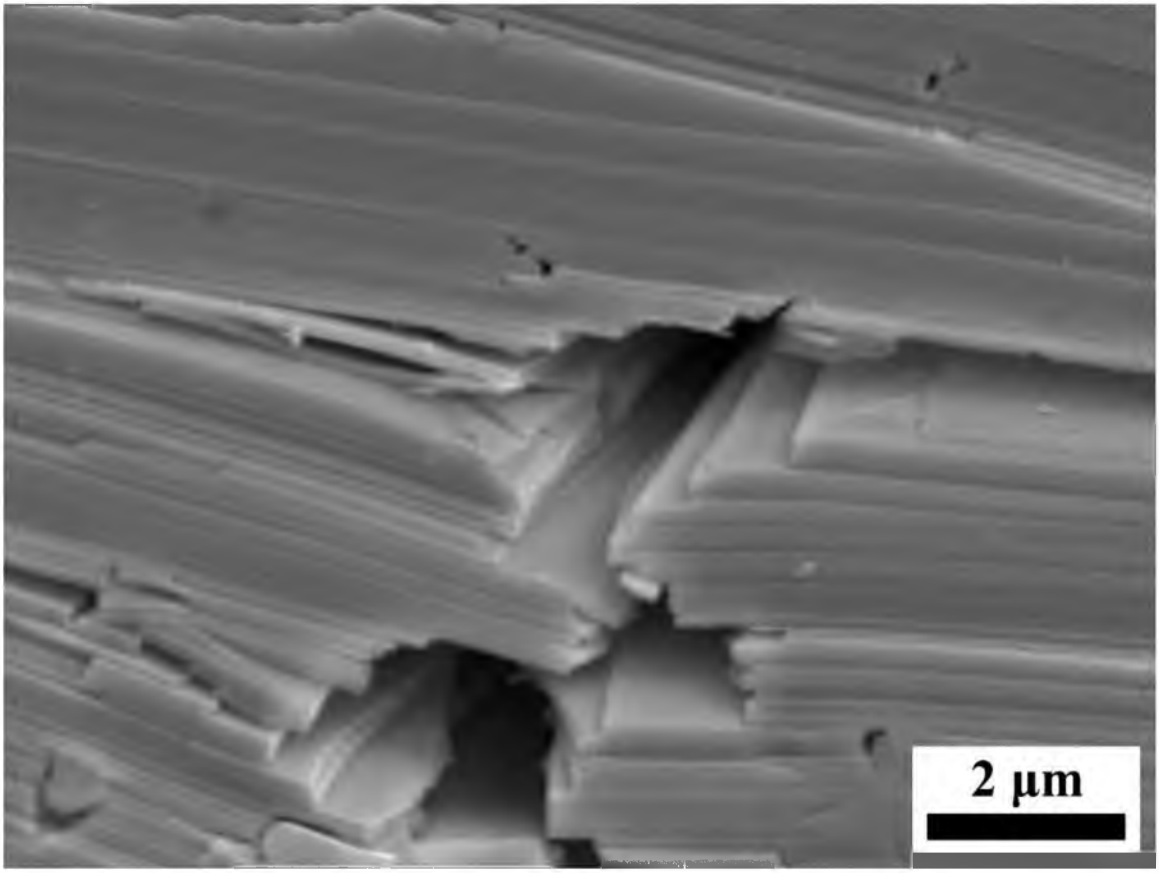

Figure 4.17 The lamellar substructure of the ζ-Ta_4C_{3-x} phase as revealed by a polished and indented surface of the TaC0.66[a] hot-pressed and HIPed billet.

crystallographic phases with different colors based on their characteristic Kikuchi diffraction patterns. The red color represents the ζ-Ta_4C_{3-x}; the blue color corresponds to the residual γ-TaCy phase; the green color was found to correspond to an oxide phase, δ-Ta_2O_{5-x}; and the black color corresponded to voids, pullouts and any unidentified phase(s). The area fractions of the four phases in the two materials, as estimated by EBSD, are listed in Table 4.1. The area fractions of the ζ-Ta_4C_{3-x} and the γ-TaC_y phases, estimated by EBSD, were slightly less than the weight fractions of these phases estimated by X-ray diffraction (see Table 4.1). This was expected since X-ray analysis did not account for the voids, pullouts and the low-density δ-Ta_2O_{5-x} phase. The EBSD images confirmed the difference in the distribution of the two major phases, ζ-Ta_4C_{3-x} and the γ-TaC_y, in the $TaC_{0.66}^{a}$(HP+HIP) billet and the sintered $TaC_{0.66}^{a}$ pellet. In the sintered material, the two major phases were more uniformly distributed. In the hot-pressed and HIPed material, there were clusters of the ζ-Ta_4C_{3-x} phase surrounded by two-phase mixtures of ζ-Ta_4C_{3-x} and γ-TaC_y.

4.8 Discussion

Most carbides, in general, and transition-metal carbides in particular, are difficult to sinter due to their low diffusivities as a result of covalent bonding and high melting points. Tantalum carbides have generally been processed to high density by some form of pressure-assisted sintering, hot-pressing [3, 13], canned hot-isostatic pressing [14, 15], or spark plasma sintering [5, 16]. This chapter reports, for the first time, the processing of a tantalum carbide, ζ-Ta_4C_{3-x}, to high density (> 94% of theoretical) by pressureless sintering. Interest in ζ-Ta_4C_{3-x} arises from its nano-lamellar substructure due to easy-

Table 4.1 Weight fractions of the phases obtained by XRD compared with area fractions measured by EBSD.

	XRD	
Phase	TaC0.66[a] (HP + HIP)	TaC0.66[b]
ζ-Ta_4C_{3-x}	0.95	0.84
γ-TaC_y	0.03	0.16
α-$Ta_2C_{y'}$	0.02	0
δ-Ta_2O_{5-x}	0	0
	EBSD	
Phase	TaC0.66[a] (HP + HIP)	TaC0.66[b]
ζ-Ta_4C_{3-x}	0.85	0.78
γ-TaC_y	0.10	0.09
α-$Ta_2C_{y'}$	0	0
δ-Ta_2O_{5-x}	0.004	0.01
Undetermined	0.05	0.11

cleaving basal planes (Figure 4.17) and its central role in the high fracture toughness of this carbide. Although ζ-Ta_4C_{3-x} carbide has been noted as a secondary phase in compositions bounded by $0.5 > C/Ta > 0.78$ and processed to high density by pressure-assisted sintering [3, 5], this chapter reports a first attempt at producing a dense and near-single-phase material containing the ζ-Ta_4C_{3-x} carbide by pressureless sintering. Both densification and formation of the ζ-Ta_4C_{3-x} phase were promoted by the high energy planetary milling of Ta and γ-TaC powder, and more so by the hydrogenation of the Ta metal powder to produce β-TaH_x prior to milling with γ-TaC powder. Commercially-available Ta metal powders are typically coarse and highly agglomerated. Milling of this powder leads to deformation and formation of large, flake-like agglomerates. These agglomerates do not pack well with the much finer, equiaxed γ-TaC particles. The low packing density and associated large pores and long diffusion distance in the Ta agglomerates suppress both densification and formation of the α-$Ta_2C_{y'}$ phase, the precursor to the ζ-Ta_4C_{3-x} phase. The β-TaH_x phase formed on hydrogenation of the Ta metal powders/agglomerates is significantly harder and more brittle than the Ta metal. Milling of the hydrogenated powder leads to more efficient comminution by breaking down the Ta agglomerates without significant deformation. This leads to smaller and more equiaxed Ta metal particles and more efficient packing with the γ-TaC powder. Figure 4.18 shows the effects powder processing had on the formation of the ζ-Ta_4C_{3-x} phase when sintered at 1700°C. Powders with smaller and more equiaxed powder morphology had a significantly decreased sintering time required to reach a high quantity of ζ-Ta_4C_{3-x} phase formation.

The inhomogeneous microstructure seen in the hot-pressed billet, Figure 4.16(b),

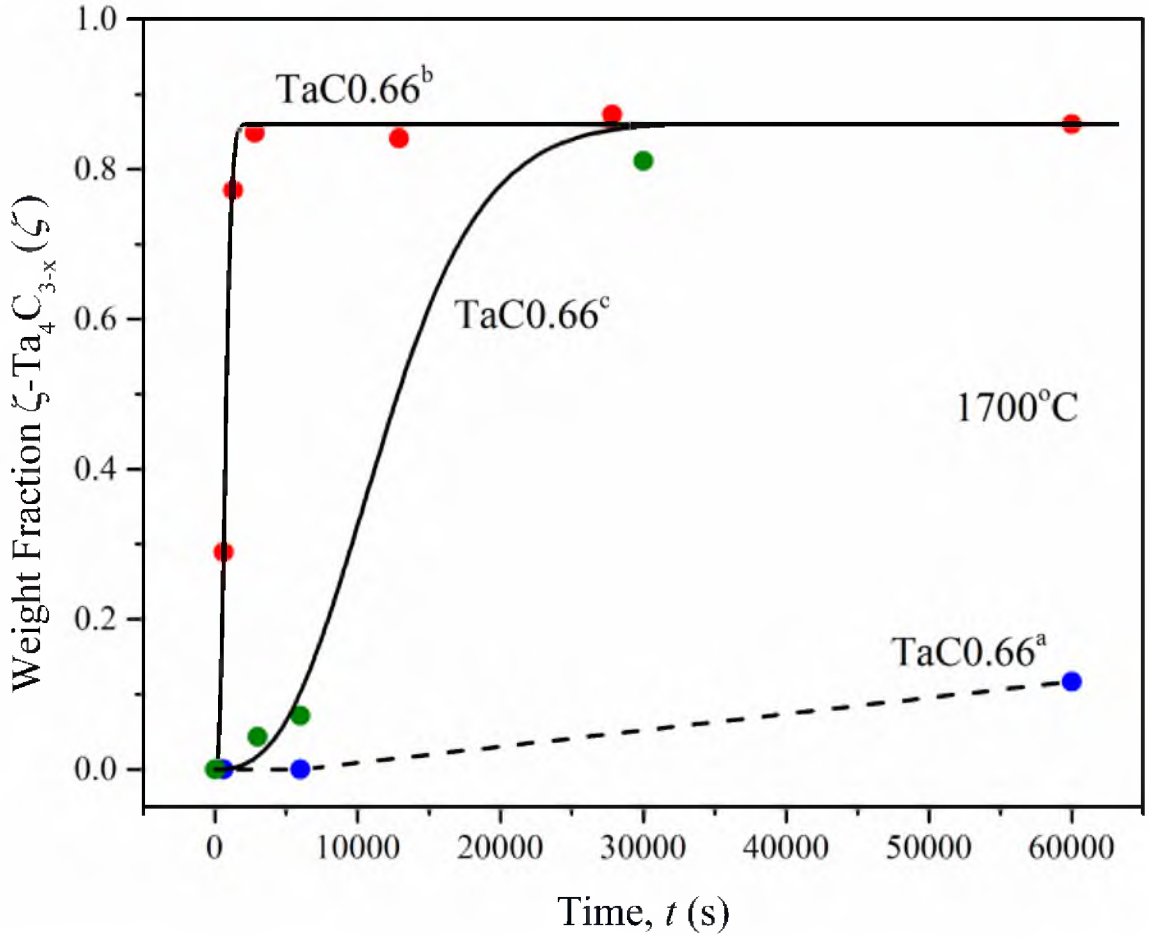

Figure 4.18 Weight fraction of ζ-Ta_4C_{3-x} phase formed in the $TaC_{0.66}$[a], $TaC_{0.66}$[b] and $TaC_{0.66}$[c] pellets when sintered at a temperature of 1700°C.

can be rationalized in the following way. The clusters of the ζ-Ta_4C_{3-x} grains seen in Figure 4.16(b) are believed to have been nucleated in the α-Ta_2C_y grains derived from the large, plate-like particles of Ta metal. Since α-Ta_2C_y has an hcp structure and shares the same close-packed Ta metal planes with the ζ-Ta_4C_{3-x} phase, only one variant of the ζ-Ta_4C_{3-x} phase is nucleated. This is the reason why the parallel substructure spans the entire ζ grain. Surrounding these clusters of monovariant ζ grains is a two-phase region consisting of multivariant ζ platelets in a retained fcc matrix. This region appears as needles of ζ of multiple orientations with the retained fcc phase in between (see Figure 4.16(b)). This large-scale inhomogeneity is not seen in the microstructure of the sintered material (Figure 4.16(a)).

The phase evolution in the TaC0.66[b] pellets as a function of temperature, shown in Figure 4.7, suggests that formation of the ζ-Ta_4C_{3-x} phase from the β-TaH_x and γ-TaC powder mixture occurs in four stages. The first stage is the decomposition of β-TaH_x which produces Ta metal:

$$0.34\beta TaH_x \rightarrow 0.34Ta + 0.17xH_2(g) \tag{4.4}$$

Based on the Ta-H phase diagram, the above reaction takes place at temperatures at and above the hydrogenation temperature (300-350°C) as the solubility of atomic H in Ta decreases with increasing temperature [44]. The nascent atomic H from β-TaH_x also reacts with oxygen dissolved in the Ta metal lattice, leading to partial deoxidation of the metal.

The second stage of the overall process is the conversion of the Ta metal to α-

$Ta_2C_{y'}$ with y' taking the value 0.86 with a concurrent depletion of C in the γ-TaC phase:

$$0.34Ta + 0.66\gamma TaC \rightarrow 0.17\alpha Ta_2C_{0.86} + 0.66\gamma TaC_{0.78} \quad (4.5)$$

It should be noted that in the above reaction the C concentration in the substoichiometric γ-TaC_y phase, i.e., y = 0.78, was established from its lattice parameter (Figure 4.7), while the C concentration in the substocihiometric α-$Ta_2C_{y'}$ was calculated from mass balance. This calculated composition of α-$Ta_2C_{y'}$ is consistent with the phase diagram of Figure 1.1 since the C/Ta ratio of the left boundary of α-$Ta_2C_{y'}$ at 1800°C is 0.43. The reaction of Eq. (4.5) must involve two steps: (a) diffusion of C from γ-TaC_y to Ta, and (b) nucleation and growth of α-$Ta_2C_{0.86}$ when the C concentration in the Ta metal exceeds the solubility limit. The analyses of the kinetics of formation of α-$Ta_2C_{y'}$ in Figures 4.8 and 4.10 indicated that the JMAK equation with an exponent, n = 0.5, gave reasonable fits to the time dependence of volume fraction transformed with the rate constant showing an Arrhenius temperature dependence. An exponent of 0.5 is typical of a transformation where the product phase grows by thickening of large plates, i.e., after complete edge impingement [80]. This is a likely situation in the second stage since α-$Ta_2C_{y'}$ grains are known to exhibit plate morphology with much higher growth rates in the basal plane than in the c-direction. The observation of the parabolic growth of the α-$Ta_2C_{y'}$ layer in Ta-C diffusion couples made by Brizes [54] supports this interpretation. In the transformation of Ta metal to α-$Ta_2C_{y'}$, the rate-controlling process is likely to be the diffusion of C through the α-$Ta_2C_{y'}$ phase. The activation energy estimated for the formation of α-$Ta_2C_{y'}$, i.e., Q_1 = 219 kJ/mole, should correspond to the activation energy

for the diffusion of C in the hcp structure of the α-Ta_2C_y phase. Three studies have reported activation energies for C diffusion in α-Ta_2C_y: 299 kJ/mole (Yeh *et al.* [50]), 405 kJ/mole (Hartmann *et al.* [76]) and 481 kJ/mole (Brizes [54]). The experiments involved diffusion of C into either powder or bulk forms of Ta metal. The three values of the activation energies were obtained in experiments at increasing temperature ranges, 1700°C to 1800°C, 2000°C to 2200°C, and 2100°C to 2600°C, respectively. Thus, the activation energies reported in the literature scaled with the temperature range of the experiments. It has been suggested that both bulk and grain-boundary diffusion contribute to diffusion of C in α-Ta_2C_y with the grain-boundary contribution increasing with decreasing temperature [76]. Typically, the activation energy for bulk diffusion is higher than that for surface/grain-boundary diffusion. The low activation energy assessed in the present study may well reflect grain-boundary diffusion of C in α-Ta_2C_y at the low temperatures investigated (900-1200°C).

The third stage of the process, represented by the following reaction, can be described as equilibration of the α-Ta_2C_y and γ-$TaC_{0.78}$ phases prior to forming the ζ-Ta_4C_{3-x} phase:

$$0.17\alpha Ta_2C_{0.86} + 0.66\gamma TaC_{0.78} \rightarrow 0.215\alpha Ta_2C + 0.57\gamma TaC_{0.78} \quad (4.6)$$

It is noted in Figure 4.7 that this third stage of the process begins at a temperature slightly above 1200°C. This results in an increase of the weight fraction of the α-Ta_2C phase to 0.43 and a decrease of the weight fraction of γ-$TaC_{0.78}$ phase to 0.57, consistent with the lever rule applied to a bulk composition of TaC0.66 prior to the nucleation and growth of

the ζ-Ta_4C_{3-x} phase.

The fourth and final stage of formation of the ζ phase can be represented by the following balanced reaction:

$$0.215\alpha Ta_2C + 0.57\gamma TaC_{0.78} \rightarrow 0.215\zeta Ta_4C_{2.56} + 0.14\gamma TaC_{0.78} \quad (4.7)$$

During this step the ζ-Ta_4C_{3-x} phase nucleates and grows on the close-packed Ta planes in both the α-Ta_2C (hcp) phase and the γ-$TaC_{0.78}$ (fcc) phase as all three phases share the same close-packed Ta planes. The growth rate of the ζ phase is likely to be much higher on the basal plane than normal to it. In the α-Ta_2C phase, the growth of the ζ-Ta_4C_{3-x} phase is relatively unimpeded since all nuclei within a grain grow predominantly parallel to each other without interference. In the γ-$TaC_{0.78}$ grains, however, ζ grains can nucleate on four independent close-packed planes and their growth can interfere with each other. This interpretation explains why the microstructures show some retained γ phase even though the gross composition, TaC0.66, is in the single ζ phase range in the phase diagram. It is interesting to note here that the amount of the retained γ phase was less in the hot-pressed and HIPed material [$TaC0.66^a$(HP+HIP)] relative to the pressureless sintered material. This influence of the applied pressure on the formation of the ζ phase is reasonable when we note that the ζ phase has a higher density relative to the γ phase.

The growth kinetics of the ζ-Ta_4C_{3-x} phase in the $TaC0.66^b$ and $TaC0.66^c$ pellets were fitted using the JMAK equation with an exponent of 3. An JMAK exponent of 3 is representative of a transformation where the growth of the phase is interface controlled with site saturation for nucleation [80]. The rate-controlling process for this

transformation would be short-range diffusion across the interface for the slower moving species, i.e., Ta.

The phase diagram of Figure 1.1, which is based on the work of Gusev *et al.* [1], indicates that the ζ-Ta_4C_{3-x} phase is stable from room temperature (~25°C) to 2130°C. Some early studies of this phase, for example by Zaplatynsky [51], concluded that ζ-Ta_4C_{3-x} phase was metastable and formed by a diffusionless transformation of the γ-TaC_y phase under compressive stress. This conclusion was based on decrease of the intensities of the XRD peaks of the ζ-Ta_4C_{3-x} phase when a section of a diffusion couple rich in this phase was comminuted. ζ-phase stability was investigated in this study by comminuting a bar fabricated from the hot-pressed billet that initially contained 0.95 weight fraction ζ-Ta_4C_{3-x} phase. The XRD on the comminuted sample showed the same amount of the ζ phase. There was also no evidence of phase transformation when a bar with 0.95 weight fraction ζ-Ta_4C_{3-x} phase was annealed at 1200°C for 20 hr. These two results were taken as support for the thesis that ζ-Ta_4C_{3-x} is a stable phase, as indicated by the phase diagram of Figure 1.1.

CHAPTER 5

ζ-Ta_4C_{3-x}: A HIGH FRACTURE TOUGHNESS CARBIDE WITH RISING-CRACK-GROWTH-RESISTANCE (R-CURVE) BEHAVIOR

5.1 Introduction

This chapter reports the results of a study undertaken with three objectives. The first objective was to see if the high fracture toughness reported for tantalum carbides in the prior studies [3-5] can be further enhanced by increasing the content of the ζ-Ta_4C_{3-x} phase via control of the C/Ta ratio in the starting powder mixture. The second objective was to compare the mechanical properties of compacts consolidated by hot-pressing with those of pressureless-sintered compacts to see if there is a significant drop in the properties. The final objective was to understand why ζ-Ta_4C_{3-x} has much higher fracture toughness as compared to the monocarbide and the hemicarbide. The results will demonstrate that compacts hot-pressed from a powder mixture with a C/Ta atomic ratio of 0.66 contain about 95 w% of ζ-Ta_4C_{3-x} and exhibit a rising crack-growth-resistance (R-curve) behavior with fracture toughness ranging from 11 to 15 MPa$\sqrt{m}$ with adequate strength (760 MPa) and modest hardness (6 GPa). The properties of the pressureless-sintered compacts are slightly inferior, but are still very attractive. The high fracture toughness of ζ-Ta_4C_{3-x} is related to the easy cleavage of the basal planes and bridging of

cracks by nano-lamellae, a characteristic it shares with Ti_3SiC_2 [20] and other similar phases [22].

5.2 Densities, Phase Contents and Grain Sizes

Table 5.1 lists the materials processed, their measured densities, weight percents of the phases present, lattice parameters of the phases, and densities expressed as percents of theoretical desnity. The composition of primary interest here is TaC0.66, the composition expected to yield single-phase ζ-Ta_4C_{3-x} based on the phase diagram of Figure 1.1. The microstructures, phase contents and properties of this material will be compared and contrasted with both single-phase α-Ta_2C and single-phase γ-TaC_y, and two-phase composites of these phases with the ζ-Ta_4C_{3-x} phase. For this purpose, we have included some results obtained previously by Hackett *et al.* [3, 4].

The measured density decreased slightly with increasing C/Ta atomic ratio from 14.89 g/cc for the $TaC0.50^a$(HP) material to 14.05 g/cc for the $TaC1.0^a$(HP) material. As percent of theoretical density, the density variation was from 99.1% for the $TaC0.50^a$(HP) material to 95.8% for the $TaC0.60^a$(HP) material. The compositions that produced single phases were consistent with the phase diagram of Figure 1.1. Thus, for example, $TaC0.50^a$(HP) was single-phase α-Ta_2C, as would be expected from Figure 1.1. The three compositions, TaC0.8, TaC0.9 and TaC1.0 all yielded single-phase γ-TaC_y. The measured lattice parameters of γ-TaC_y were consistent with the initial C/Ta ratios of the powders based on the correlation reported by Bowman [56]. This suggested that there was no significant loss or gain of carbon during powder consolidation. Compositions expected to yield two-phase mixtures of α-Ta_2C and γ-Ta_4C_{3-x}, i.e., C/Ta = 0.55, 0.6 and

Table 5.1 Densities, weight percents of phases, lattice parameters, and densities as percents of theoretical density of for various compositions.

Material	Measured Density (g/cc)	Weight percent of phases			Lattice parameters		Density (% theo.)
		α-Ta_2C	ζ-Ta_4C_{3-x}	γ-TaC_y	*a* (Å)	*C* (Å)	
TaC0.50[a](HP)	14.89	100	0	0	3.1067	4.9445	99.1
TaC0.55[a](HP)	14.76	58.2	41.8	0	3.1249(ζ) 3.1066(α)	30.0725(ζ) 4.9415(α)	98.8
TaC0.60[a](HP)[7]	14.26	21	79	0	3.1227(ζ) 3.1039(α)	30.0388(ζ) 4.9273(α)	95.8
TaC0.625[a](HP)	14.7	15	85	0	3.1235(ζ) 3.1067(α)	30.0641(ζ) 4.939(α)	98.8
TaC0.66[a](HP)	14.51	0	95.4	4.6	3.1239	30.0627	97.9
TaC0.66[a](HP+HIP)	14.7	2.5	95	2.5	3.1242	30.077	99.1
TaC0.66[b](PS)	14.37	0	86.7	13.3	3.1239(ζ) 4.4241(γ)	30.0731(ζ)	97.1
TaC0.66[b](PS+HIP)	14.43	0	89.2	10.8	3.1239(ζ) 4.4223(γ)	30.0722(ζ)	97.4
TaC0.70[a](HP)[7]	14.20	0	44.6	55.4	3.1279(ζ) 4.4204(γ)	30.0116(ζ)	96.6
TaC0.80[a](HP)[7]	14.11	0	0	100	4.4244		96.7
TaC0.90[a](HP)[7]	14.03	0	0	100	4.4379		96.5
TaC1.0[a](HP)[7]	14.05	0	0	100	4.4534		97.1

0.625, did show these two phases, but the measured weight fractions of the ζ-Ta_4C_{3-x} phase in the consolidated materials were consistently greater than the values calculated by applying the lever rule in the two-phase region of the phase diagram. Similarly, the composition, TaC0.70, showed a mixture of the phases, ζ-Ta_4C_{3-x} and γ-$TaC_{0.78}$, but the measured weight fraction of the ζ-Ta_4C_{3-x} phase was less than the value calculated from the phase diagram and the lever rule. The TaC0.66 composition was expected to yield single-phase ζ-Ta_4C_{3-x}. However, this composition produced two phases, ζ-Ta_4C_{3-x} and a small amount of γ-$TaC_{0.78}$. The amount of the residual γ-$TaC_{0.78}$ phase varied with the consolidation method. Pressureless sintering produced the highest amount of the residual γ-TaC_y phase at 13.3 w%. HIPing of the pressureless sintered material reduced the residual γ-TaC_y phase to 10.8 w%, but still did not approach the low values of 4.6 w% and 2.5 w% obtained in the hot-pressed ($TaC0.66^a$(HP)) and the hot-pressed and HIPed ($TaC0.66^a$(HP+HIP)) materials. The XRD analyses of the phase contents suggested that the composition range where the ζ-Ta_4C_{3-x} is the single phase is likely shifted to lower values. In fact, a composition range, C/Ta = 0.62-0.65 for ζ-Ta_4C_{3-x}, is more consistent with the measured weight fractions of the phases in the two-phase regions. Wiesenberger *et al.* [81] have reported a range, C/Ta = 0.618-0.639 for the γ-Ta_4C_{3-x} phase based on electron-probe micro-analysis (EPMA) of diffusion couples.

Measurements of grain size by optical microscopy proved to be difficult for materials containing large quantities of the ζ-Ta_4C_{3-x} phase for two reasons: (1) the grain morphology was often complex with poorly defined grain boundaries; (2) etching of the ζ-Ta_4C_{3-x} phase often revealed a lamellar substructure, which increased the difficulty in identifying the grain boundaries. Figure 5.1 illustrates the wide range of microstructures

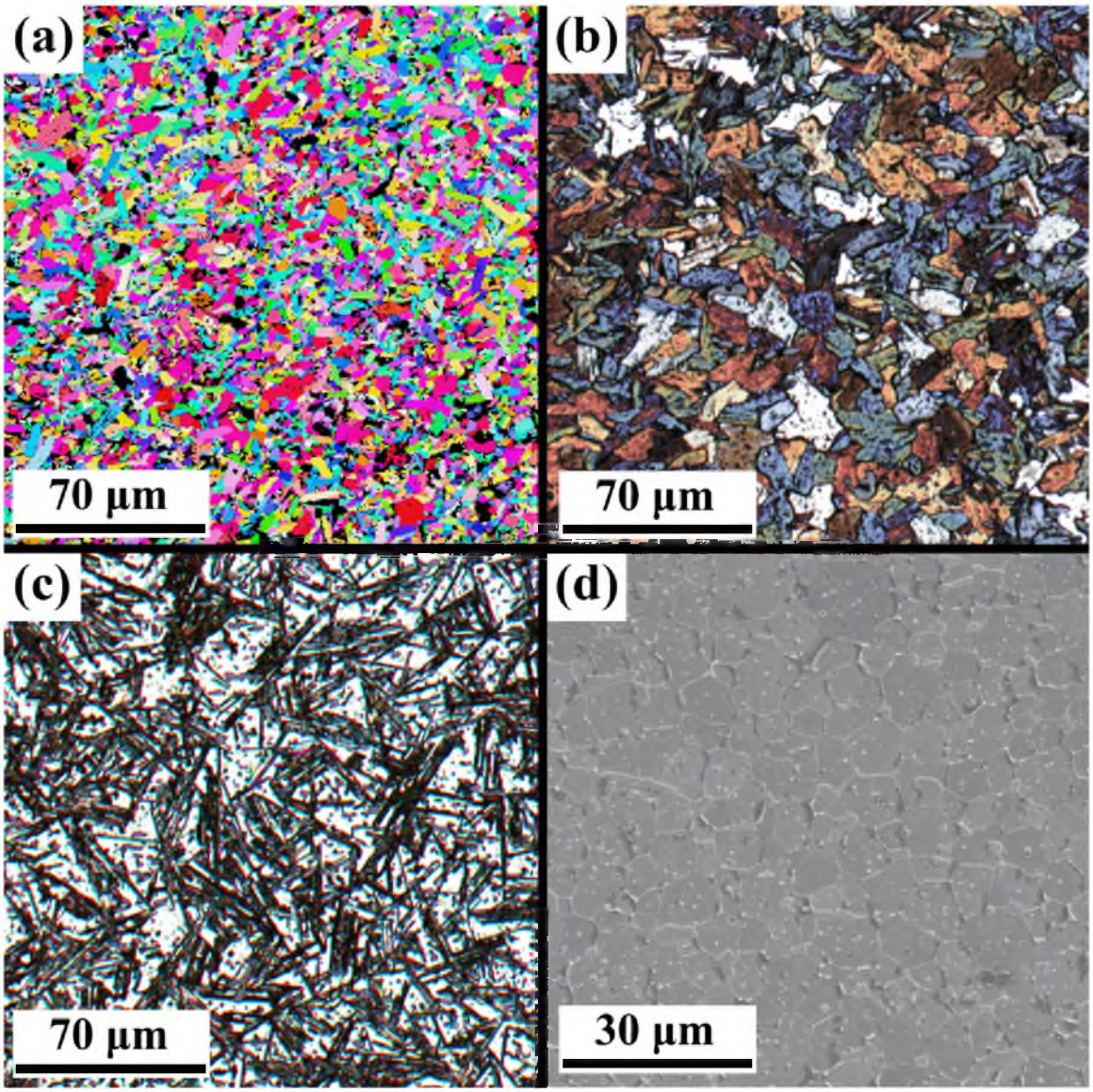

Figure 5.1 EBSD image of (a) TaC0.50[a](HP), optical images of (b) TaC0.66[a](HP) and (c) TaC0.70[a](HP), and SEM images of (d) TaC1.0[a](HP) microstructures.

exhibited by single-phase and two-phase composites of carbides in the Ta-C system. Figure 5.1(a) shows an EBSD orientation image of single-phase α-Ta_2C ($TaC0.50^a$(HP)). The different colors represent grains of different orientations. There was a mixture of both equiaxed and elongated grains. The mean grain size was 3.5 μm. An optical microstructure of $TaC0.66^a$(HP), which was nearly single-phase with 95.4 w% ζ-Ta_4C_{3-x}, is shown in Figure 5.1(b). The microstructure was much coarser than that of the $TaC0.50^a$(HP) material. Most of the grains were elongated with a mean grain size of 8.5 μm. The microstructure of $TaC0.70^a$(HP), Figure 5.1(c), was significantly different from those of the previous materials. The microstructure consisted of randomly oriented needle-like grains (approximately 40 μm long and <3 μm wide) homogeneously dispersed in a matrix. The needle-like grains are the ζ-Ta_4C_{3-x} phase, while the matrix is the parent γ-$TaC_{0.78}$ phase. The $TaC1.0^a$(HP) material had a uniform, equiaxed grain structure (Figure 5.1(d)), with a mean grain size of 7.7 μm. All of the materials showed evidence of a dispersed phase within the primary phase. An EBSD phase analysis indicated that this phase was the oxide, δ-Ta_2O_{5-x}. The weight fraction of the oxide phase was less than 0.01.

EBSD orientation image maps of: (a) $TaC0.66^a$(HP), (b) $TaC0.66^a$(HP+HIP), (c) $TaC0.66^b$(PS) and (d) $TaC0.66^b$(HP+HIP) materials are shown in Figure 5.2. The different colors represent different grain orientations of the phases. In all the images, the black color corresponds to voids, pullouts or any unidentified phase(s). The hot-pressed material (Figure 5.2(a)) showed a uniform microstructure consisting of elongated, plate-shaped grains of the ζ-Ta_4C_{3-x} phase, 5-30 μm in size. The hot-pressed and HIPed $TaC0.66^a$(HP+HIP) material (Figure 5.2(b)) had larger grains than the $TaC0.66^a$(HP)

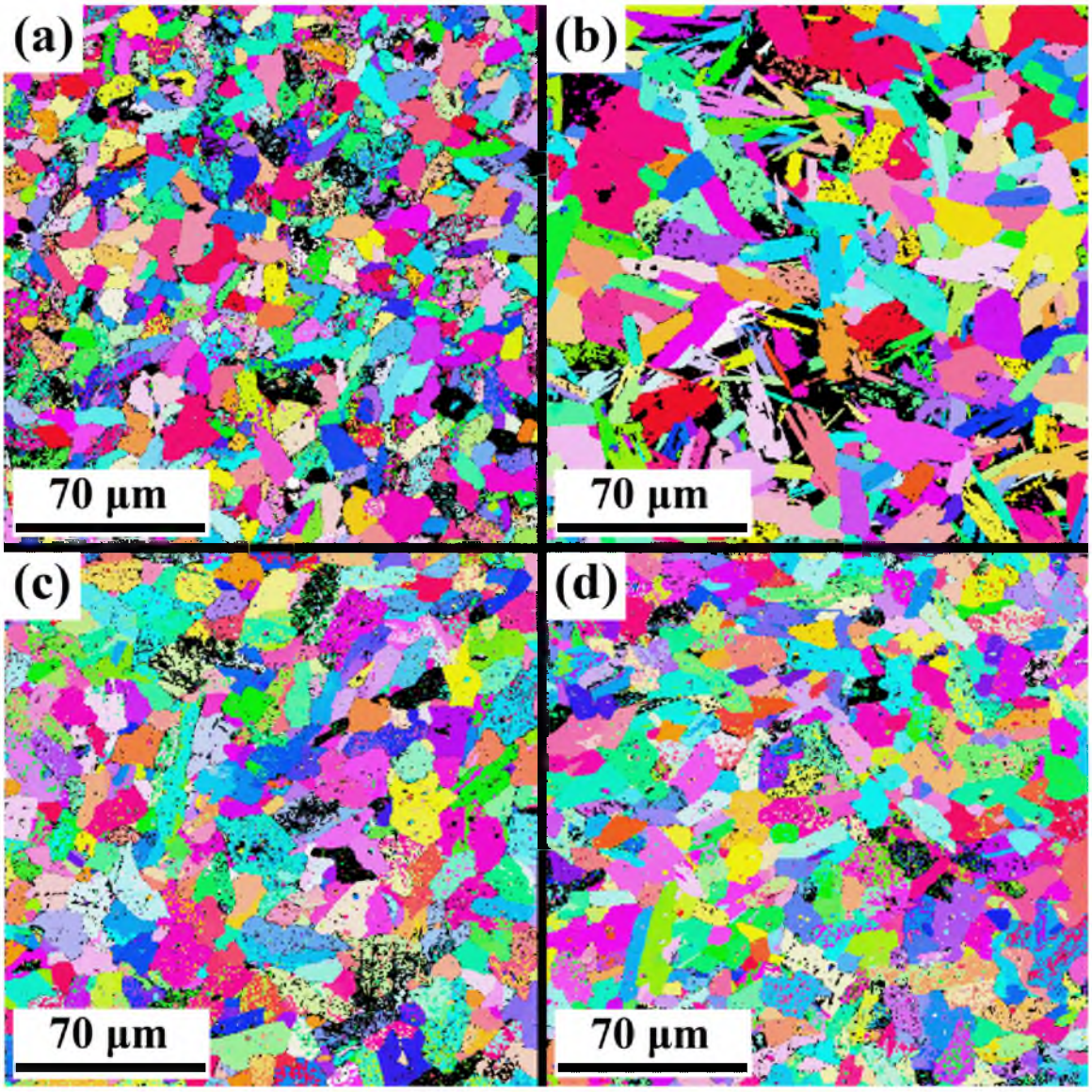

Figure 5.2 EBSD images of etched (a) TaC0.66[a](HP), (b) TaC0.66[a](HP+HIP), (c) TaC0.66[b](PS), and (d) TaC0.66[a](PS+HIP) microstructures.

material. Grains ranged greatly in size and shape and were anywhere from 5 μm or smaller in size and equiaxed in shape, to highly elongated grains approximately 60 μm x 20 μm in size. There were regions of the microstructure that consisted of a cluster of plate-shaped grains with parallel lamellae and a dispersion of second phases/voids within the grains. These clusters were surrounded by regions where the ζ-Ta_4C_{3-x} phase had a needle-like structure with multiple orientations. The hot-pressed $TaC_{0.66}^{a}$(HP) material (Figure 5.2(a)) and the hot-pressed and HIPed $TaC_{0.66}^{a}$(HP+HIP) material (Figure 5.2(b)) had average grain sizes of 8.5 μm and 14.2 μm, respectively, as determined by EBSD. Figure 5.2(c) shows the microstructure of the pressureless sintered $TaC_{0.66}^{b}$(PS) material. The grain size appeared to be smaller than the $TaC_{0.66}^{a}$(HP+HIP) material but slightly larger than the $TaC_{0.66}^{a}$(HP), and showed a uniform microstructure similar to the hot-pressed material. The microstructure of $TaC_{0.66}^{b}$(HP+HIP), shown in Figure 5.2(d), was similar to its hot-pressed counterpart.

5.3 Mechanical Properties

Figure 5.3 shows a plot of the fracture strengths of tantalum carbides from this study and from the study of Hackett *et al.* [3, 4] as a function of their nominal C/Ta atomic ratio in the starting powder mix. The fracture strength was highest for the $TaC_{0.66}^{a}$(HP) material at 759 ± 24 MPa. For the same composition, the strength was lower for the sintered (701 ± 20 MPa) and the sintered and HIPed materials (679 ± 56 MPa), and it was particularly low for the hot-pressed and HIPed material (508 ± 97 MPa). This decrease in strength was consistent with an increase in the average grain size of the material as determined by the consolidation process and temperature. The fracture

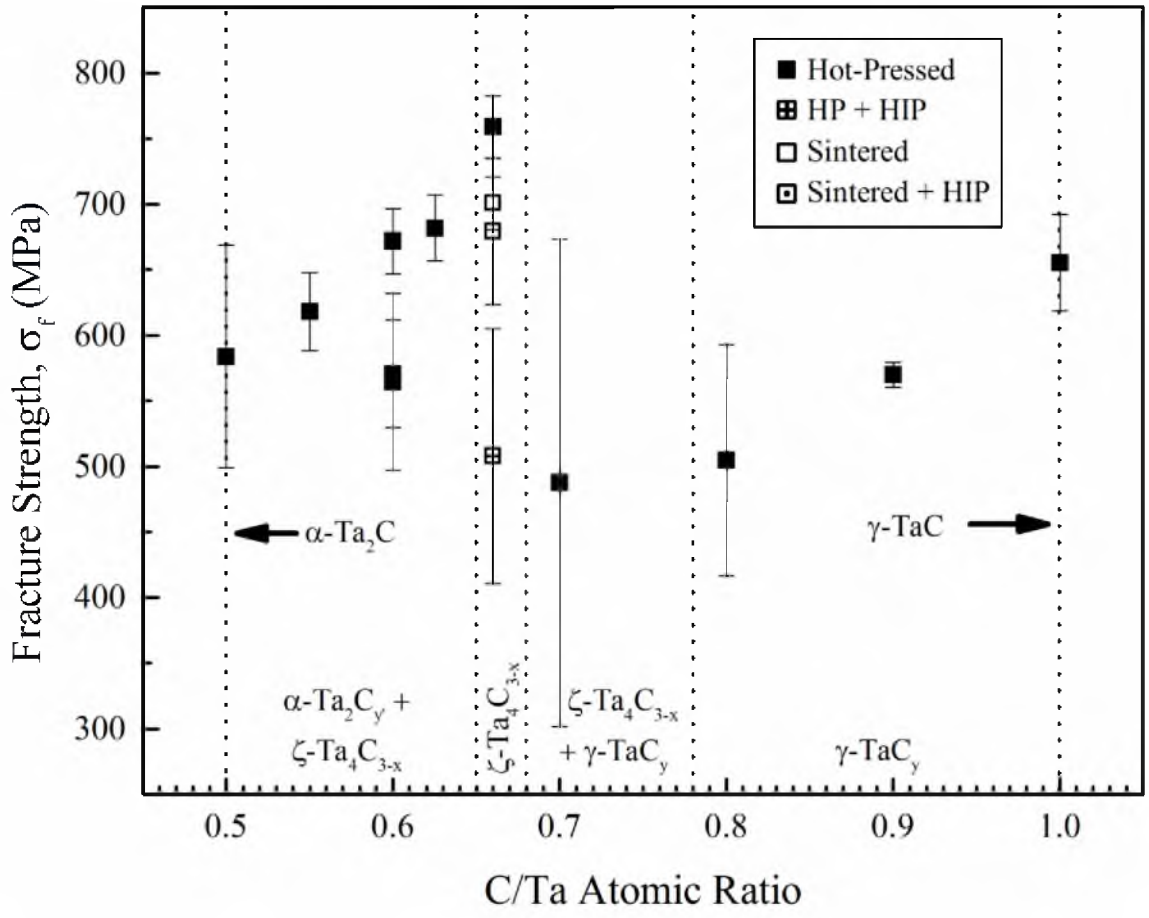

Figure 5.3 Fracture strength of carbides as a function of the C/Ta atomic ratio.

strength decreased with decreasing C/Ta atomic ratio reaching a value of 584 ± 85 MPa for the $TaC_{0.50}^{a}$(HP) material which consisted of 100 w% of the α-Ta_2C phase. It is interesting to note that this material exhibited this low strength despite its high density and small grain size (see Table 5.1 and Figure 5.1(a)). This suggests that ζ-Ta_4C_{3-x} is intrinsically a stronger phase than α-Ta_2C, and there is potential for further increase in strength of a material containing predominantly the ζ-phase by increasing the ζ-phase content, decreasing its grain size and increasing the density by improved powder processing and consolidation. The trend in fracture strength with C/Ta atomic ratio greater than 0.66 was also interesting. There was a precipitous drop in mean strength coupled with a large standard deviation of strength for the $TaC_{0.70}^{a}$(HP) material (488 ±186 MPa). This was despite the presence of the needle-like ζ-Ta_4C_{3-x} grains in the microstructure (Figure 5.1(c). For C/Ta atomic ratios of 0.8, 0.9 and 1.0, the fracture strength increased and reached a value of 655 ± 37 MPa for the stoichiometric γ-TaC.

Figure 5.4 plots the fracture toughness of materials from this study and from Hackett *et al.* [3, 4] as a function of their C/Ta atomic ratio. Beginning at the C/Ta atomic ratio of 0.5, the fracture toughness increased from a value of 8.4 ± 0.2 MPa$\sqrt{m}$ for the single-phase α-Ta_2C to a maximum value of 15.6 ± 0.5 MPa$\sqrt{m}$ for the $TaC_{0.66}^{a}$(HP+HIP) material that contained 95 w% ζ-Ta_4C_{3-x}. It should be noted that this particular material had the highest weight percent and the largest mean grain size for the ζ-Ta_4C_{3-x} phase. This resulted in high fracture toughness, but at the expense of strength. Note that the fracture strength was only 508 ± 97 MPa for this hot-pressed and HIPed material. The hot-pressed material of the same composition, C/Ta = 0.66, had an attractive combination of fracture toughness (13.8 ± 0.2 MPa$\sqrt{m}$) and fracture strength

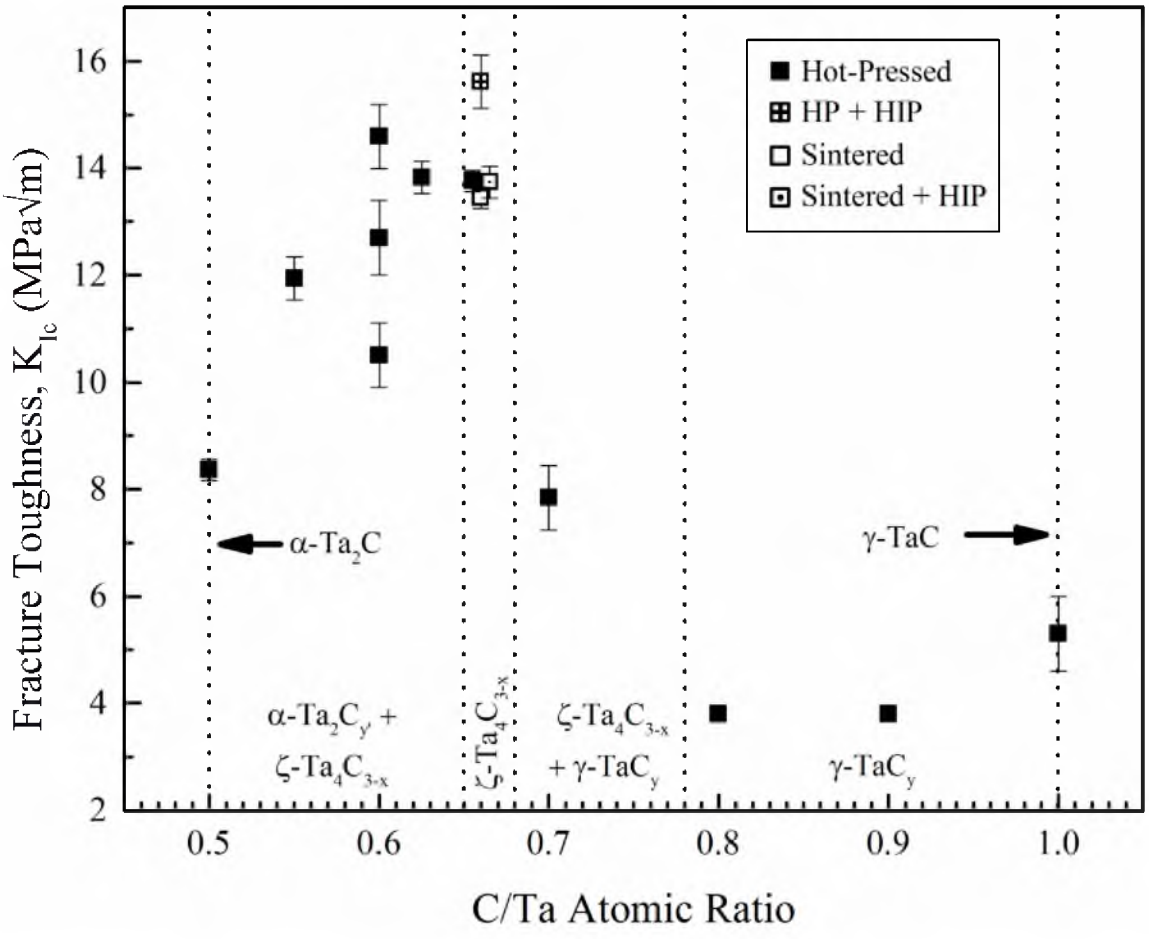

Figure 5.4 Fracture toughness of carbides as a function of C/Ta atomic ratio.

(759 ± 24 MPa). The sintered and the sintered and HIPed material of the same composition had fracture toughness comparable to the hot-pressed material with slightly lower fracture strengths. For compositions, C/Ta > 0.66, there was a large drop in fracture toughness to the lowest value measured in this study, 3.8 ± 0.1 MPa√m for the single-phase material, γ-$TaC_{0.8}$, before recovering to a slightly higher value (5.3 ± 0.7 MPa√m) for the stoichiometric γ-TaC.

Figure 5.5 shows a plot of the fracture toughness as a function of the hardness for all the single-phase and two-phase tantalum carbides processed in this study and in the study of Hackett *et al.* [3, 4]. A general trend of decreasing fracture toughness with increasing hardness is evident in the plot. Similar trends have been seen in other structural ceramic families, for example, SiC [82]. In the tantalum carbide family, high fracture toughness (K_{Ic} > 12 MPa√m) is associated with materials containing predominantly the ζ-Ta_4C_{3-x} phase, while materials with γ-TaC_y as the predominant phase have high hardness. In addition to the phases, the grain size of the dominant phase also plays a role in the hardness-toughness correlation. In Figure 5.5, high fracture-toughness is also associated with large grain size, while the hard materials have small grain size.

5.4 Rising Crack-Growth-Resistance (R-Curve) Behaviors

Figure 5.6 plots crack-growth resistance, K_R, as a function of crack length (R-curves) for the hot-pressed materials ranging in composition from C/Ta = 0.5 to C/Ta = 0.7. There were three trends in the parameters of the R-curves with composition and weight percent of the ζ-Ta_4C_{3-x} phase. The compositions corresponding to high weight fractions of the ζ-Ta_4C_{3-x} phase had shorter initial crack lengths (a_0), higher crack-

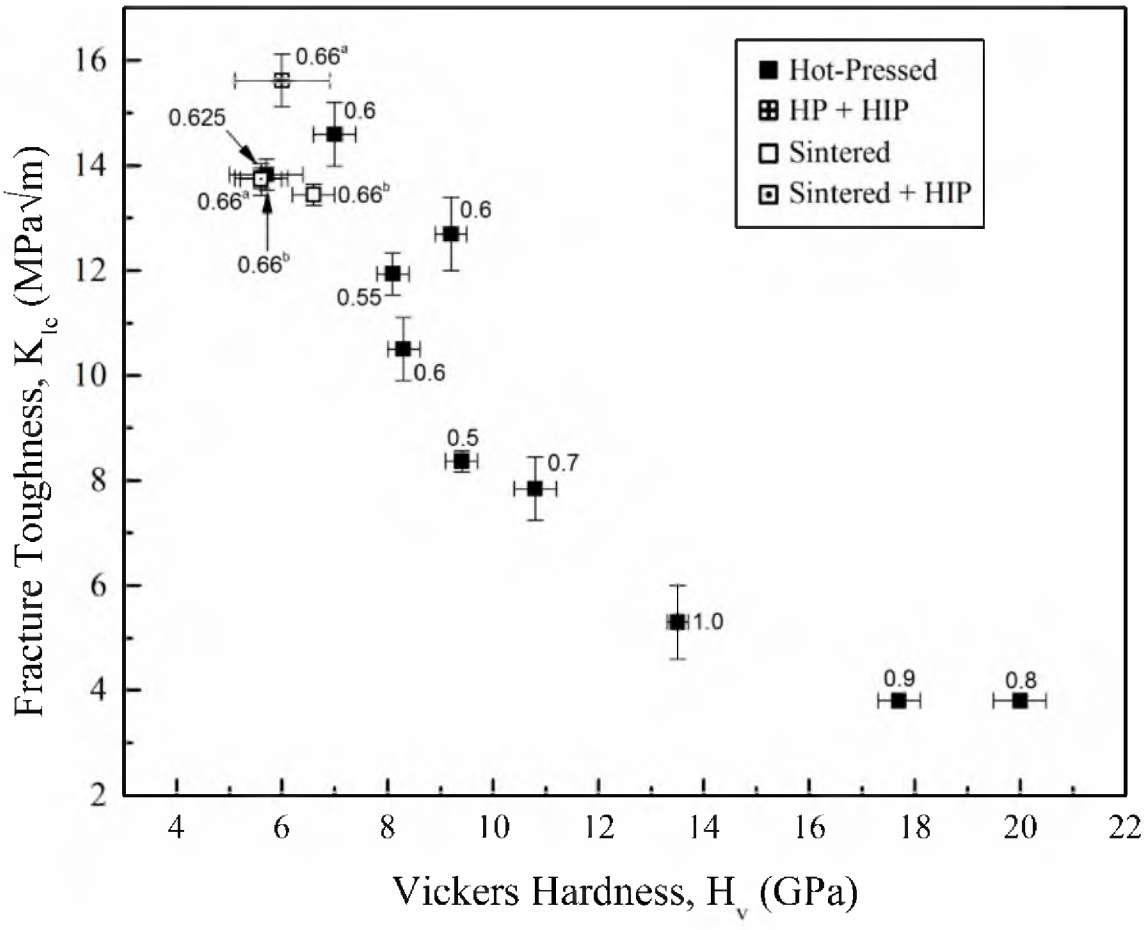

Figure 5.5 Fracture toughness of carbides as a function of hardness (9.8 N load).

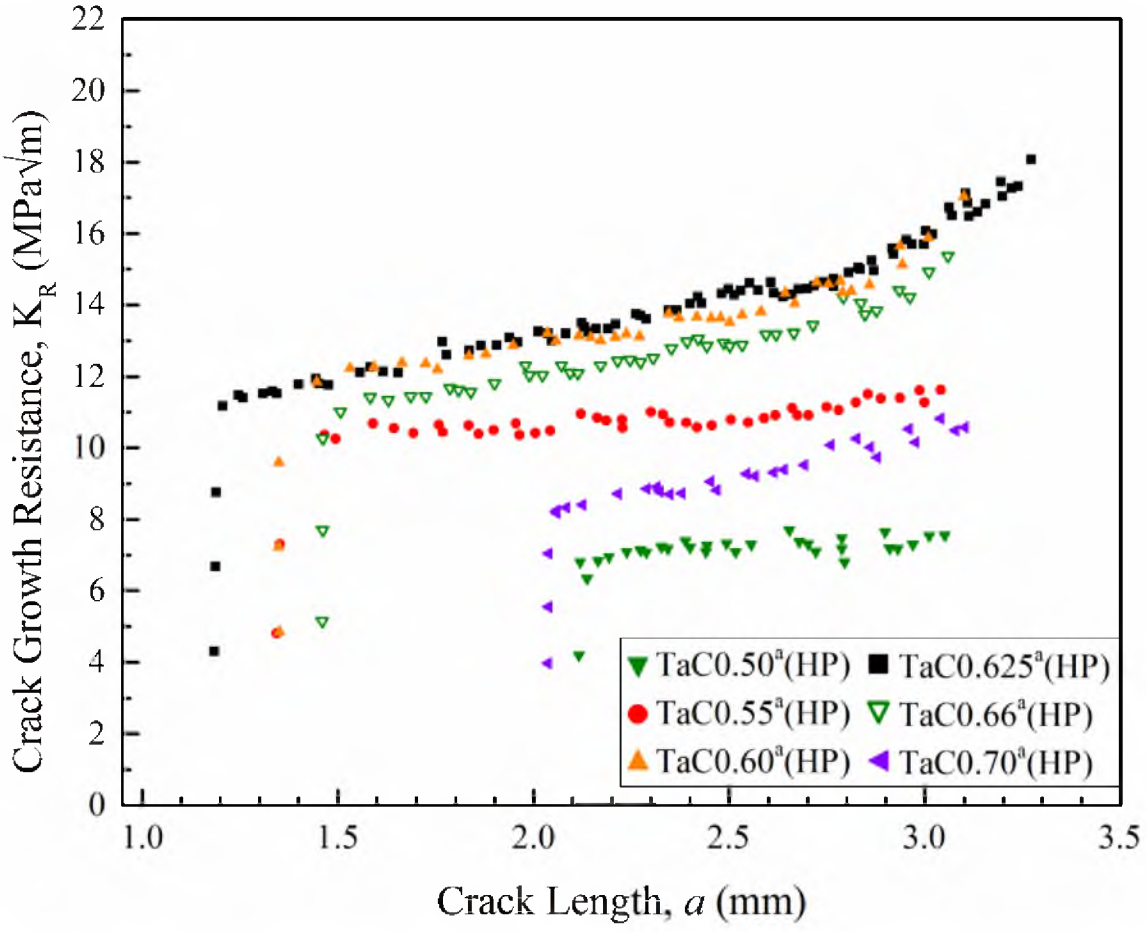

Figure 5.6 Rising R-Curve plots of hot-pressed carbides as a function of crack length, *a*.

extension resistance at a_0, and greater slope of the R-curve. Conversely, the only material which did not contain the ζ-Ta_4C_{3-x} phase in Figure 5.6, $TaC0.50^a$(HP), showed the longest initial crack length, lowest crack-extension resistance at a_0, and lowest slope of the R-curve. A comparison of the SEPB fracture toughness of Figure 5.4 and the R-curves of Figure 5.6 for the same material revealed that the SEPB fracture toughness was slightly higher than the value of K_R at the same initial crack length, a_0. There are two likely reasons for this discrepancy. First, the initial crack length in the SEPB test specimens was measured on the fracture surface as the average of three measurements on the crack front. The crack length in the R-curve test specimens was measured as the average of two crack lengths on the side surfaces. The crack lengths on the free surfaces tend to be slightly shorter than in the middle of the thickness of the specimens. Secondly, the R-curve specimens had notches instead of Vickers indents to reduce the lengths of the initial cracks. The notched length of the initial crack did not have crack-bridging ligaments and, consequently, R-curve specimens did not produce as much crack shielding as the SEPB specimens. A final point of interest to note in the R-curves of Figure 5.6 is that none of the tests ended in unstable fracture. The tests were terminated while the R-curves were still rising and the final crack length was in the range, 3.1 to 3.6 mm (a/W = 0.775 to 0.9). This suggests that the crack-bridging zone did not reach a steady-state even at these crack lengths and the measured fracture toughness values could well be higher if one uses a scaled-up SEPB specimen or a fracture-mechanics specimen of different geometry.

Figure 5.7 plots R-curves for materials of the same composition, $TaC0.66^a$, consolidated by four different methods: hot-pressed (HP), hot-pressed and HIPed

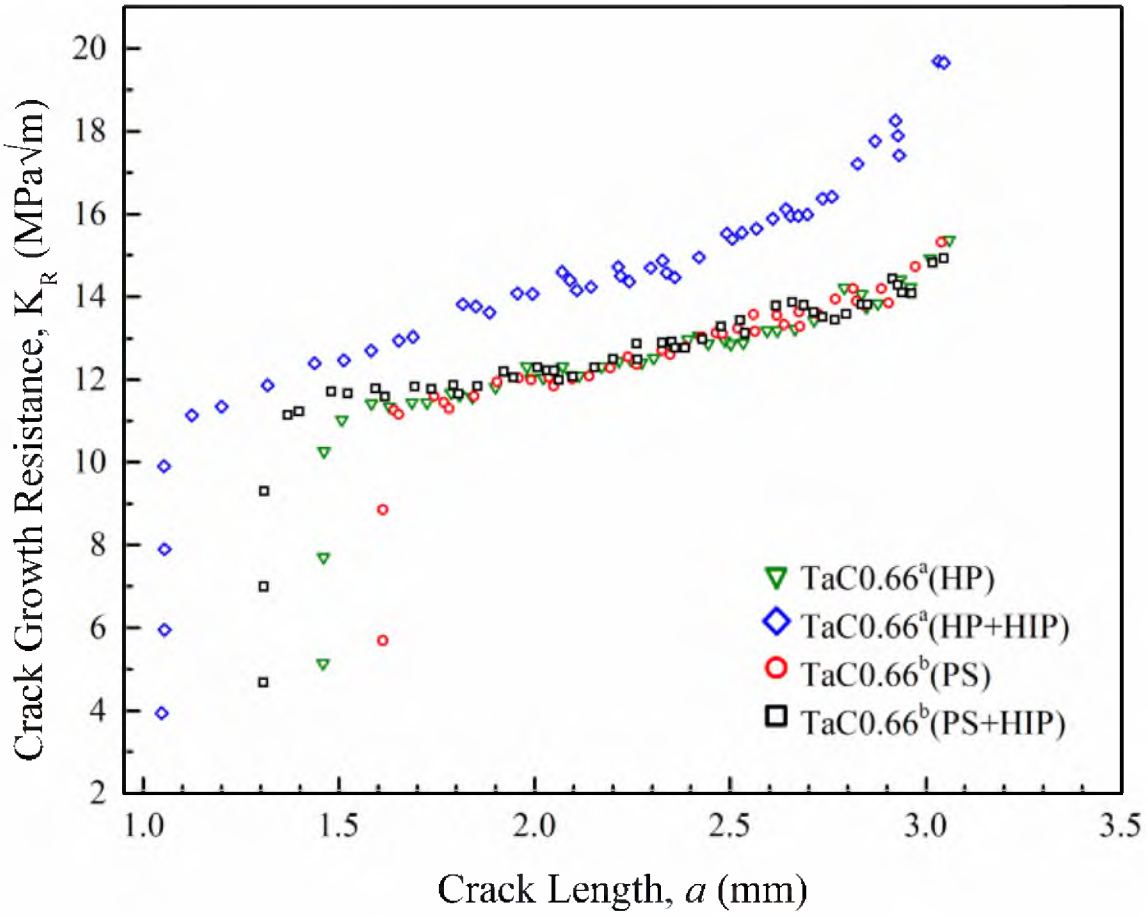

Figure 5.7 Rising R-curve plots of carbides at a C/Ta atomic ratio of 0.66 as a function of crack length, *a*.

(HP+HIP), pressureless sintered (PS), and pressureless sintered and HIPed (PS+HIP). The hot-pressed and HIPed material exhibited the highest R-curve ranging in fracture toughness from 11 MPa$\sqrt{m}$ at an initial crack length of about 1.05 mm to a value of 19.7 MPa$\sqrt{m}$ for a crack length of 3.05 mm. The R-curves for the other three materials, HP, PS and PS+HIP, were essentially identical and ranged from 11 to 15.4 MPa$\sqrt{m}$. It is interesting to note that the SEPB fracture toughness in Figure 5.4 also showed the same trend. The hot-pressed and HIPed material has higher fracture toughness relative to the materials consolidated by the other methods. It is useful to note here again that the hot-pressed and HIPed material had both the highest content of the ζ-Ta_4C_{3-x} phase as well as the largest grain size of this phase.

5.5 Discussion

A variety of mechanisms are known to contribute to high fracture toughness and rising-crack-growth-resistance (R-curve) behaviors of toughened ceramics [83]. These include (a) microcracking ahead of the crack tip, (b) crack deflection or branching, (c) stress-induced phase transformation, and (d) crack-face bridging by various forms of ligaments [83]. Optical and SEM examinations of the crack-tip and the crack-wake regions of the SEPB specimens suggest that the high fracture toughness and the R-curve behavior of ζ-Ta_4C_{3-x} are likely due to crack-face bridging. Typically, the bridging ligaments in single-phase polycrystalline ceramics are large grains or elongated grains, exemplified by coarse-grained alumina [84] and self-reinforced silicon nitride [85], respectively. Second-phase particles and whiskers also act as ligaments in two-phase cermets and whisker-reinforced ceramics [86], respectively. In polycrystalline ζ-Ta_4C_{3-x},

and likely in such compounds as Ti_3XC_2 (X = Si, Al) [19, 20, 22], a new type of bridging ligament applies closure traction on the crack faces in addition to whole grains. Here, they are referred to as lamellae. Examples of crack bridging lamellae are shown in Figures. 5.8(a), 5.8(b) and 5.8(c). Figures 5.8(a) and 5.8(b) show SEM images of crack-bridging lamellae in SEPB specimens, while Figure 5.8(c) shows lamellae bridging in the vicinity of a Vickers indent. Lamellae are essentially plates or sheets consisting of the basal planes of the ζ-Ta_4C_{3-x} crystal. The SEM images, Fig. 5.8(c) in particular, suggest that certain basal planes in the ζ-Ta_4C_{3-x} crystal are weak cleavage planes and lead to the formation of the lamellae. The thickness of the individual lamella varied from 40-300 nm (Figure 5.8(c)) up to 1-2 μm (Figure 5.8(b)). These thicknesses of the lamellae are smaller than the shorter dimension of the grains in the c direction, 5-20 μm. Thus, lamellae bridging of cracks occurs at a scale smaller than the grain size. The easy cleavage and formation of crack-bridging lamellae in polycrystalline ζ-Ta_4C_{3-x} is somewhat analogous to toughening in ceramic laminates with weak interfaces [87]. While the weak interfaces in ceramic laminates are man-made, the weak interfaces in polycrystalline ζ-Ta_4C_{3-x} are intrinsic to the crystal, i.e., they are nature-made. The weak interfaces in polycrystalline ζ-Ta_4C_{3-x} are the basal planes and their in-plane dimension is limited to the grain size. The orientation of the basal planes of the ζ-Ta_4C_{3-x} grain relative to the direction of crack growth is expected to play an important role in lamellae bridging. Grains with basal planes oriented normal to the direction of crack growth will provide the most effective lamellae bridging, while those grains with basal planes parallel to the crack faces are likely to be least effective. This suggests that polycrystalline ζ-Ta_4C_{3-x} with texture is likely to show anisotropy in fracture toughness.

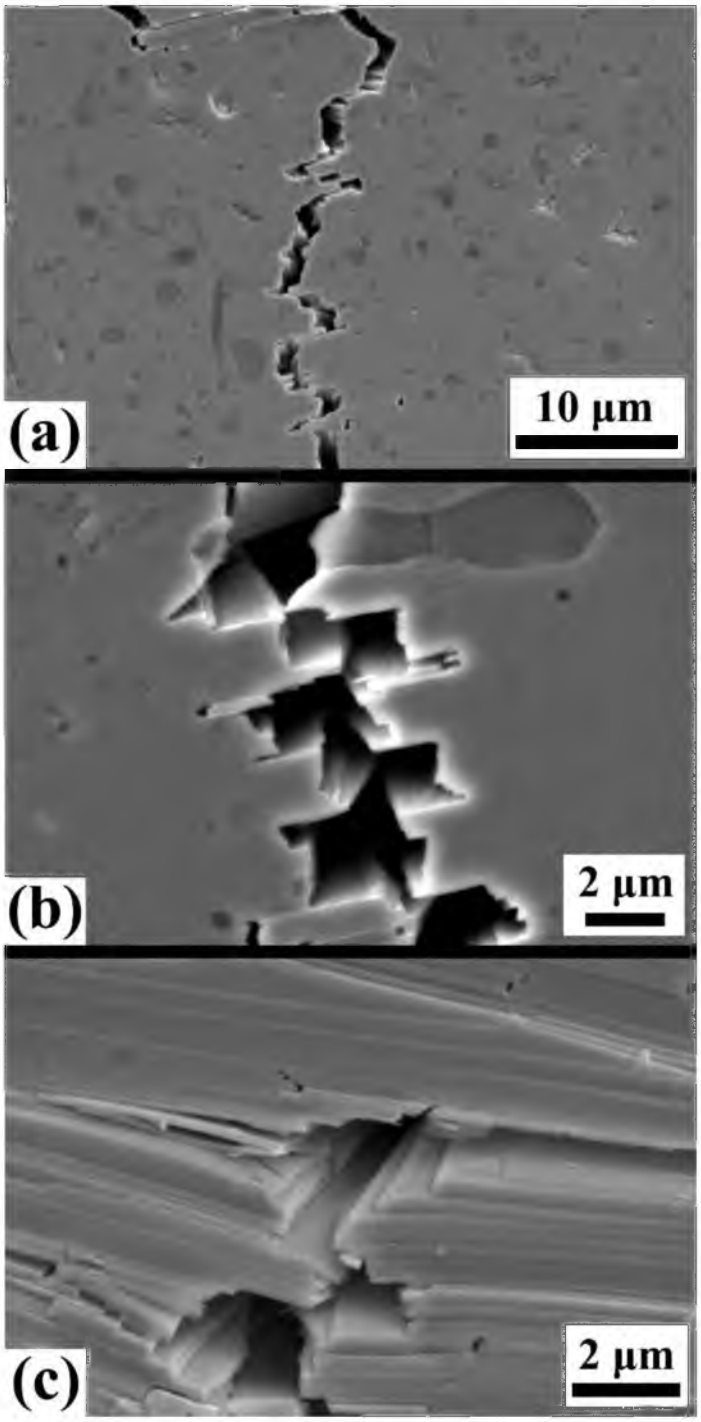

Figure 5.8 SEM images (a & b) showing crack-bridging lamella in SEPB specimens, and (c) showing lamellae bridging in the vicinity of a Vickers indent.

Measurement and characterization of the R-curve behavior of a toughened ceramic can be useful in a number of ways. First, the R-curves measured with the same specimen/crack geometry can be used to compare different ceramics. This is useful in the development and selection of toughened ceramics for structural applications. From this point of view, the R-curve measured for polycrystalline ζ-Ta_4C_{3-x} with SEPB specimens, with fracture toughness ranging from 11 to 19.7 MPa√m (Fig. 5.7), is one of the highest ranges ever reported for a monolithic ceramic. A second objective in characterizing R-curves is to be able to predict the fracture strength and strength variability for cracks initiating at natural flaws in the ceramic. It is now well-established that fracture strength of a ceramic exhibiting R-curve behavior corresponds to a critical applied stress that simultaneously satisfies the following conditions [83]:

$$K_a = K_R$$
$$\frac{dK_a}{dc} = \frac{dK_R}{dc} \tag{5.1}$$

In Eq. (5.1), K_a is the applied stress intensity for a surface or internal crack initiating at a flaw, c is the surface radius of a half-penny or semi-elliptical surface crack or the radius of an internal penny-shaped crack. The applicability of Eq. (5.1) to predict strength and strength variability has been demonstrated for some ceramics, for example, transformation-toughened Ce-TZP/Al_2O_3 [67]. An important caveat here is that the R-curve employed in applying the instability conditions of Eq. (5.1) must be based on measurements of stable growth of cracks from natural flaws. This is due to the fact that

R-curves measured by monitoring stable growth of cracks from surface flaws are often lower in magnitude and steeper in slope than the R-curves measured with large cracks, such as SEPB specimens [83]. It should be recognized, however, that measurements of R-curves for natural surface cracks are not easy or even feasible for all ceramics and this explains the scarcity of such measurements [83].

One encouraging development is the possibility of predicting R-curves for small surface cracks from the bridging stress (σ_{br}) – crack-opening displacement (δ) relationship measured in such large-crack specimens as SEPB or compact tension (CT). Fett *et al.* [88] demonstrated this approach for both fine-grained and coarse-grained alumina. The R-curves for the surface crack were calculated from the superposition of a crack-tip stress intensity (K_0) and a crack-shielding stress intensity due to the bridging ligaments:

$$K_R = K_0 + K_{br} = K_0 + \int_0^a h(x,a)\sigma_{br}(x)dx \tag{5.2}$$

In Eq. (5.2), h(x,a) is a weight function for the surface crack/specimen geometry, and $\sigma_{br}(x)$ is the bridging stress at any position, x, on the crack face obtained from the σ_{br} - δ relationship measured with the large-crack specimen. The R-curves calculated for surface cracks in alumina were within 0.3 MPa$\sqrt{m}$ of the experimental results.

The polycrystalline ζ-Ta_4C_{3-x} ceramic reported in this paper is far from optimum with respect to either its composition (C/Ta atomic ratio) or microstructure. The objective of the current ongoing research is to optimize both the composition and the

microstructure to obtain a combination of high fracture toughness (15 MPa$\sqrt{m}$) and strength (1 GPa). Measurements and/or calculation of the surface-crack R-curves and understanding their relationship with fracture strength are keys to achieving this goal.

CHAPTER 6

CONCLUSIONS AND FUTURE WORK

6.1 Conclusions

- H_2-treatment of Ta metal powder prior to ball milling is effective in increasing specific surface area, reducing the particle size and agglomeration, and maintaining a near equiaxed particle shape relative to untreated Ta powder.
- The enhanced comminution of H_2-treated powder is due to the nucleation and growth of an orthorhombic β-TaH_x phase within the bcc Ta grains, leading to misfit strains and cracking along the grain boundaries.
- Measurements of Vickers microhardness and SEM characterization of the hardness impressions on both untreated and H_2-treated sheets confirmed the higher hardness and lower fracture toughness of the TaH_x phase as compared to the untreated Ta.
- Hydrogenation of the Ta powder coupled with a high charge-to-ball weight ratio (1:10) minimizes WC contamination from wear of the ball mill container.
- Reduction of the size and number of Ta agglomerates led to efficient packing in the binary Ta and TaC compacts and promoted sintering and ζ-Ta_4C_{3-x} phase formation.
- The formation of the ζ-Ta_4C_{3-x} phase occurs in four sequential stages: (a) decomposition of β-TaH_x to Ta, (b) diffusion of C from γ-TaC to Ta leading to the

formation of α-$Ta_2C_{y'}$, (c) equilibration of α-Ta_2C and γ-$TaC_{0.78}$ phases, and (d) formation of ζ-$Ta_4C_{2.56}$ from the equilibrated α-Ta_2C and γ-$TaC_{0.78}$ phases.

- The microstructure showed evidence of nucleation and growth of the ζ-$Ta_4C_{2.56}$ phase in both the α-Ta_2C and γ-$TaC_{0.78}$ parent phases with distinct difference in the morphology due to the different number of variants of the habit plane.
- Materials with increasing ζ-phase content showed increased fracture strength and fracture toughness.
- Rising R-curve behavior was seen in all materials containing the ζ-phase.
- Toughening mechanisms primarily consisted of crack-bridging in the form of ligaments called lamellae.
- The $TaC0.66^{b}$(HP+HIP) materials had larger and more anisotropic ζ-phase grains, which could bridge larger fracture spans and resulted in a material with higher fracture toughness and larger rising R-curves.

6.2 Future Work

In order to consolidate Ta metal powder and γ-TaC powder mixtures to a high density at lower temperatures, and simultaneously improve their mechanical properties (increased fracture strength without affecting fracture toughness) by decreasing the grain size of the dense compacts, the starting powder particle size and morphology needs to be further optimized. One of the fundamental observations in this study has been that a finer, more uniform Ta metal powder morphology, properly milled with γ-TaC can promote densification and reduce the temperature and time at which the high fracture toughness ζ-phase forms.

To reduce hydrogenated Ta powder particle size and maintain a uniform morphology, the use of a planetary mill and a WC milling container are suggested. A high energy planetary mill is expected to further decrease the particle size of hydrogenated Ta metal powder beyond what was achieved in this study. The use of a WC crucible instead of ZrO_2 is also recommended to prevent Zr or O contamination. Since WC-CO is already used as milling media, the use of a WC crucible would not introduce unknown contaminants. Additionally, with a proper balance of media and powder to crucible size, as recommended by the planetary mill manufacturer, the wear of the media and the crucible would be limited.

In addition to using a planetary mill it is recommended that hydrogenated Ta metal powder be processed in an inert atmosphere in order to reduce or eliminate exposure to oxygen. By working in a glove box and argon atmosphere any oxide contamination, which has been identified in the microstructure of sintered materials using EBSD as the δ-Ta_2O_{5-x} phase, would be limited. Oxygen has been previously identified as a contaminant in high surface area Ta metal powders [35, 39] and can inhibit densification in TaC compacts [13].

A more rigorous investigation of the phase boundaries and the nucleation and growth properties of the ζ-phase are also warranted. This body of work, and that of Hackett *et al*. [3, 4], has raised doubt as to the location of the boundaries of the ζ-phase as indicated in the phase diagram of Gusev *et al.* [1]. A detailed study of multiple compositions ranging in C/Ta atomic ratio from 0.62 to 0.68 is recommended. The composition most likely to produce phase pure ζ-Ta_4C_{3-x} would then be annealed at various temperatures using a furnace equipped X-ray diffractometer. By analyzing the

rate of formation of the ζ-phase *in situ*, significantly more data would be generated for use in kinetic analysis, and would possibly pinpoint the minimum temperature at which the ζ-phase phase first nucleates. This *in situ* study would benefit from the use of dense compacts containing a homogeneous mixture of α-Ta_2C and γ-$TaC_{0.78}$ instead of Ta metal powder and γ-TaC powder. Only one reaction step would need to be considered and there would be less alignment issues due to sample shrinkage. Such samples could be made by hot-pressing Ta metal powder and γ-TaC powder mixtures at temperatures below those required to nucleate the ζ-phase, approximately 1500°C.

Two intriguing mechanical studies that could be performed to better characterize the high fracture toughness and rising R-Curve of the ζ-phase include the use of a SEM loading system [89] to monitor *in situ* crack growth as a function of applied stress, and the use of a dynamic fatigue test system to measure fatigue-crack growth properties of the ζ-phase and determine if it is susceptible to cyclic-fatigue failure [20]. The SEM system would be able to monitor the rate of crack growth relative to applied stress, which would be of interest when the crack tip interacts with ζ-phase grains with different orientations. Grains with their basal plans oriented parallel to the propagating crack direction should have faster growth rates than ζ-phase grains with their basal planes perpendicular to the propagating direction. A dynamic fatigue test system, on the other hand, would be able to induce frictional wear at grain bridging sites. The apparent plasticity of the ζ-phase and its high fracture toughness could mean that its more prone to cyclic degradation, similar to what is seen in Ti_3SiC_2 [20].

REFERENCES

[1] A. I. Gusev, A. S. Kurlov, and V. N. Lipatnikov, "Atomic and Vacancy Ordering in Carbide ζ-Ta_4C_{3-x} ($0.28<x<0.40$) and Phase Equilibria in the Ta-C System," *J. Solid State Chem.,* vol. 180, pp. 3234-3246, 2007.

[2] E. Wuchina, E. Opila, M. Opeka, W. Fahrenholtz, and I. Talmy, "UHTCs: Ultra-High Temperature Ceramic Materials for Extreme Environment Applications," *Electrochem. Soc. Interface,* vol. 16, pp. 30-36, 2007.

[3] K. Hackett, S. Verhoef, R. A. Cutler, and D. K. Shetty, "Phase Constitution and Mechanical Properties of Carbides in the Ta-C System," *J. Am. Ceram. Soc.,* vol. 92, pp. 2404-2407, 2009.

[4] K. R. Hackett, "Phase Constitution and Mechanical Properties of Carbides in the Ta-C System," Ph.D., Materials Science and Engineering, University of Utah, 2009.

[5] L. Liu, F. Ye, Y. Zhou, and Z. Zhang, "Microstructure and Mechanical Properties of Spark Plasma Sintered $TaC_{0.7}$ Ceramics," *J. Am. Ceram. Soc.,* vol. 93, pp. 2945-2947, 2010.

[6] M. M. Opeka, I. G. Talmy, E. J. Wuchina, J. A. Zaykoski, and S. J. Causey, "Mechanical, Thermal, and Oxidation Properties of Refractory Hafnium and Zirconium Compounds," *J. Eur. Ceram. Soc.,* vol. 19, pp. 2405-2414, 1999.

[7] W. S. Williams, "Physics of Transition Metal Carbides," *Mater. Sci. Eng.,* vol. A105/106, pp. 1-10, 1988.

[8] F. Monteverde and L. Scatteia, "Resistance to Thermal Shock and to Oxidation of Metal Diborides–SiC Ceramics for Aerospace Application," *J. Am. Ceram. Soc.,* vol. 90, pp. 1130-1138, 2007.

[9] M. Desmaison-Brut, N. Alexandre, and J. Desmaison, "Comparison of the Oxidation Behaviour of Two Dense Hot Isostatically Pressed Tantalum Carbide (TaC and Ta_2C) Materials," *J. Eur. Ceram. Soc.,* vol. 17, pp. 1325-1334, 1997.

[10] A. Metcalfe and N. B. Elsner, "Rocket Nozzle Material," United States of America Patent Publication 2006/0144037 A1, 2006.

[11] T. H. Squire and J. Marschall, "Material Property Requirements for Analysis and Design of UHTC Components in Hypersonic Applications," *J. Eur. Ceram. Soc.*, vol. 30, pp. 2239-2251, 2010.

[12] N. D. Leon, B. Wang, C. R. Weinberger, and G. B. Thompson, "Elevated Temperature Deformation Mechanisms in Ta_2C," *Microc. Microanal.*, vol. 17, pp. 1898-1899, 2011.

[13] X. Zhang, G. E. Hilmas, W. G. Fahrenholtz, and D. M. Deason, "Hot Pressing of Tantalum Carbide With and Without Sintering Additives," *J. Am. Ceram. Soc.*, vol. 90, pp. 393-401, 2007.

[14] N. Alexandre, M. Desmaison, F. Valin, and M. Boncoeur, "Solid State Reaction Between Tantalum (Ta) and Tantalum Carbide (TaC) powders during Hiping," *Key Eng. Mater.*, vol. 132-136, pp. 868-871, 1997.

[15] N. Alexandre, M. Desmaison, F. Valin, and M. Boncoeur, "Synthesis of High Toughness Tantalum Carbide Ta_2C by HIP-Reaction Sintering," in *Hot Isostatic Pressing '93, Proceedings of the International Conference on Hot Isostatic Pressing*, Antwerp, Belgium, 1994, pp. 443-450.

[16] L. Liu, H. Liu, F. Ye, Z. Zhang, and Y. Zhou, "Microstructure and Mechanical Properties of the Spark Plasma Sintered Ta_2C Ceramics," *Ceram. Int.*, vol. 38, pp. 4707-4713, 2012.

[17] M. W. Barsoum, T. El-Raghy, C. J. Rawn, W. D. Porter, H. Wang, E. A. Payzant, *et al.*, "Thermal Properties of Ti_3SiC_2," *J. Phys. Chem. Solids,* vol. 60, pp. 429-439, 1999.

[18] T. El-Raghy, M. W. Barsoum, A. Zavaliangos, and S. R. Kalidindi, "Processing and Mechanical Properties of Ti_3SiC_2: II, Effect of Grain Size and Deformation Temperature," *J. Am. Ceram. Soc.*, vol. 82, pp. 2855-2860, 1999.

[19] T. El-Raghy, A. Zavaliangos, M. W. Barsoum, and S. R. Kalidindi, "Damage Mechanisms around Hardness Indentations in Ti_3SiC_2," *J. Am. Ceram. Soc.*, vol. 80, pp. 513-516, 1997.

[20] C. J. Gilbert, D. R. Bloyer, M. W. Barsoum, T. El-Raghy, A. P. Tomsia, and R. O. Ritchie, "Fatigue-Crack Growth and Fracture Properties of Coarse and Fine-Grained Ti_3SiC_2," *Scripta Mater.*, vol. 42, pp. 761-767, 2000.

[21] M. Radovic, M. W. Barsoum, T. El-Raghy, and S. Wiederhorn, "Tensile Creep of Fine Grained (3-5 μm) Ti_3SiC_2 in the 1000–1200°C Temperature Range," *Acta Mater.*, vol. 49, pp. 4103-4112, 2001.

[22] N. V. Tzenov and M. W. Barsoum, "Synthesis and Characterization of Ti_3AlC_2," *J. Am. Ceram. Soc.*, vol. 83, pp. 825-832, 2000.

[23] R. A. Morris, D. Butts, P. A. Shade, and G. B. Thompson, "Influence of Precipitation Sequence on the 3D TaC + Ta_2C/Ta_4C_3 Microstructure Processed by Vacuum Plasma Spraying," *Microc. Microanal.*, vol. 16, pp. 1882-1883, 2010.

[24] R. A. Morris, B. Wang, L. E. Matson, and G. B. Thompson, "Microstructural Formations and Phase Transformation Pathways in Hot Isostatically Pressed Tantalum Carbides," *Acta Mater.*, vol. 60, pp. 139-148, 2012.

[25] R. A. Morris, B. Wang, and G. B. Thompson, "Variations in Tantalum Carbide Microstructures with Changing Carbon Content," *Int. J. Appl. Ceram. Technol.*, vol. 10, pp. 540-551, 2013.

[26] Y. Chen and J. S. Williams, "Formation of Metal Hydrides by Mechanical Alloying," *J. Alloys Compd.*, vol. 217, pp. 181-184, 1995.

[27] D. A. Small, R. A. MacKay, and R. A. Dunlap, "Hydriding Reactions in Ball-Milled Titanium," *J. Alloys Compd.*, pp. 312-315, 1999.

[28] J.-L. Bobet, C. Even, and J.-M. Quenisset, "On the Production of Ultr-Fine Titanium Hydride Powder at Room Temperature," *J. Alloys Compd.*, vol. 348, pp. 247-251, 2003.

[29] H. J. Friedrich and H. Meyer, "Method of Producing Tantalum or Niobium Powder from Compact Bodied," United States of America Patent 3,635,693, 1972.

[30] T. Yano, N. Oishi, A. Komatsu, and K. Koyama, "Tantalum Powder for Sintered Capacitors," United States of America Patent 3,647,415, 1972.

[31] J. A. Fife and M. F. Getz, "Tantalum Powder and Method of Making Same," United States of America Patent 5,261,942, 1993.

[32] J. A. Fife, "Flaked Tantalum Powder," United States of America Patent 5,211,741, 1993.

[33] J. A. Fife, "Flaked Tantalum Powder and Method of Using Same Flaked Tantalum Powder," United States of America Patent 5,580,367, 1996.

[34] V. M. Pathare, H. K. D. P. Rao, J. A. Fife, H. Chang, R. W. Steele, and L. M. Ruch, "Method of Making Tantalum Metal Powder with Controlled Size Distribution and Products Made Therefrom," United States of America Patent 5,954,856, 1999.

[35] W. Shi, X. Chen, Y. Li, X. Xi, and T. Guo, "Process for Preparing Tantalum Powder for Capacitors," United States of America Patent US 2010/0326239, 2010.

[36] E. Rudy and D. P. Harmon, "Ternary Phase Equilibria in Transition Metal-Boron-Carbon-Silicon Systems, Part 1. Related Binary Systems, Volume V. Ta-C System. Partial Investigation in the System Nb-C and V-C," Aerojet-General Corp, Sacramento CA, 1965.

[37] H. Chang, "Method of Producing High Surface Area, Low Metal Impurity," United States of America Patent 5,234,491, 1993.

[38] R. M. Bergman and C. E. Mosheim, "Tantalum Powder Process," United States of America Patent 4,684,399, 1987.

[39] Y. Mizusaki, H. Iijima, and Y. Noguchi, "Tantalum Powder and Methods of Manufacturing Same," United States of America Patent US 7,679,885, 2010.

[40] R. Yamada, N. Watanabe, K. Sato, H. Asano, and M. Hirabayashi, "Localized Modes in Tantalum Hydrides Studied by Neutron Inelastic Scattering," *J. Physical Soc. Japan,* vol. 41, pp. 85-90, 1976.

[41] T. Schober and A. Carl, "A Revision of the Ta-H Phase Diagram," *Scripta Metall.,* vol. 11, pp. 397-400, 1977.

[42] H. Asano, Y. Ishikawa, and M. Hirabayashi, "Single-Crystal X-ray Diffraction Study on the Hydrogen Ordering in Ta_2H," *J. Appl. Cryst.,* vol. 11, pp. 681-683, 1978.

[43] H. Asano, S. Uematsu, and T. Fukiura, "Detection of Superlattice Reflections from Ta_2H by X-Ray Powder Diffraction," *Trans. Jpn. Inst. Met.,* vol. 24, pp. 661-664, 1983.

[44] A. San-Martin and F. D. Manchester, "The H-Ta (Hydrogen-Tantalum) System," *J. Phase Equilibria,* vol. 12, pp. 332-343, 1991.

[45] S. Semboshi, N. Masahashi, and S. Hanada, "Multiple Cracking of Tantalum by Hydrogenation," *Metall. Mater. Trans. A,* vol. 34A, pp. 685-690, 2003.

[46] S. Semboshi, T. J. Konno, N. Masahashi, and S. Hanada, "Microstructural Observation of Ordered β-Ta_2H in Hydrogenated Tantalum," *Metall. Mater. Trans. A,* vol. 38A, pp. 956-963, 2007.

[47] A. San-Martin, and F.D. Manchester, "H-Ta," *ASM Handbook, Volume 3, Alloy Phase Diagrams*, Materials Park, Ohio: ASM International, 1992, pp. 2-238.

[48] B. R. Simonović, S. Mentus, and M. V. Šušic, "Kinetics of Tantalum Hydriding: the Effect of Palladization," *Int. J. Hydrogen Energy,* vol. 25, pp. 1069-1073, 2000.

[49] R. A. Dunlap, D. A. Small, and G. R. Mackay, "Hydriding Reactions Induced by Ball Milling in Group IV and V Transition Metals," *J. Mater. Sci. Lett.,* vol. 18, pp. 881-883, 1999.

[50] C. L. Yeh and E. W. Liu, "Combustion Synthesis of Tantalum Carbides TaC and Ta_2C," *J. Alloys Compd.,* vol. 415, pp. 66-72, 2006.

[51] I. Zaplatynsky, "Observations of the Zeta Phase in the System Ta-C," *J. Am. Ceram. Soc.,* vol. 49, pp. 109-110, 1966.

[52] W. F. Brizes and J. M. Tobin, "Isolation of the Zeta Phase in the System Tantalum-Carbon," *J. Am. Ceram. Soc.,* vol. 50, pp. 115-116, 1967.

[53] K. Yvon and E. Parthé, "On the Crystal Chemistry of the Close Packed Transition Metal Carbides. I. The Crystal Structure of the ζ-V, Nb and Ta Carbides," *Acta. Cryst.,* vol. B26, pp. 149-153, 1970.

[54] W. F. Brizes, "Diffusion of Carbon in the Carbides of Tantalum," *J. Nucl. Mater.,* vol. 26, pp. 227-231, 1968.

[55] A. I. Gusev, A. A. Rempel, and V. N. Lipatnikov, "Incommensurate Ordered Phase in Non-Stoichiometric Tantalum Carbide," *J. Phys.: Condens. Matter,* vol. 8, pp. 8277-8293, 1996.

[56] A. L. Bowman, "The Variation of Lattice Parameter with Carbon Content of Tantalum Carbide," *J. Phys. Chem.,* vol. 65, pp. 1596-1598, 1961.

[57] R. Lesser and G. Brauer, "Carbide Phases of Tantalum," *Z. Metallk,* vol. 49, p. 622, 1958.

[58] V. I. Smirnova and B. F. Ormont, "Homogeneity Ranges and Variation of the Thermodynamic and other Properties of Tantalum Carbide Phases with their Composition and Structure," *Zh. Fiz. Khim.,* vol. 30, p. 1327, 1956.

[59] D. A. Robins, *The Physical Chemistry of Metallic Solutions and Intermetallic Compounds* vol. Paper 7B. London: Her Majesty's Stationery Office, 1959.

[60] C. P. Kempter and M. R. Nadler, "Thermal Decomposition of Niobium and Tantalum Monocarbides," *J. Chem. Phys.,* vol. 32, p. 1477, 1960.

[61] K. Balani, G. Gonzalez, and A. Agarwal, "Synthesis, Microstructural Characterization, and Mechanical Property Evaluation of Vacuum Plasma Sprayed Tantalum Carbide," *J. Am. Ceram. Soc.*, vol. 89, pp. 1419-1425, 2006.

[62] B. Wang, N. D. Leon, C. R. Weinberger, and G. B. Thompson, "A Theoretical Investigation of the Slip System of Ta_2C," *Acta Mater.*, vol. 61, pp. 3914-3922, 2013.

[63] S. M. Wiederhorn, "Brittle Fracture and Toughening Mechanisms in Ceramics," *Ann. Rev. Mater. Sci.*, vol. 14, pp. 373-403, 1984.

[64] K. T. Faber and A. G. Evans, "Crack Deflection Processes - I. Theory," *Acta Metall.*, vol. 31, pp. 565-576, 1983.

[65] Y.-S. Chou and D. J. Green, "Silicon Carbide Platelet/Alumin Composites: III, Toughening Mechanisms," *J. Am. Ceram. Soc.*, vol. 76, pp. 1985-1992, 1993.

[66] P. Šajgalik, J. Dusza, and M. J. Hoffmann, "Relationship Between Microstructure, Toughening Mechanisms, and Fracture Touhness of Reinforced Silicon Nitride Ceramics," *J. Am. Ceram. Soc.*, vol. 78, pp. 2619-2624, 1995.

[67] N. Ramachandran, L.-Y. Chao, and D. K. Shetty, "R-Curve Behavior and Flaw Insensitivity of Ce-TZP/Al_2O_3 Composite," *J. Am. Ceram. Soc.*, vol. 76, pp. 961-969, 1993.

[68] K. Kendall, N. M. Alford, and J. D. Birchall, "Weibull Modulus of Toughened Ceramics," *MRS Proceedings*, vol. 78, pp. 189-197, 1986.

[69] K. Kendall, N. M. Alford, S. R. Tan, and J. D. Birchall, "Influence of Toughness on Weibull Modulus of Ceramic Bending Strength," *J. Mater. Res.*, vol. 1, pp. 120-123, 1986.

[70] D. L. Hartsock and A. F. McLean, "What the Designer with Ceramics Needs," *Am. Ceram. Soc. Bull.*, vol. 63, pp. 266-270, 1984.

[71] ASTM Standard C1161-02, "Standard Test Method for Flexural Strength of Advanced Ceramics at Ambient Temperature." ASTM International, 100 Bar Harbor Dr., PO Box C700, West Conshohocken, PA 19428-2959.

[72] ASTM Standard C1421-10, "Standard Test Method for Determination of Fracture Toughness of Advanced Ceramics at Ambient Temperature." ASTM International, 100 Bar Harbor Dr., PO Box C700, West Conshohocken, PA 19428-2959.

[73] ASTM Standard E-384-10, "Standard Test Method for Knoop and Vickers Hardness of Materials." ASTM International, 100 Bar Harbor Dr., PO Box C700, West Conshohocken, PA 19428-2959.

[74] B. Pedersen, T. Krogdahl, and O. E. Stokkeland, "On the Motion of Hydrogen in the Tantalum-Hydrogen System," *J. Chem. Phys.*, vol. 42, pp. 72-79, 1965.

[75] G. Schaumann, J. Volkl, and G. Alefeld, "The Diffusion Coefficients of Hydrogen and Deuterium in Vanadium, Niobium, and Tantalum by Gorsky-Effect Measurements," *Phys. Status Solidi B,* vol. 42, pp. 401-413, 1970.

[76] C. Hartmann, J. Wollweber, M. Albracht, and I. Rasin, "Preparation and Characterisation of Tantalum Carbide as an Optional Crusible Mateial for Bulk Aluminium Nitride Crystal Growth Via Physical Vapour Transport," *Phys. Stat. Sol. C,* vol. 3, pp. 1608-1612, 2006.

[77] A. N. Kolmogorov, "On the Statistical Theory of the Crystallization of Metals," *Bull. Acad. Sci. USSR, Math. Ser.*, vol. 1, pp. 355-359, 1937.

[78] W. A. Johnson and R. F. Mehl, "Reaction Kinetics in Processes of Nucleation and Growth," *Trans. Am. Inst. Min. (Metall.) Engrs.*, vol. 135, pp. 416-458, 1939.

[79] M. Avrami, "Kinetics of Phase Change. I General theory," *J. Chem. Phys.*, vol. 7, pp. 1103-1112, 1939.

[80] J. W. Christian, *The Theory of Transformations in Metals and Alloys: Part I + II*, 1st ed.: Pergamon, 2002.

[81] H. Wiesenberger, W. Lengauer, and P. Ettmayer, "Reactive Diffusion and Phase Equilibria in the V-C, Nb-C, Ta-C and Ta-N Systems," *Acta Mater.*, vol. 46, pp. 651-666, 1998.

[82] D. Ray, M. Flinders, A. Anderson, and R. A. Cutler, "Hardness/Toughness Relationship for SiC Armor," *Ceram. Eng. Sci. Proc.*, vol. 24, pp. 401-410, 2003.

[83] D. Munz, "What Can We Learn from R-Curve Measurements?," *J. Am. Ceram. Soc.*, vol. 90, pp. 1-15, 2007.

[84] R. W. Steinbrech, R. Knehans, and W. Schaarwachter, "Increase of Crack Resistance During Slow Crack Growth in Al_2O_3 Bend Specimens," *J. Mater. Sci.*, vol. 18, pp. 265-270, 1983.

[85] T. Ohji, K. Hirao, and S. Kanzaki, "Fracture Resistance Behavior of Highly Anisotropic Silicon Nitride," *J. Am. Ceram. Soc.*, vol. 78, pp. 3125-3128, 1995.

[86] P. F. Becher, C.-H. Hsueh, P. Angelini, and T. N. Tiegs, "Toughening Behavior in Whisker-Reinforced Ceramic Matrix Composites," *J. Am. Ceram. Soc.,* vol. 71, pp. 1050-1061, 1988.

[87] W. J. Clegg, K. Kendall, N. M. Alford, T. W. Button, and J. D. Birchall, "A Simple Way to Make Tough Ceramics," *Nature,* vol. 347, 1990.

[88] T. Fett, D. Munz, J. Seidel, M. Stech, and J. Rodel, "Correlation Between Long and Short Crack R-Curves in Alumina Using the Crack Opening Displacement and Fracture Mechanical Weight Function Approach," *J. Am. Ceram. Soc.,* vol. 79, pp. 1189-1196, 1996.

[89] L. Smiltneek, S. R. Shinde, and D. W. Hoeppner, "Single Cylinder *in situ* Scanning Electron Microscope Fatigue System," *Rev. Sci. Instrum.,* vol. 77, p. 015104, 2006.